Seasonal melting and the formation of sedimentary rocks on Mars, with predictions for the Gale Crater mound

Edwin S. Kite [a,*], Itay Halevy [b], Melinda A. Kahre [c], Michael J. Wolff [d], Michael Manga [e,f]

[a] Division of Geological and Planetary Sciences, California Institute of Technology, Pasadena, CA 91125, USA
[b] Department of Environmental Sciences, Weizmann Institute of Science, P.O. Box 26, Rehovot 76100, Israel
[c] NASA Ames Research Center, Mountain View, CA 94035, USA
[d] Space Science Institute, 4750 Walnut Street, Suite 205, Boulder, CO 80301, USA
[e] Department of Earth and Planetary Science, University of California Berkeley, Berkeley, CA 94720, USA
[f] Center for Integrative Planetary Science, University of California Berkeley, Berkeley, CA 94720, USA

ABSTRACT

A model for the formation and distribution of sedimentary rocks on Mars is proposed. In this model (ISEE-Mars), the rate-limiting step is supply of liquid water from seasonal melting of snow or ice. The model is run for a $O(10^2)$ mbar pure CO_2 atmosphere, dusty snow, and solar luminosity reduced by 23%. For these conditions snow melts only near the equator, when obliquity and eccentricity are high, and when perihelion occurs near equinox. These requirements for melting are satisfied by 0.01–20% of the probability distribution of Mars' past spin–orbit parameters. This fraction is small, consistent with the geologic record of meta-stable surface liquid water acting as a "wet-pass filter" of Mars climate history, only recording orbital conditions that permitted surface liquid water. Total melt production is sufficient to account for observed aqueous alteration. The pattern of seasonal snowmelt is integrated over all spin–orbit parameters and compared to the observed distribution of sedimentary rocks. The global distribution of snowmelt has maxima in Valles Marineris, Meridiani Planum and Gale Crater. These correspond to maxima in the sedimentary-rock distribution. Higher pressures and especially higher temperatures lead to melting over a broader range of spin–orbit parameters. The pattern of sedimentary rocks on Mars is most consistent with a model Mars paleoclimate that only rarely produced enough meltwater to precipitate aqueous cements (sulfates, carbonates, phyllosilicates and silica) and indurate sediment. This is consistent with observations suggesting that surface aqueous alteration on Mars was brief and at low water/rock ratio. The results suggest intermittency of snowmelt and long globally-dry intervals, unfavorable for past life on Mars. This model makes testable predictions for the Mars Science Laboratory *Curiosity* rover at Gale Crater's mound (Mount Sharp, Aeolis Mons). Gale Crater's mound is predicted to be a hemispheric maximum for snowmelt on Mars.

© 2012 Elsevier Inc. All rights reserved.

1. Introduction

The early Mars climate problem has bedevilled generations of scientists (Sagan and Mullen, 1972; Kasting, 1991; Haberle, 1998; Wordsworth et al., 2012a): What allowed widespread sedimentary rocks and valley networks on a planet in a distant orbit around a faint young star? What caused that environment to deteriorate? Climate models struggle to maintain annual mean temperatures $\overline{T} \gtrsim 273$ K on early Mars (Haberle, 1998; Wordsworth et al., 2012a). Seasonal melting can occur for annual maximum temperatures $T_{max} \gtrsim 273$ K, which is much easier to achieve. Therefore, seasonal melting of snow and ice is a candidate water source for surface runoff and aqueous mineralization on Mars. Surface temperatures reach ~300 K at low latitudes on today's Mars. However, seasonal melting of surface-covering, flat-lying snowpack does not

occur because of (1) evaporative cooling and (2) cold-trapping of snow and ice near the poles or at depth. Reduced solar luminosity for early Mars makes melting more difficult (Squyres and Kasting, 1994).

Milankovitch cycles exert a strong control on Mars ice temperatures (Toon et al., 1980). Melting is favored when snow is darkened by dust, when evaporative cooling is reduced by increased pressure, and when the solid-state greenhouse effect is strong (Toon et al., 1980; Clow, 1987). Equatorial snowpacks should form at high obliquity (Jakosky and Carr, 1985), so melt could contribute to the observed low-latitude erosion. Orbital change shifts the locations of cold-traps in which subsurface ice is most stable (Schorghofer and Forget, 2012). Melting on steep slopes is a candidate water source for young midlatitude gullies (e.g., Costard et al., 2002; Hecht, 2002). For example, Williams et al. (2009) modeled melting of relatively clean snow overlain by a thin, dark lag deposit. They found melt rates ~1 kg/m²/h on steep slopes, and argue that this is sufficient to form gullies through either fluvial or

* Corresponding author.
 E-mail address: ekite@caltech.edu (E.S. Kite).
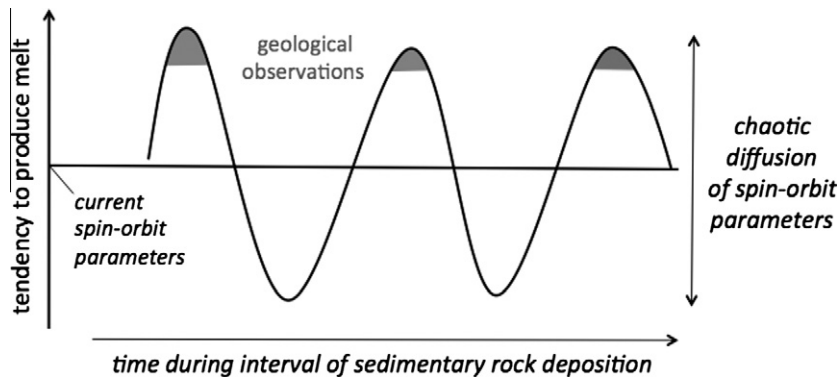
Fig. 1. Motivation for this paper. Mars underwent tens to thousands of spin–orbit oscillations during the interval of sedimentary-rock deposition. Three are shown schematically in this sketch. Mars orbital parameters vary over a wide range, resulting in a correspondingly wide range in tendency to melt. The geologic record of metastable surface liquid water is a wet-pass filter of Mars climate history. Because of the evidence for orbital pacing of sedimentary rock accumulation (Lewis et al., 2008), transient warming events are not shown, but may have been critical for generating geomorphically effective runoff – see Section 8.4.

debris-flow incision. The Laboratoire de Météorologie Dynamique (LMD) General Circulation Model (GCM) has been used to simulate the early martian hydrological cycle, including melting, for selected orbital parameters (Fastook et al., 2012; Wordsworth et al., 2012a).

This paper has two purposes:

- To extend the global snowmelt models with a new model, ISEE-Mars (Ice and Snow Environment Evaluator for Mars). For the first time, ISEE-Mars integrates a model of snowpack temperatures over all spin–orbit parameters, while keeping track of cold-traps. Chaotic diffusion in the Solar System makes it almost certain that Mars' obliquity (ϕ) has ranged 20 times more widely than Earth's obliquity over billion-year periods, and that Mars' eccentricity has had a long-term variance twice that of the Earth (Touma and Wisdom, 1993; Laskar and Robutel, 1993; Laskar et al., 2004; Laskar, 2008). These wide swings cause large variations in insolation and propensity to melt (Fig. 1).
- To understand the water source for sedimentary rock formation on Mars (Malin and Edgett, 2000; Squyres et al., 2004). We focus on the hypothesis that supply of water from seasonal melting was the limiting step in the formation of sedimentary rocks on early Mars. Existing evidence for snowmelt-limited sedimentary rock formation is discussed in Section 2.

If surface liquid water availability was the only limiting factor on sedimentary rock formation, then the spatial distributions of liquid water availability and sedimentary rock detections should correspond to each other. Section 3 analyzes the global sedimentary rock distribution. In the only previous global model of sedimentary rock formation on Mars, Andrews-Hanna et al. (2007) tracked groundwater flow in a global aquifer that is recharged by a broad low-latitude belt of precipitation. Groundwater upwelling is focused in low-lying areas, generally consistent with the observed distribution of sedimentary rocks (Andrews-Hanna et al., 2010; Andrews-Hanna and Lewis, 2011). Their model assumes $\overline{T} > 273$ K, in order to avoid the development of an impermeable cryosphere. Especially in light of the Faint Young Sun predicted by standard solar models, temperatures this high may be unsustainable for the long periods of time required to form the sedimentary rocks (Haberle, 1998; Tian et al., 2010). We assume instead that liquid water is supplied from locally-derived snowmelt, rather than a deep global aquifer (Sections 4 and 5). Groundwater flow contributing to shallow diagenesis is restricted to local aquifers perched above the cryosphere. Annually-averaged and planet-averaged temperatures remain similar to today's, which reduces

the required change in climate forcing from the present state. If Mars' climate once sustained $\overline{T} > 273$ K, then it must have passed through climate conditions amenable to snowmelt en route to the modern desert (McKay and Davis, 1991). The converse is not true.

Sections 3-5 emphasize the model, Sections 6-8 emphasize comparison to geologic data. ISEE-Mars predictions for different paleoclimates are compared to global data in Section 6. Section 7 makes testable predictions for Mount Sharp[1] in Gale Crater (Milliken et al., 2010; Grotzinger et al., 2012), which is the objective of the Mars Science Laboratory (MSL) *Curiosity* rover. The discussion (Section 8) compares three models for sedimentary rock formation: our snowmelt model, the global-groundwater model (Andrews-Hanna et al., 2010), and the ice-weathering model (Niles and Michalski, 2009). We conclude in Section 9. The most important results are shown in Fig. 12 and Fig. 16

The scope of our paper is forward modeling of snowmelt production as a function of (unknown) early Mars climate parameters. We do not attempt to physically model the processes running from snowmelt production to sedimentary rock formation, beyond a qualitative discussion in Sections 7 and 8. A computationally inexpensive 1D model allows us to sweep over a large parameter space. The trade-off is that 1D models cannot track the effect of topographically-forced planetary waves on the atmospheric transport of water vapor, which controls snow precipitation (Colaprete et al., 2005; Vincendon et al., 2010). Any 1D snow location prescription is therefore an idealization.

2. Snowmelt hypothesis

Liquid water is required to explain sedimentary rock texture and bulk geochemistry along the Mars Exploration Rover *Opportunity* traverse across Meridiani Planum, and there is strong evidence for extending this conclusion to other light-toned, sulfate-bearing sedimentary rocks on Mars (Bibring et al., 2007; McLennan and Grotzinger, 2008; Murchie et al., 2009a). The hypothesis in this paper is that the water source for sedimentary rocks on early Mars was seasonal melting, and that liquid water was infrequently available so that melt availability was the limiting factor in forming sedimentary rocks. "Sedimentary rocks" is used to mean units comprised of chemical precipitates or siliciclastic material cemented by chemical precipitates, usually sulfates. These are recognized from orbit as light-toned layered sedimentary deposits (Malin et al., 2010) that

---

[1] Mount Sharp is the informal name of Gale's mound that is used by NASA and the MSL Project. The formal name is Aeolis Mons. We use Mount Sharp in this paper.

characteristically show diagnostic sulfate features in the near-infrared. This definition excludes layered deposits dominated by phyllosilicates, which usually predate sulfates (Bibring et al., 2006; Ehlmann et al., 2011; Grotzinger and Milliken, 2012).

2.1. What is the evidence that sediment lithification on Mars requires liquid water?

Erosion to form cliffs and boulders (Malin and Edgett, 2000; Edgett, 2010), ejection of meter-size boulders from small, fresh craters (Golombek et al., 2010), microscopic texture (Okubo, 2007), and resistance to crushing by rover wheels show that most light-toned sedimentary deposits are indurated or lithified. Lithification involves compaction and cementation. Water is required to form aqueous cements, as well as for fluvial sediment transport. At *Opportunity*'s landing site, evaporitic sandstones (60% chemical precipitates by weight on an anhydrous basis) record groundwater recharge and aqueous cementation, surface runoff, and shallow lithification (McLennan and Grotzinger, 2008). Aqueous minerals are present in sedimentary rocks throughout Meridiani and the Valles Marineris. Murchie et al. (2009a) argue for water-limited lithification of the Valles Marineris sedimentary rocks. Some layered sedimentary deposits on Mars might not require liquid water for long-term stabilization, but these deposits are usually younger or at higher latitudes than the sulfate-bearing layered sedimentary rocks (Hynek et al., 2003; Bridges et al., 2010; Fenton and Hayward, 2010).

2.2. When did sulfate-bearing sedimentary rocks form?

Sulfate-bearing sedimentary rocks occur relatively late in the stratigraphic sequence of evidence for stable surface liquid water on Mars (Murchie et al., 2009b; Fassett and Head, 2011; Massé et al., 2012; Mangold et al., 2010). The most commonly published age for sedimentary rocks on Mars is Hesperian (Carr and Head, 2010), well after the peak of phyllosilicate formation on Mars (Ehlmann et al., 2011; Fassett and Head, 2011). Sedimentary rocks appear to postdate almost all of the large-scale, regionally integrated highland valley networks (Carr and Head, 2010; Fassett and Head, 2011); the observed sedimentary rocks cannot be simply the terminal deposits of the classic valley networks. Therefore, the climate that created the classic valley networks could have been different from the climate that formed the sedimentary rocks (Andrews-Hanna and Lewis, 2011). However, sediments at Meridiani have themselves been reworked by wind, so the peak of sedimentary-rock production may predate the average age of extant outcrop. Sedimentary rocks do contain some channels, often preserved in inverted relief (Edgett, 2005; Burr et al., 2009). Many sedimentary rocks postdate the large impacts of the Late Heavy Bombardment, and some have quasi-periodic bedding suggesting orbitally-paced deposition (Lewis et al., 2008, 2010). These observations are inconsistent with brief bursts of rapid sedimentary rock formation during impact-induced greenhouse events.

2.3. What existing data supports the snowmelt hypothesis?

Liquid water was in short supply even at the time of sedimentary rock formation at the *Opportunity* landing site. Mineralogy indicates that weathering at Meridiani was either isochemical or at low water/rock ratio or both (Berger et al., 2009; Hurowitz and McLennan, 2007; Ming et al., 2008), consistent with a rare trickle of snowmelt. Low specific grind energy of sandstones indicates weak aqueous cementation (Herkenhoff et al., 2008). All but two of the rock and soil classes at the *Spirit* and *Opportunity* landing

sites contain olivine[2] (Morris et al., 2006a,b, 2008), including rocks at both sites that contain aqueous minerals at the 5–60 wt.% level (e.g., Squyres et al., 2006). Orbital thermal spectra show olivine on terrain of all ages, so martian wet epochs were either brief, local, or both (Koeppen and Hamilton, 2008). The present day extent of sedimentary rock outcrops on Mars is small, and the persistence of opal, jarosite and olivine indicates minimal water–rock interaction since those minerals crystallized (Tosca and Knoll, 2009; Olsen and Rimstidt, 2007; Elwood Madden et al., 2009). Olivine's pervasive persistence requires that *for any given parcel of sediment* the duration of water–rock interaction was a very small fraction of Mars surface history.

Sedimentary rocks outcropping at the Mars surface were once buried. If conditions at depth were cold or dry as in the snowmelt hypothesis, olivine persistence is easy to understand: even supposing surface melting occurred every year for hundreds of millions of years, each parcel of sediment would spend a relatively short time at shallow, seasonally wet depths before being buried and frozen. If groundwater pervaded the rocks after burial, then olivine persistence is less easy to understand.

Away from the sedimentary rocks themselves, aqueous mineralization was minor or absent elsewhere on the surface at the time when most sulfate-bearing sedimentary rocks formed (Murchie et al., 2009b; Salvatore et al., 2010; Ehlmann et al., 2011; Hausrath et al., 2008). No measurable regional-scale K/Th fractionation occurred, so "aqueous events must have been brief or the total throughput of water small" (Taylor et al., 2010). Globally, data are most consistent with soil formation "with little aqueous alteration under conditions similar to those of the current martian climate" (Bandfield et al., 2011). Elemental profiles indicate top-down mobilization of soluble elements (Amundson et al., 2008; Arvidson et al., 2010).

Geomorphic evidence that the Mars surface environment has only marginally supported surface liquid water since the Noachian includes long-term average erosion rates 1–10 m/Ga at Meridiani and ∼0.03 m/Ga at *Spirit*'s landing site, Gusev Crater (Golombek et al., 2006), together with a sharp post-Noachian decline in valley network formation and crater infilling (Fassett and Head, 2008; Forsberg-Taylor et al., 2004). Dividing the total thickness of sedimentary rock deposits by the thickness of quasi-periodic layers and then multiplying by the obliquity periods thought to pace accumulation suggests that observed sedimentary rocks formed in 1–10 Ma (Lewis et al., 2010), consistent with the frequency of embedded craters (Kite et al., 2012). This is a small fraction of Mars' history.

These data argue for a short-lived and downward-infiltrating post-Noachian water supply, suggestive of transient liquid water that is generated only during brief melt events.

2.4. How could brief pulses of snowmelt form kilometer-thick accumulations of sedimentary rock?

Seasonal meltwater can indurate loose material via wicking of water through soils to make the equivalent of caliche/gypcrete, or local ponding of water to form transient pools where layers of evaporite minerals accumulate. Peace-class rocks at Gusev preserve evidence for movement of water through soils to make the equivalent of caliche on early Mars. They consist of olivine-rich, relatively weakly altered ultramafic sand grains cemented by 16–17 wt.% sulfate salts; "the cement may be essentially a sulfate caliche" (Squyres et al., 2006). Peace-class rock specific grind energy is about 2 J/mm^3, in family with Burns Formation rocks at the *Opportunity* landing site (Arvidson et al., 2004). *Opportunity* has not

---

[2] Setting aside out-of-place rocks such as meteorites, the exceptions are the Independence class at the heart of Husband Hill and the Montalva class at Low Ridge.

found the source of the sulfate-rich sand grains that went into the Burns Formation, but data are consistent with ponding of water to form pools where layers of evaporite minerals accumulated (McLennan et al., 2005).

Antarctica's McMurdo Dry Valleys are a terrestrial analog for seasonal-melt-limited fluvial erosion and sedimentary rock formation at $\overline{T} < 273$ K (Lee and McKay, 2003; Marchant and Head, 2007; Doran et al., 2010). Weathering and mineralization is confined to lakes, hyporheic zones, and a shallow active layer. However, seasonal river discharges reach 20 m^3 s^{-1} (McKnight, 2011), fluvial valleys incise >3 m deep into granite (Shaw and Healy, 1980), and annually-averaged weathering intensity within the hyporheic zone is greater than in temperate latitudes (Nezat et al., 2001). Sublimation concentrates ions within ice-covered lakes. Outcrops of gypsum, carbonate evaporites, and algal limestone sediments show that sediments have accumulated at the base of melt-fed perennial lakes for 300,000 years (Doran et al., 1998; Hendy, 2000). Dry Valley Drilling Project cores show lithification in older horizons (McKelvey, 1981).

Order-of-magnitude energy balance and mass balance calculations show that brief, rare pulses of snowmelt provide enough water to form the kilometers of sedimentary rock observed on Mars. For solar luminosity reduced by 23%, peak noontime insolation at Mars at perihelion on a moderate-eccentricity ($e = 0.15$) orbit is ≈ 630 W/m^2. If the snowpack is dusty then its albedo will be that of Mars dust, 0.28 (Putzig et al., 2005). During melting, radiative losses are $\sigma T_{melt}^4 \approx 320$ W/m^2, and for a 200 mbar atmosphere a reasonable value for wind-speed dependent sublimation losses into dry air is $\sim$60 W/m^2. Conductive losses will be roughly one-half the diurnal temperature range divided by the diurnal skin depth, giving 60 W/m^2 for a 100 K diurnal cycle of surface temperature and the snowpack thermal properties in Carr and Head (2003). Greenhouse forcing from a 200 mbar CO$_2$ atmosphere equilibrated with a 230 K daily mean surface temperature is $\sim$60 W/m^2 (from detailed radiative transfer calculations: Appendix B). Neglecting all other gains and losses, the net energy available for melting is therefore $630(1 - 0.28) - 320 - 60 - 60 + 60 \approx 100$ W/m^2, equivalent to approximately 1 kg/m^2/h snowmelt.

The total water required to form the 800 m-thick Meridiani sediments depends on the water/rock mass ratio (W/R) during alteration. W/R is given as $\lesssim 1$ by Berger et al. (2009) and $\lesssim 300$ by Hurowitz and McLennan (2007). This corresponds to a time-integrated melt column of either $\lesssim$0.3 km or $\lesssim$100 km, respectively, for a bulk Meridiani sandstone density of 2.3, and ignoring the contribution of water bound in hydrated minerals to the solid mass of the deposit. If melt was produced continuously at 1 mm/h, these time-integrated melt columns would be reached in 30 years (for W/R = 1) or 10 Kyr (for W/R = 300), but these surface liquid water production rates are completely unrealistic (except just after a large impact; Toon et al., 2010). However, if we make the realistic assumptions that melting occurs for 10% of each sol, the melt season lasts for 10% of the year, and 90% of melt refreezes and is unavailable for alteration, then the upper limit on W/R for the entire Meridiani sandstone is still reached after seasonal melt production for a small number of years (30 Kyr for W/R = 1, or 10 Myr for W/R = 300). Net loss of snow to melting is $O(1$ cm)/year in this case. Exhaustion of snowpack is unlikely to severely limit the melt produced: for example, GCM runs show 1–2 cm/year net accumulation (accumulation−sublimation) in sedimentary-rock locations (Madeleine et al., 2009). Sedimentary rocks formed on Mars for an interval of $O(10^9)$ years, so climate and orbital conditions favorable for surface liquid water at Meridiani are only needed for <1% of that time.

This fraction is small, consistent with the geologic record of metastable surface liquid water acting as a "wet-pass filter" of Mars climate history, only recording orbital conditions that permitted surface liquid water (Fig. 1). Evidence that the sedimentary

rocks formed in a small fraction of Mars' history (Lewis et al., 2010) is consistent with negligible liquid water availability for mean orbital forcing. If the martian sedimentary rock record only records orbital conditions that permitted surface liquid water, then modeling average orbital conditions is neither sufficient nor appropriate. To capture the orbital conditions that would be preserved by a wet-pass filter, it is instead necessary to calculate snowmelt for the full range of orbital elements that Mars likely sampled over the time interval of sedimentary rock deposition (Fig. 1). These predictions can then be compared to observations.

3. Distribution of sedimentary rocks on Mars

The Mars Orbiter Camera Narrow Angle (MOC NA) team documented $\sim$4000 "layered rock outcrops of probable or likely sedimentary origin" (Malin et al., 2010), which is the only available global catalogue of sedimentary rocks on Mars (as of December 2012). Details of our analysis of these data are given in Appendix A. The resulting distribution of sedimentary rocks on Mars (Fig. 2) suggests that surface water availability was narrowly concentrated near the equator and at low elevations (Lewis, 2009). 64% of sedimentary rocks are within 10° of the equator, 60% when the Valles Marineris region (260–330°E, 20°S–20°N) is excluded (Fig. 2a). Blanketing by young mantling deposits may contribute to the paucity of sedimentary rocks poleward of 35° in both hemispheres, but cannot explain the rarity of sedimentary rocks at 10–35° latitude relative to the equatorial belt. The ±10° band is not unusual in thermal inertia (TI), dust cover index, albedo, or surface age distribution, so a dependence of sedimentary rock on these parameters could not explain the latitudinal distribution.

On average, sedimentary rocks are lower than ancient terrain by 2 km (Fig. 2b). On Earth sedimentary rocks are low-lying because of sediment transport by regional-integrated channel networks, but evidence for regionally-integrated channel networks on Mars mostly predates the sedimentary rock era (Carr and Head, 2010; Fassett and Head, 2011). The low-elevation bias is independent of the equatorial concentration. Therefore, the low-elevation bias reflects a planetwide, non-fluvial process that occurs preferentially at low elevations.

Although sedimentary rock abundance away from the equator is much less than in the equatorial sedimentary-rock belt, "wings" of increased sedimentary rock abundance are found nearly symmetric about the equator at 25–30°S and 20–30°N. The sedimentary rocks in the southern wing are regionally associated with clusters of large alluvial fans (Fig. 2c).

4. ISEE-Mars model

This section describes ISEE-Mars. We give an overview of the model framework and assumptions in Section 4.1; describe the 1D snowpack thermal model in Section 4.2; describe the potential-well approximation for warm-season snow locations in Section 4.3; and explain how we combine results from 1D models to produce predictions in Section 4.4.

4.1. Overview of model framework

Controls on Mars snowmelt include:

- *Spin–orbit properties* $\mathbf{O} = \{\phi, e, L_p, L_s, \text{latitude}\}$ control the distribution of sunlight at a given location. These include obliquity ϕ, eccentricity e, solar longitude of perihelion L_p, solar longitude L_s, and latitude. Milankovitch parameters $\mathbf{O}' = \{\phi, e, L_p\}$ oscillate or circulate on 10^{4-6} yr frequencies, and ϕ shows chaotic shifts
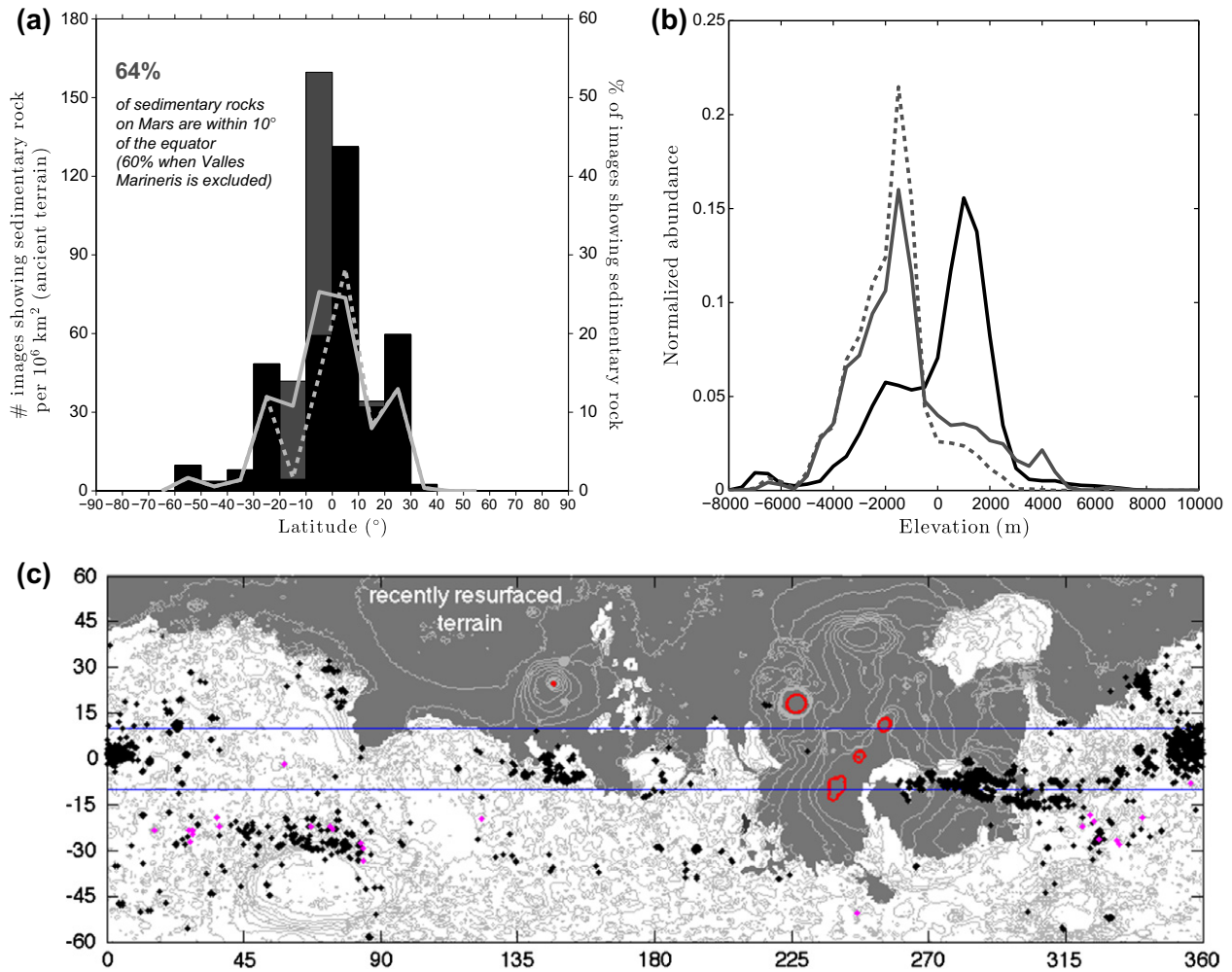
Fig. 2. (a) Latitudinal dependence of martian sedimentary rocks. Latitude bin size is 10°. Histogram corresponds to number of images (left axis). Gray bars are the contribution from the Valles Marineris region, and black bars represent the rest of the planet. Lines correspond to the percentage of images showing sedimentary rock (right axis). Dashed line is the percentage of images showing sedimentary rocks once the Valles Marineris region is excluded. (b) Elevation dependence for: terrain with sedimentary rocks (solid gray line); all ancient terrain (black line); and terrain with sedimentary rocks after masking out Valles Marineris (dotted gray line). Histograms bin size is 500 m. Median sedimentary rock elevation is ∼2 km lower than median ancient terrain. (c) Distribution of sedimentary rocks (black dots, from Malin et al., 2010). Alluvial fans are also shown (purple dots, from Kraal et al., 2008). Blue horizontal lines highlight the ±10° latitude band. Dark gray shading corresponds to recently resurfaced terrain, which is masked out from the analysis. Light gray contours show topography, with the +10 km contour highlighted in red. Appendix A has details of this analysis. (For interpretation of the references to color in this figure legend, the reader is referred to the web version of this article.)

at ∼250 Myr intervals (Head, 2011). We iterate over all the spin–orbit properties that have probably been encountered by Mars over the last 3.5 Ga (Steps 1–2 in Fig. 3).

- *Climate parameters* **C** = {$P, \Delta T, f_{snow}$} include atmospheric pressure P (assumed to be mostly CO_2), freezing-point depression/non-CO_2 greenhouse forcing ΔT, and snow coverage fraction f_{snow}. These are iterated over a large range (Step 3 in Fig. 3). They are assumed to vary slowly relative to changes in spin–orbit properties.
- *Surface material properties, insolation*. These are held fixed for the ensemble of model runs.

Fig. 3 summarizes how we evaluate the predictions of the snowmelt hypothesis. First, for a given trial set of past climate parameters **C** and orbital parameters **O**, we calculate snow temperature for all seasons and latitudes using a 1D surface energy balance model (Steps 1–2 in Fig. 3). This defines a zone in which snow could melt, if it were present. In reality much of this melt zone could lack snow during the warm season (or it could be snow-free year round). We pick snow locations using the assumption that warm-season snow is only found in places that have a low annual-average snow sublimation rate. We refer to this as the "potential-well approximation". Using the 1D model output for a

range of P (Step 3), potential peak temperatures and potential annual-average snow sublimation rates are mapped onto topography (Step 4). Snowmelt occurs when temperatures exceed freezing at locations that are near-minima in annual-average sublimation rate (Step 5) – when the melt zone overlaps the cold traps. The output at this stage consists of maps of snow stability for a single **C** and **O′**, along with time series of snow temperature and melt rates. We analyze this output for a fictitious flat planet in Section 5.3, and for real Mars topography in Section 5.4. Next, ISEE-Mars loops over all possible early Mars **O** (Step 6), convolving the outputs with the **O′** probability distribution function (Laskar et al., 2004). The output is now a map of predicted snowmelt on Mars integrated over geologic time. This map can be compared to observed sedimentary rock abundance and thickness data (Section 5.5). Similar maps are computed for many plausible **C**. Assuming the snowmelt model is correct, the **C** that gives the map in best agreement with data is the best-fit early Mars climate (Section 6.1). Interpolating in the melt rate output gives a predicted time series at Gale (Section 7).

4.2. Thermal model

Surface liquid water is always unstable to evaporation on a desert planet (Richardson and Soto, 2008a; Richardson and Soto,
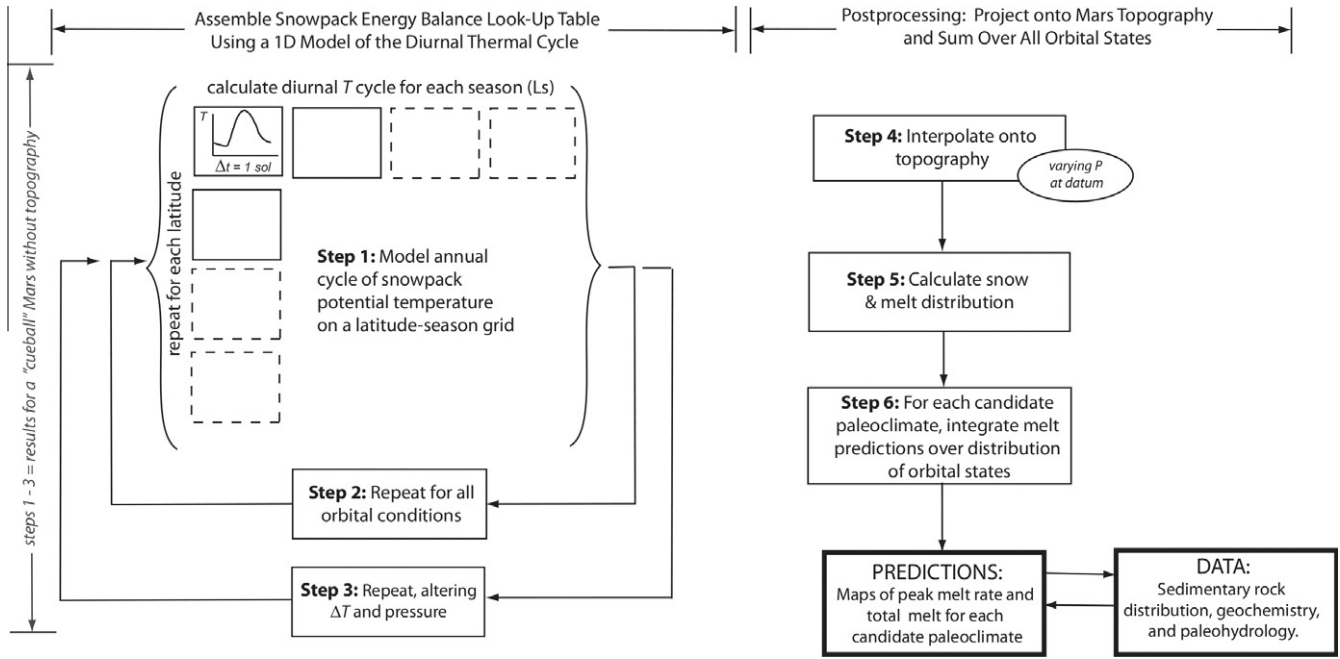
Fig. 3. Workflow of the early Mars seasonal melting model, ISEE-Mars. See text for details.

2008b). However, transient liquid water can occur metastably if temperatures exceed the freezing point, and if P exceeds the triple point (in order to prevent internal boiling).

ISEE-Mars captures these dynamics using a 1D thermal model (Fig. 4). When temperature exceeds (273.15 K – ΔT), melting occurs and buffers the temperature at the melting point. Within the snowpack, we assume material properties are uniform with depth, and heat flow is by conduction and solar absorption only. When melt is not present, energy balance in the subsurface layer adjacent to the surface is given for unit surface area by (Fig. 4)
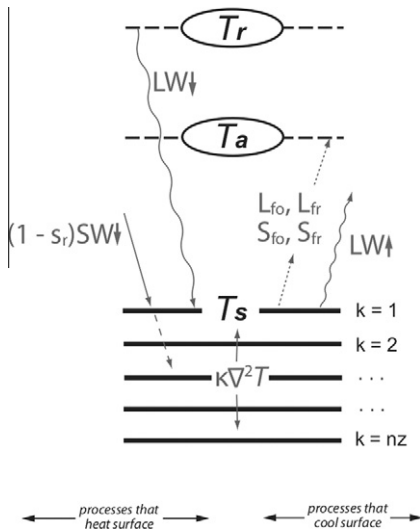

Fig. 4. Vertical discretization and energy flow in the 1D model. Solid horizontal lines correspond to solid surface layers numbered $K = \{1 \cdots n_z\}$, dashed horizontal lines correspond to atmospheric layers. T_r is the effective atmospheric radiative temperature, T_a is the atmospheric surface layer temperature, and T_s is the ground surface temperature. The diagonal arrows correspond to energy fluxes: $LW\downarrow$ for greenhouse effect, $(1 - s_r)SW\downarrow$ for insolation attenuated by Rayleigh scattering, $LW\uparrow$ for back-radiation, and $\{L_{fo}, L_{fr}, S_{fo} \text{ and } S_{fr}\}$ for the turbulent fluxes. Some insolation penetrates into the snowpack (dashed continuation of insolation arrow). $\kappa\nabla^2 T$ corresponds to conductive diffusion.

$$\frac{\partial T_1}{\partial t} = \kappa\nabla^2 T + \frac{1}{\rho C_s \Delta z}\left[\underbrace{LW\downarrow -\epsilon\sigma T^4 + (1 - s_r)Q(1)SW\downarrow}_{radiative\ terms}\right.$$
$$\left. - \underbrace{S_{fr} - L_{fr}}_{free\ convection} - \underbrace{S_{fo} - L_{fo}}_{forced\ convection}\right] \tag{1}$$

and energy balance at depth z within the snowpack is given by (Fig. 4)

$$\frac{\partial T_K}{\partial t} = \kappa\nabla^2 T + \frac{1}{\rho C_s \Delta z}\left[\underbrace{(1 - s_r)Q(z)SW\downarrow}_{solid-state\ greenhouse}\right] \tag{2}$$

Here, ρ is snow density, C_s is snow specific heat capacity, Δz is the thickness of the subsurface layer whose upper boundary is the surface, T is the temperature at subsurface level $K = \{1, 2, \ldots, n_z\}$, k is snow thermal conductivity, ϵ is the longwave emissivity of ice, $LW\downarrow$ is downwelling longwave radiation, s_r is the Rayleigh-scattering correction factor, $Q_{\{1,2,\ldots,n_z\}}$ is the fraction of sunlight absorbed at level z (Appendix C), $SW\downarrow$ is solar flux per unit surface area, S_{fr} corresponds to free sensible heat losses driven by atmosphere-surface temperature differences, L_{fr} corresponds to evaporative cooling by free convection when the atmosphere has relative humidity <1, S_{fo} corresponds to forced sensible heat losses caused by cool breezes over warm ground, and L_{fo} corresponds to additional evaporative cooling by wind. Snow albedo, α, is $1 - \int Q_z dz$. We use the 3.5 Gya solar luminosity calculated by Bahcall et al. (2001), which is 23% below present.

To keep the model straightforward, melt is not permitted to drain, and refreezes in place. In reality, snow and soil are porous. Draining and channelization of melt and associated release of latent heat at better-insulated depths are key in terrestrial snow hydrology (e.g., Bengtsson, 1982; Illangasekare et al., 1990). Examples of meltwater flowing through the ground below the diurnal/annual thermal skin depth include flow down shadowed crevasses that (in the absence of flow) would be below the freezing point day and night; taliks (Sloan and van Everdingen, 1998; Arcone et al.,

2002); supraglacial lake drainage; and high Arctic springs (Andersen et al., 2002; Scheidegger et al., 2012). Although low-latitude melting in ISEE-Mars only occurs within $O(1)$ diurnal skin depth of the surface, these Earth analogs suggest that shallow melting can recharge significantly deeper aquifers. Although large, deep aquifers can result from snowmelt, this is not strictly necessary to explain the sedimentary rocks. Small amounts of melt, which cement unconsolidated material close to the surface, are probably sufficient.

We give details of the flux parameterizations, melt handling, and run conditions in Appendix B. Representative output is shown in Fig. 5.

Low-latitude melting is most likely when both α and TI are low (Fig. 6). We use fixed, low values of TI ($\sim$277 Kieffers, where 1 Kieffer = 1 J m^{-2} K^{-1} s$^{-1/2}$) and α (0.28, the same as that of Mars' dust continents; Mellon et al., 2000). Our simulated snowpack has similar TI to the snow in previous Mars snowmelt models, and it is more reflective (Fig. 6 and Table B.1) (Costard et al., 2002; Carr and Head, 2003; Williams et al., 2009; Morgan et al., 2010). Snow-like (low) TI is justified because water snow precipitation is predicted by all General Climate Models (GCMs) at high ϕ (e.g., Mischna et al., 2003; Fastook et al., 2008; Madeleine et al., 2009; Wordsworth et al., 2012a) and was observed on Mars by *Phoenix* (Whiteway et al., 2011). Pure, fresh, fine-grained snow has a high albedo that prevents melting, but snow albedo is greatly reduced by contamination at the part-per-thousand level with darkening agents, and acquires the albedo of dust following contamination with $O(1\%)$ dust (Warren and Wiscombe, 1980; Warren, 1984; Appendix C). Present day observed and calculated Mars seasonal H$_2$O snow α is 0.25–0.4 (Vincendon et al., 2010; Kereszturi et al., 2011). α on the South Polar water ice cap is 0.30 (Titus et al., 2003). Dust storms and dust devils occur every year, and cause major changes in regional and global albedo (Geissler, 2005; Putzig and Mellon, 2007). Globe-encircling dust storms, which now occur every few years, are likely to occur twice every year at high ϕ (Haberle et al., 2003). Dust is required to supply ice nuclei for heterogenous nucleation. Therefore, it is reasonable to expect snowpack at high ϕ to be contaminated with dust (and, occasionally, fine-grained impact ejecta and volcanic ash). During melting, impurities often tend to accumulate at the surface rather than being removed by runoff (Warren, 1984). Using material properties that favor melting is conservative, because the reconstructed paleoclimate will involve the smallest change from the current Mars climate that is consistent with the geological evidence.
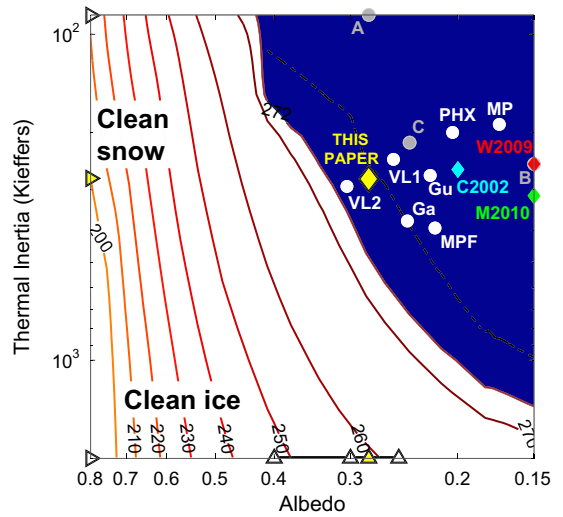
Fig. 6. Sensitivity of peak snowpack temperature to snowpack albedo and thermal inertia for 3.5 Gya insolation, 195 mbar atmosphere, and optimal orbital conditions, during the warm season at the equator. Orange through red contours are for peak temperature within the snowpack, and the dark-shaded area experiences some melting. "Clean snow" and "clean ice" never melt, so contamination with dark materials is required to lower albedo. The black dashed contour shows the onset of significant melting (1 kg/m^2/day). The material properties used in this paper (yellow diamond and yellow triangles) are shown in the context of snowpack properties adopted by a subset of other Mars snowmelt modeling groups (diamonds) and measurements of currently snow-free Mars terrain (circles). Gray circles are the modes of TES thermophysical classes A, B and C (Mellon et al., 2000). White circles are for landing sites (Golombek et al., 2012): VL1 = Viking Lander 1; VL2 = Viking Lander 2; MPF = Mars Pathfinder; Gu = *Spirit* at Gusev, MP = *Opportunity* at Meridiani Planum, PHX = *Phoenix*, Ga = *Curiosity* at Gale. Diamonds correspond to properties adopted by Costard et al. (2002) (cyan diamond), Morgan et al. (2010) (green diamond) and Williams et al. (2009) (red diamond). Note that the green diamond and red diamond should actually lie slightly offscale to the right. White triangles on the x-axis highlight the range of albedos observed and calculated for seasonal H$_2$O ice on Mars (0.25–0.4, see text), and the albedo of H$_2$O ice exposed near the south pole (0.3, see text). White triangles on the y-axis highlight the thermal inertias of ice at 248 K and of fresh, fluffy snow. (For interpretation of the references to color in this figure legend, the reader is referred to the web version of this article.)

4.3. Snow location prescription: the potential-well approximation

For $\sim$100 mbar CO$_2$, the model predicts melt only during the warmest season, and usually within a diurnal skin depth of the
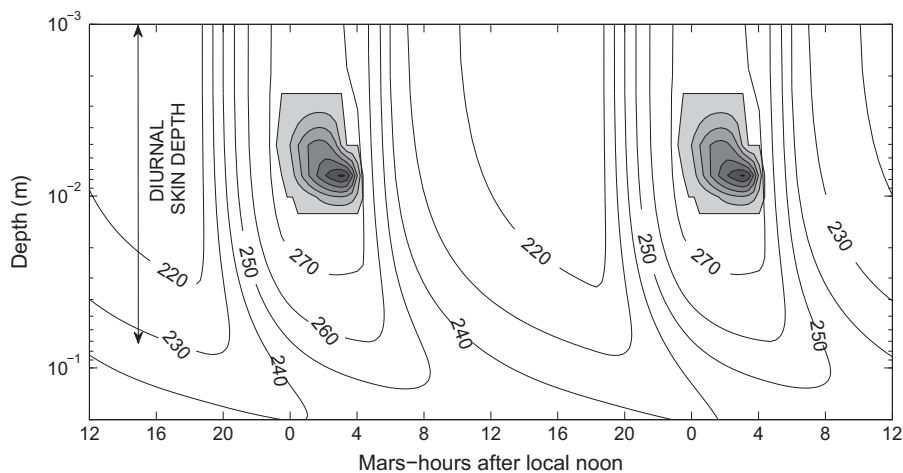
Fig. 5. Daily cycle of temperature and melting in the upper 15 cm of snowpack. Grayscale corresponds to melt fraction at a constant temperature of 273.15 K, with contours of 0.1 (edge of gray region corresponds to zero melt). Temperature contours are shown wherever the snow is not melting, at intervals of 10 K. $L_s = 0°$, $L_p = 0°$, $\phi = 50°$.

surface. Warm-season snow and ice within this depth range on Mars are near equilibrium with present-day forcing (Mellon and Jakosky, 1995; Boynton et al., 2002; Schorghofer and Aharonson, 2005; Hudson and Aharonson, 2008). Above-freezing T only leads to melt when snow is present. Therefore, we are interested in the annual-maximum T experienced by the cold traps, whose location depends on orbital conditions and topography. For most orbital conditions, this T is below freezing, so the greatest interest is in the orbital conditions that maximize the cold-traps' annual maximum T.

We find the location of cold traps for the flat-planet case as follows. For each $\mathbf{O'}$, the output of the thermal model for all seasons (L_s) and geographic locations $\mathbf{x}$ is used to determine the $\mathbf{x}$ where snow is most likely to be present during the melt season. We assume melt-season snow is only found at locations where annually-averaged sublimation is minimized (Fig. 7). To calculate annually-averaged sublimation, we use Kepler's equation to linearly interpolate thermal model output that is equally spaced in L_s onto a sequence equally spaced in time (Fig. 7). All $\mathbf{x}$ are then assigned a rank, f, scaled from 0% (global minimum in annually-averaged sublimation; most favorable for snow accumulation) to 100% (global maximum in annually-averaged sublimation; least favorable to snow accumulation). These ranks are weighted by area appropriately, so that $f = 10\%$ implies that 10% of the planet's surface area is more favorable for interannual snow accumulation. Ice lost by melting is assumed to be recovered by refreezing close (<100 km) to source. Warm-season snow is assumed not to occur above a critical f, termed f_{snow} (the percentage of the planet's surface area that has warm-season snow). Using the $f(\mathbf{x})$ and f_{snow}, warm-season snow can then be assigned to favored geographic locations (Fig. 8). The warm season is the time of fastest snow retreat, not minimum snow extent. Therefore, the critical f for warm-season snow will be greater than the critical f for interannually-persistent snow and melting does not have to be supraglacial. In fact, the most favorable set-up for aqueous alteration may be where melt occurs during a seasonal accumulation–ablation cycle which leaves bare soil during part of the year. Under this set-up, the snow is thin and bare soil is close to the zone of meltwater production.

Melting is almost certain to occur when orbital forcing leads to annual-maximum temperatures above freezing at all latitudes (Fig. 8). Thermal barriers >10 cm thick can insulate snow against diurnal melting, but a sublimation lag covering all ice is logically impossible, and a debris lag covering all ice is unlikely. Twice-yearly transfer of the entire water ice reservoir across the equator to the cold high-obliquity winter pole would require seasonally reversing mean wind speed >100 m/s.

With MOLA topography, annual-average sublimation rates are calculated as for the flat planet, but now for a range of P that spans mountaintop pressures and canyon pressures. ISEE-Mars then interpolates the latitude-P grid onto latitude and longitude using MOLA topography. This assumes that Mars' long-wavelength bedrock topography was in place before the sedimentary rock era, in agreement with geodynamic analysis (e.g., Phillips et al., 2001). This also neglects the effect of the adiabatic lapse rate on surface T, which is an acceptable approximation for the P of interest here (Section 8.1).

4.4. Integrating over all orbital states

Generating model predictions for a single $\mathbf{O'}$ requires f for each $\mathbf{x}$, the potential snowpack temperatures, and the potential melt rates. Then, f_{snow} maps out the snow distribution, and f_{snow} and ΔT together map out the melt distribution. ISEE-Mars weights the maps using the probability distribution function for $\mathbf{O'}$ (Laskar et al., 2004), and the weighted maps are summed. (Note that this

weighted mean is not the same as the median melt column from a large ensemble of Solar System integrations.) Melt likelihood is then given by

$$M_{\mathbf{x}} = \int (T_{max,\mathbf{x}} > (273.15 - \Delta T))(f_{snow} > f_{\mathbf{x}})p(\mathbf{O'})d\mathbf{O'} \quad (3)$$

where the "greater than" operator returns 1 if true and 0 if false, and $p()$ is probability.

5. Results and analysis

In this section we demonstrate the effect of different parameters on the results. This is not intended as a systematic sensitivity study, but rather as a means of providing insight into the processes at work.

5.1. Controls on the occurrence of near-surface liquid water on early Mars

By the potential-well assumption, warm-season snow locations have low sublimation rates. Sublimation depends on P (Fig. 9). Losses due to free convection decrease with increasing P, because the greater atmospheric density dilutes the buoyancy of moist air. Losses due to forced convection do not vary strongly with increasing P (Eq. (B7) in Appendix B). Surface temperature increases monotonically with increasing greenhouse forcing, leading to an uptick in sublimation rate for $P > 100$ mbar. Snow is most stable against sublimation when $P \sim 100$ mbar. Therefore, snow is most stable in topographic lows when the atmospheric pressure at zero elevation (P_o) $\ll 100$ mbar (Fastook et al., 2008). Snow is most stable on mountaintops when $P_o \gg 100$ mbar.

Melting and runoff depend on energy fluxes around the hottest part of the day. Fig. 10 shows the terms in the energy balance for a snow surface artificially initialized just below the freezing point. At low P, L_{fr} > insolation and melting cannot occur. At high P, L_{fr} is much less important. Instead, absorbed insolation and greenhouse warming are balanced principally by radiative losses and melting. The presence or absence of melt at the surface depends on the strength of conductive heating from deeper layers in the snow that are warmed by the solid-state-greenhouse effect (Fig. 10).

Both α and $\mathbf{O'}$ affect the energy absorbed by the snowpack. Considering the energy absorbed by equatorial snow at equinox:

$$E_{equinox} \approx (1 - \alpha)L_\tau \underbrace{\left(\frac{1 - e^2}{1 + e \cos \Psi} \right)^{-2}}_{distance\ from\ Sun} \quad (4)$$

where $E_{equinox}$ is the sunlight absorbed at noon at equinox, L_τ is the solar luminosity at Mars' semi major axis at geological epoch τ, Ψ is the minimum angular separation between L_p and either $L_s = 0°$ or $L_s = 180°$ (Murray and Dermott, 2000, their Eq. (2.20)), and the atmosphere is optically thin. If e is large then peak insolation need not occur at equinox. Eq. (4) shows that moving from average orbital conditions ($e = 0.06$, $\Psi = 90$) to optimal orbital conditions ($e = 0.15$, $\Psi = 0$) has the same effect on $E_{equinox}$ as darkening from albedo 0.28 to albedo zero. Albedo zero cannot produce a warm–wet Early Mars (Fairén et al., 2012).

5.2. Seasonal cycle and snow locations

Fig. 7 shows the seasonal cycle of T and sublimation rate on a flat planet. Annual average sublimation rate controls warm-season snow location, and annual-peak snow temperature determines whether melting will occur. The cold trap latitudes indicated correspond to $f_{snow} \rightarrow 0$, i.e. a single thick ice-sheet. Suppose instead that warm-season snow covers a wider area – that the "potential well"
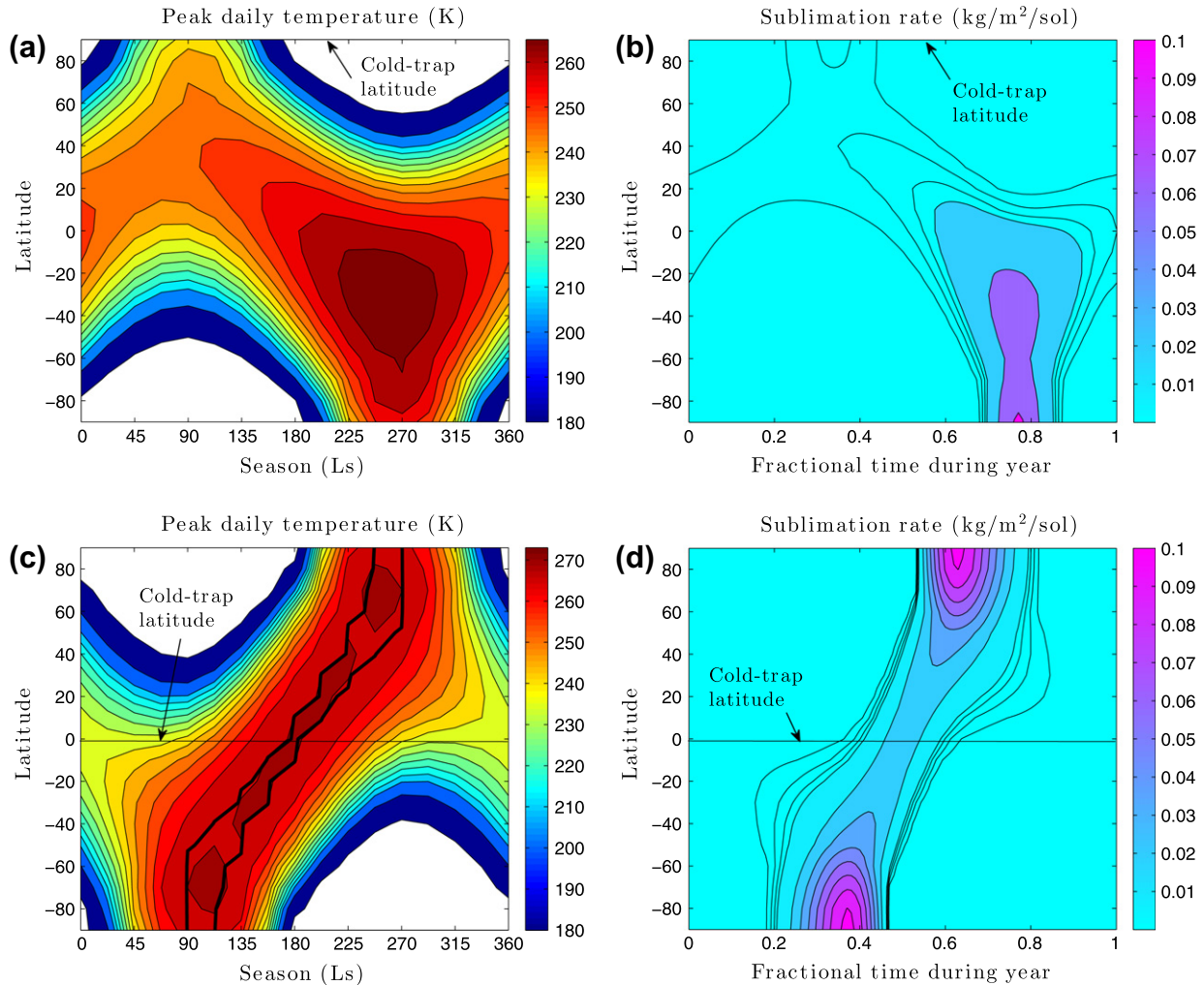
Fig. 7. Seasonal cycle of diurnal-peak temperature and diurnal-mean free sublimation rate for 3.5 Gya insolation, flat topography, and 146 mbar CO_2 atmosphere. (a and b) Current orbital forcing (ϕ = 25.2°, e = 0.093, L_p = 251°). (c and d) Optimal conditions for melting – high-ϕ, moderate e, and L_p aligned with equinox. Contours of daily maximum surface temperature are drawn at 180 K, 200 K, and 210 K and then at intervals of 5 K up to a maximum of 270 K, only reached in (c). White shading corresponds to CO_2 condensation at the surface. Sublimation-rate contours are drawn intervals of 0.025 kg/m²/sol from 0 to 0.1 kg/m²/sol and then at intervals of 0.2 kg/m²/sol. At low e and low ϕ (a and b), ice is stable at the poles, where temperatures never exceed freezing. In (c and d), ice is most stable at the equator, and diurnal-peak temperature exceeds freezing everywhere at some time during the year. The thick black line in (c) outlines the zone of subsurface melting at some time during the day. (No melting is predicted for modern orbital conditions.) The blockness of this line corresponds to the underlying seasonal resolution (22.5° in L_s). Solid-state greenhouse raises subsurface temperatures by up to several K relative to the surface.

of Fig. 8 fills up with snow. For modern orbital conditions, the area of snow stability will then extend south from the North Pole. If warm-season snow covers more than 43% of the planet – if the cold-trap effect is weak or nonexistent – then melt is possible even under modern orbital conditions. For optimal orbital conditions, increasing f_{snow} expands the melting area to form a broad band equatorward of 30°.

5.3. Snowmelt on a flat Mars-like planet

Next, we sum the maps over orbital states to find how surface liquid water varies with P. If liquid water supply limits sedimentary rock formation, this should match how geological evidence for sedimentary rocks varies with latitude.

First consider a flat planet. Suppose warm-season snow is restricted to a narrow ring at the latitude that has the lowest sublimation rate on annual average. We impose a climate that only just allows melting, and only under the optimal orbital conditions. Then:

What is the latitudinal distribution of snow, melt and melt intensity? The strongest control on Mars snowpack stability is obliquity. The 1D model predicts that snow is most stable near the equator for $\phi \geqslant 40°$, near the poles at ϕ = {0°, 10°, 20°}, and at intermediate latitudes (±55°) for ϕ = 30°, in agreement with other models (e.g., Mischna et al., 2003; Levrard et al., 2004; Forget et al., 2006; Madeleine et al., 2009) and geologic observations (e.g., Head et al., 2003). The hemisphere with an aphelion summer is favored for warm-season snow. Increasing ϕ while holding e fixed, the width of the latitudinal belt swept out by warm-season snow during a precession cycle decreases from ±26° at ϕ = 40° to ±6° at ϕ = 80° (for e = 0.09). Increasing e while holding ϕ fixed, the width of the warm-season snow belt increases from ±18° at e = 0.09 to ±22° at e = 0.16 (for ϕ = 40°).

Ninety-nine percent of melting occurs for latitudes <10°. Annual column snowmelt is further concentrated toward the equator within this narrow melt band (Fig. 11). Even though this climate has been chosen so that the probability of a melt year is tiny (~0.05%), the orbitally integrated expectation for the equatorial snowmelt column is 5 km/Gyr. This is the global spatial maximum
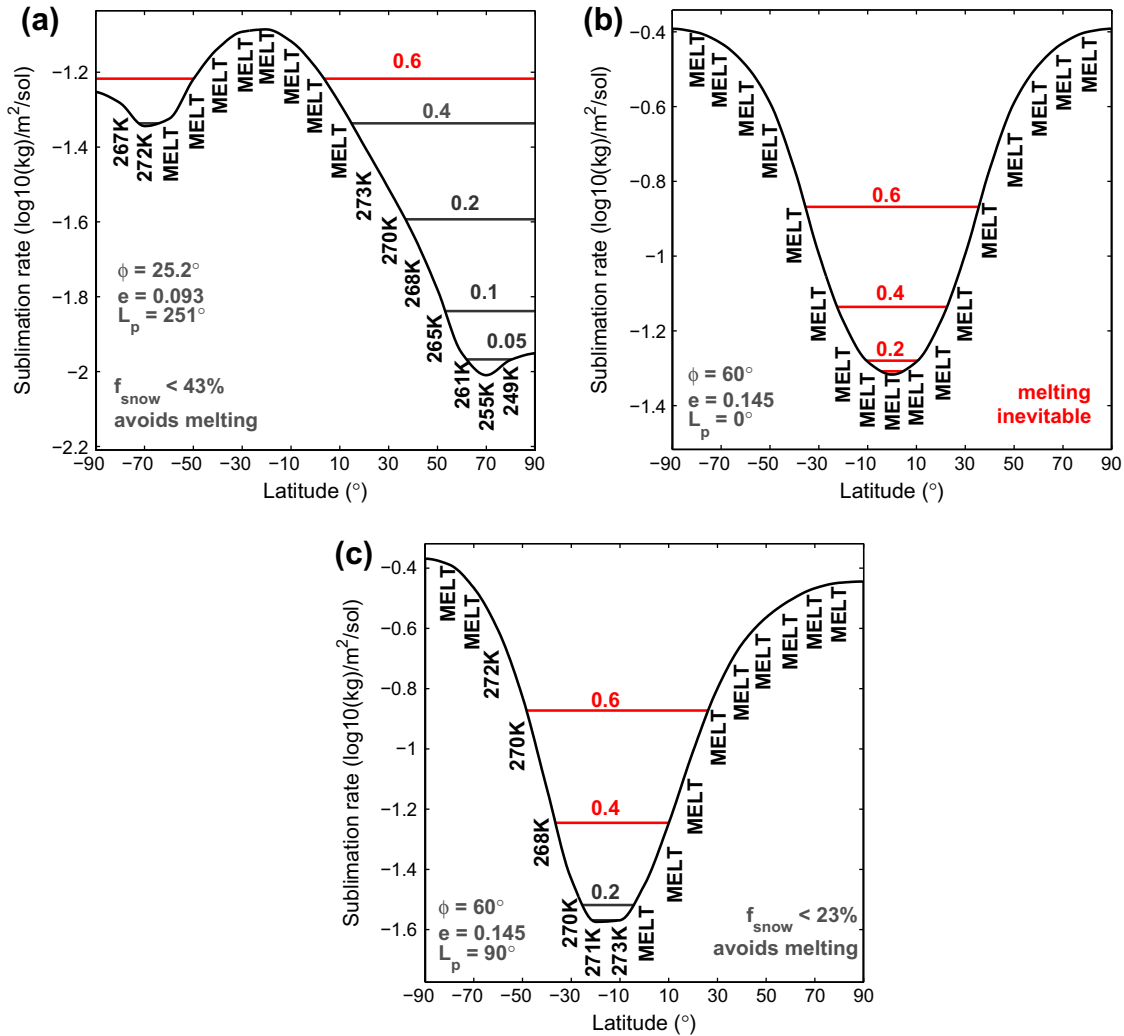
Fig. 8. The potential-well approximation for finding warm-season snow locations. Nominal parameters (Table B.1), 146 mbar atmosphere, flat topography. Curve corresponds to potential sublimation during a year. Temperatures are annual maxima. "MELT" denotes melting at some point during the year, should snow exist at that latitude. Horizontal lines correspond to f_{snow} values, assuming warm-season snow is found at locations that minimize annually-averaged sublimation, and colored red for values of f_{snow} that lead to melting. (a) Current orbital conditions. Massive ice or buried ice may exist in the southern hemisphere, but snowpack that persists through the warm-season is only likely in the far north, where temperatures are always below freezing. (b) Optimal orbital conditions. Melting occurs at all latitudes so melting is inevitable. (c) As for optimal orbital conditions, but with perihelion aligned with northern summer solstice. The short, intense northern summer displaces the potential-sublimation minimum to 20°S. $f_{snow} > 23\%$ is needed for melting to occur under these circumstances. The latitude of first melting will be near the equator. Note that '273 K' is just below the melting point.

on this flat planet. A typical Mars-year of melting produces 9 kg/m² melt at the latitude of warm-season snow, which is comparable to mean annual precipitation in the hyperarid core of the Atacama Desert. Peak instantaneous melt rate is of order 0.1 kg/m²/h. Peak rates are less sharply concentrated at the equator than annual column snowmelt (Fig. 11). Such anemic melt rates are unlikely to carve rivers. However, aqueous alteration of silicates within or beneath the snow may be sufficient to produce sulfate-bearing aeolian deposits, alongside dissolution, mobilization and re-precipitation of preexisting salts that could cement the rocks and also concentrate the salts to detectable levels. Aeolian deposits volumetrically dominate the Mars sedimentary rock record (Grotzinger and Milliken, 2012).

What is the distribution of melt and melt intensity with orbital conditions? As **C** is moved towards conditions that allow melt, melt first occurs at $\phi \geqslant 40°$ and $e > 0.13$ (Fig. 12). High ϕ is needed to drive snow to the equator, and high e is needed to bring perihelion close to the Sun (Fig. 12) (Kite et al., 2011b,c). Melting requires that the noontime Sun is high in the sky at perihelion. For the equator,

this requires $L_p \sim 0°$ or $L_p \sim 180°$). Moving Mars around a precession cycle with e and ϕ fixed, the flat planet is entirely dry between $L_p = 45°$ and $L_p = 135°$ inclusive, and between $L_p = 225°$ and $L_p = 315°$ inclusive.

What is the seasonal distribution of melt? All melting occurs near perihelion equinox. The melt season lasts $\leqslant 50$ sols (for $e \leqslant 0.145$).

How does increasing f_{snow} affect the results? Pinning snow to within $\pm 1°$ of the optimum latitude corresponds to $f_{snow} \sim 1\%$. This is similar to the present-day area of warm-season water–ice, which is the sum of the areas of late summer residual water–ice at the North and South poles. We do not know the Hesperian value of f_{snow}, but there is geologic evidence that f_{snow} can be much greater than 1% from the heights of Amazonian midlatitude pedestal craters (44 ± 22.5 m; Kadish et al., 2010). Assuming that the midlatitude pedestal craters correspond to the thickness of a single ancient ice layer of uniform thickness, and ice volume is not less than the 2.9 ± 0.3 × 10⁶ km³ volume of the modern Polar Layered Deposits (Selvans et al., 2010), the ice accumulation area is ∼46% of the planet's surface area. This ice accumulation area must be less
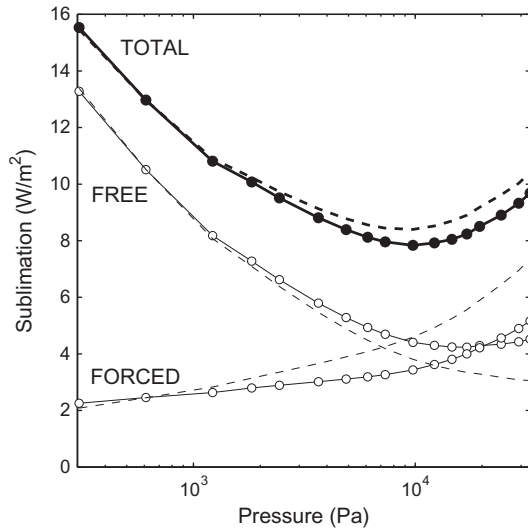
Fig. 9. Pressure dependence of diurnal-mean sublimation rate at an equatorial site. FREE is L_{fr}, FORCED is L_{fo}. Solid lines with asterisks correspond to a wind speed that declines with increasing P, dashed lines correspond to constant near-surface wind speed of 3.37 m/s. $e = 0.11$, $\alpha \approx 0.28$, $L_p = 0°$, $L_s = 0°$, $\phi = 50°$.
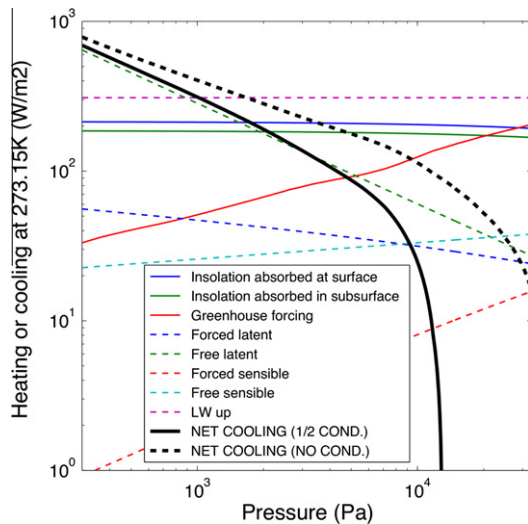
Fig. 10. Pressure dependence of the surface energy balance for $T_1 = 273.15$ K. Wind speed declines as P rises. Note that subsurface melting can occur for $T_{surf} < 273.15$ K. Rayleigh scattering reduces insolation slightly at high P. Greenhouse forcing is stronger than in the time-dependent case shown in Fig. 5 because the atmospheric temperature is assumed to have equilibrated with the relatively warm (freezing-point) T_1. If half of the subsurface absorbed insolation returns to the surface through conductive heating, then surface melting will occur (net cooling at the melting point will be negative) for $P \gtrsim 130$ mbar. However, if none of the subsurface absorbed insolation conductively warms the surface, then surface melting will not occur even for the highest P shown (~330 mbar). S_{fo} and L_{fo} are weak because of the low surface roughness. $e = 0.15$, $\alpha \approx 0.28$, $L_p = 0°$, $L_s = 0°$, $\phi = 50°$.

than f_{snow}, suggesting that thin and extensive water ice deposits have occurred on Mars. In addition to these kilometer-scale pedestals, decameter-scale pedestals suggest a widespread equatorial ice deposit in the geologically more recent past (Mitchell, 2004; Maarry et al., 2012; Schon and Head, 2012). These observations motivate calculating melt distribution for $f_{snow} = 50\%$.

At $f_{snow} = 50\%$ in ISEE-Mars, the melt belt thickens to ±33°, with minor melt activity around ±50° (Fig. 11). Maximum annual column melt and melt rates are at ±22°, where column melt is 5× greater (98 km/Gyr) and peak melt rates are 3× greater than at the equator. Peak melt rates now reach 0.7 mm/h, so runoff is

conceivable (Fig. 11). Provided that $\phi \geqslant 40°$, melting can now occur for any value of L_p and most e. There is still a very strong increase of melting with increasing e. Melt is strongest in the Northern Hemisphere at $15° < L_p < 45°$ and $135° < L_p < 165°$. It is strongest in the Southern Hemisphere at $195° < L_p < 225°$ and $315° < L_p < 345°$. This is because the belt of warm-season snow is now so wide that it partly overlaps the hot zone for all L_p. The edge of this belt closest to the pole with the highest peak temperatures sees the Sun at zenith near perihelion, when perihelion occurs near equinox. The dramatic increase in melting for $f_{snow} = 50\%$ does not require any change in greenhouse forcing or paleopressure, just a change in the way the climate system deposits snow.

How does changing atmospheric pressure affect snowmelt? At 293 mbar, which is the highest P we considered, low values of f_{snow} produce a broad band of melting between ±(15 and 20)°. There is a secondary peak around ±50°. The equatorial maximum in melt rate bifurcates at $f_{snow} \geqslant 35\%$, forming low-latitude peaks symmetric about the equator. Further increases in f_{snow} cause these maxima to drift to higher latitudes. These patterns are similar at 98 mbar and 149 mbar, although the peak melt rates and expected-seasonal-mean melt rates are both lower because of the reduced greenhouse effect. At 49 mbar, melting only occurs for $f_{snow} > 35\%$, and never at equatorial latitudes. Lower P further restricts melting to high f_{snow} and higher latitudes. This is because of the need for a long day-length (or perpetual sunlight) to warm the snowpack at low P. This is not possible at the equator, which never receives more than ≈12 h of sunlight. The melt rate under orbital conditions that are optimal for melting can be thought of as a potential well in latitude, with maxima at high latitudes (for high-ϕ polar summer), and a minimum near the equator. At low P the melt potential is zero at low latitudes, so large values of f_{snow} are needed for melting, which will then occur away from the equator. Increasing P shifts melt rate upwards everywhere, and for $\gtrsim 98$ mbar melt potential exists even at the equator, allowing melting as $f_{snow} \rightarrow 0$. If Mars had a relatively thick >0.1 bar atmosphere during the sedimentary-rock era, then progressive inhibition of equatorial melting should be a latitudinal tracer of Mars atmospheric loss.

Our flat-planet results have strong echoes in the geologic record of ancient Mars. The distribution of evidence for liquid water shows strong latitudinal banding: sedimentary rocks are concentrated at <15° latitude but have "wings" at 25–30°S and 20–30°N, and alluvial fans are most common at 15–30°S (Kraal et al., 2008; Wilson et al., 2012).

5.4. With MOLA topography

ISEE-Mars shows similar latitudinal trends whether run with MOLA topography or no topography. This is because nominal model parameters produce snow distributions that are more sensitive to latitude than to elevation.

Snow distribution shows only a weak preference for low points at $P_o = 48$ mbar and optimal $\mathbf{O}'$($\phi = 50°$, $e = 0.16$, $L_p = 0°$). However, melting only occurs in topographic lows close to the equator at low f_{snow} and $\Delta T = 2$ K (Fig. 13). $LW\downarrow$ is stronger (and L_{fr} is weaker) at low elevations, so peak temperature is higher.

For $f_{snow} = 50\%$, melting at optimal orbital conditions occurs for all low-lying locations equatorward of 30°. When perihelion is aligned with solstice at $\phi = 50°$, the snow distribution shifts away from the equator, and no melting occurs below $f_{snow} \sim 60\%$.

Low ϕ is less favorable for snow melting than high ϕ (Jakosky and Carr, 1985). For $\phi \leqslant 30°$ and perihelion aligned with solstice, snow is most stable poleward of 60°, but these locations never reach the freezing point. As f_{snow} is raised, melting will first occur at lower latitudes because these receive more sunlight. The most favored locations are S Hellas and the lowest ground around 40°N. Interestingly, these are the midlatitude locations where
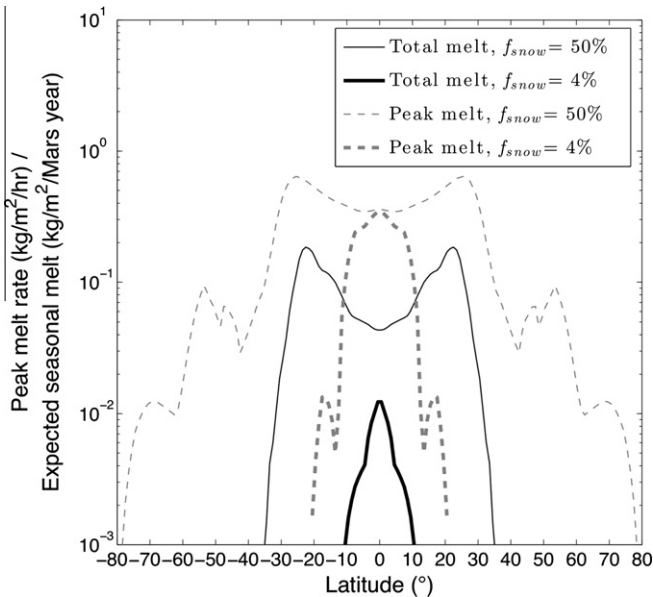
Fig. 11. Flat-planet results for a climate that only marginally rises above the freezing point. Black solid lines correspond to the orbitally-averaged melt column per Mars year (relevant for aqueous alteration). Dashed gray lines correspond to the peak melt rate experienced at any point in the orbits considered (the geomorphically relevant melt rate). Thick lines correspond to a very small value of f_{snow} (4%), and the thin lines are for f_{snow} = 50%.

scalloped depressions (e.g., Zanetti et al., 2010) and thumbprint terrain (Skinner et al., 2012) are most prominent, although these features might not require liquid water to form (Lefort et al., 2010) and these ISEE-Mars runs are not directly applicable to Middle/Late Amazonian features.
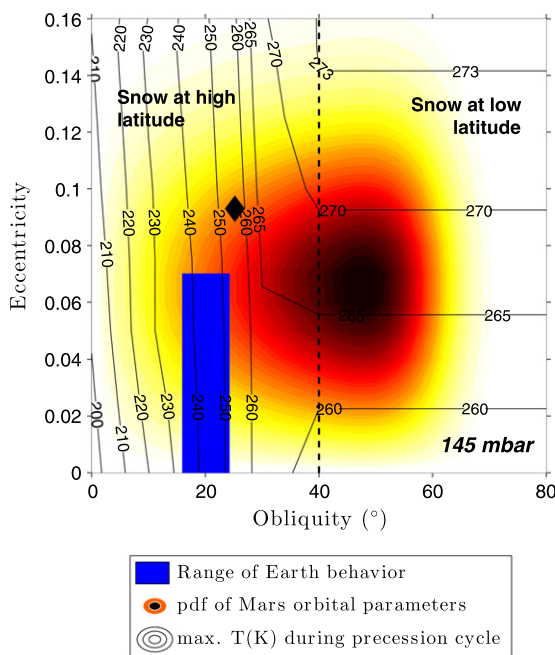
Fig. 12. Sensitivity of peak snowpack temperature to Milankovitch forcing. Maximum snowpack temperatures over a precession cycle (black contours) are highest for high obliquity and moderate eccentricity. Mars orbital elements are more variable than Earth orbital elements (probability distribution of Mars' orbital elements shown by color ramp, with white shading least probable and red shading most probable; Gyr range of Earth's orbital elements shown by blue rectangle). Black diamond corresponds to Mars' present-day orbital elements. Vertical dashed line divides $\phi < 40°$ (for which warm-season snow is generally found at high latitude), from $\phi \geqslant 40°$ (for which warm-season snow is generally found at low latitude). ΔT = 5 K, P = 146 mbar, $\alpha \approx 0.28$, Faint Young Sun, no topography.

The trade-off between P and sublimation rate controls snow stability on MOLA topography, and this sets the snow and melt distributions (Fig. 9). For example, suppose wind speed on early Mars was much higher than in our calculations. This would increase the relative importance of wind-speed-dependent turbulent losses in the surface energy balance. In turn, this would increase the importance of elevation ($\sim 1/P$) in setting snow location, relative to latitude which sets $SW\downarrow$. The snow and melt distributions for this "windy early Mars" (not shown) are broader in latitude and more concentrated in low areas (especially Northern Hellas, but also Northern Argyre and the Uzboi–Ladon–Margaritifer corridor).

5.5. Effects of climate on snowmelt distribution with MOLA topography

Integrating over the orbital-snapshot maps of melt likelihood ($\int p(\mathbf{O})d\mathbf{O}$) reveals the effect of $\mathbf{C} = \{P, \Delta T, f_{snow}\}$ on melt likelihood averaged over geological time (Fig. 14,15).

- For P_o = 49 mbar and for small values of ΔT (5 K) and f_{snow} (2%), warm-season snow is found primarily in (Fig. 14a) Valles Marineris, the circum-Chryse chaos, the Uzboi–Ladon–Margaritifer corridor, craters in W Arabia Terra, the Isidis rim, northern Hellas, Gale, Aeolis–Zephyria Planum, and parts of the Medusae Fossae Formation, as well as at high (>50°) latitudes. However, warm-season snow only melts very close to the equator (Fig. 14b) – in Gale, the circum-Chryse chaos, Meridiani Planum, Aeolis–Zephyria Planum, the Isidis rim, and the floors of Valles Marineris. Even in central Valles Marineris, among the wettest parts of the planet under this climate, melting occurs with probability <0.5% (e.g., 5 Myr of melt years during 1 Gyr). As f_{snow} is increased to 5–10% at ΔT = 5 K, melting in Meridiani Planum and Valles Marineris becomes more frequent. Melting in Northern Hellas does not occur until either f_{snow} or ΔT is greatly increased.
- As the atmosphere is lost, melting becomes restricted in space as well as time (ΔT = 5 K, P_o = 24 mbar, f_{snow} = 0.1%, Fig. 15a). The last holdouts for surface liquid water as pressure is lost are Gale, du Martheray, and Nicholson Craters in the west-of-Tharsis hemisphere, and the floors of Valles Marineris in the east-of-Tharsis hemisphere (Fig. 15a). Gale (near 6S, 135E) is usually a hemispheric maximum in snowmelt for marginal-melting climates such as this. Melting can only occur for very improbable orbital combinations under this climate. Wet periods would be separated by long dry intervals, if they occurred at all.
- At P_o = 293 mbar and low f_{snow}, low-latitude snow is restricted to high ground and so is melt. Fig. 15b shows the melt distribution for f_{snow} = 10% and ΔT = 7.5 K. For $f_{snow} \geqslant 20\%$, snow is still most likely at high ground, but the melt pattern flips: melt occurs at all elevations, but it is most common at low ground as in the low-P case. As $f_{snow} \to 100\%$, melt extent is limited only by temperature. Temperature is anticorrelated with elevation, because of the greater column thickness of greenhouse gas and because evaporative cooling is suppressed. The adiabatic atmospheric temperature lapse rate, neglected in ISEE-Mars, would also contribute to this effect at high P_0 (Section 8.3 and Forget et al., 2012).
- Hellas is usually the most favored area for snowmelt within the midlatitude ancient terrain. A climate relatively favorable for melting in Northern Hellas is shown in Fig. 15c (ΔT = 15 K, P_o = 24 mbar, f_{snow} = 40%). The contour of locally maximal snowmelt extending from deepest Hellas, to the Northern Hellas floor, to crater Terby, is intriguing because these are the locations of the thickest packages of sedimentary rock in midlatitude ancient terrain (e.g. Wilson et al., 2007, 2010). The Uzboi–Ladon–Margaritifer corridor of fluvial activity (e.g., Grant and Parker, 2002; Milliken and Bish, 2010) is the next most favorable midlatitude zone for snowmelt.

- For the wettest conditions considered (e.g., Fig. 15d: $\Delta T = 15$ K, $P_o = 49$ mbar, $f_{snow} = 40\%$), melt occurs more than 25% of the time in most places equatorward of 30°. Such wet global climates overpredict the spatial extent of both surface aqueous alteration and sedimentary rock formation on early Mars, as discussed in the next section.

6. Snowmelt in space: understanding the distribution of sedimentary rocks on Mars

6.1. Comparison to global sedimentary-rock data: implications for early Mars climate

The full climate ensemble consists of 343 orbitally integrated melt-likelihood maps similar to those in Fig. 15. To reduce this to a manageable number for analysis, k-means clustering was used (Press et al., 2007). The spatial variability of each melt-likelihood map was normalized by the within-map mean and within-map standard deviation, and clustering was carried out on these self-standardized maps. Representative results are shown in Fig. 16, together with the mean melt-likelihood maps for each of the climate clusters identified. These climate clusters were as follows:

Dark blue cluster of climates. These are perpetual-global-desert climates caused by cold, thin-atmosphere climates (Fig. 16a). Zero melting is predicted on horizontal surfaces under all orbital conditions, so no map is shown.

Red cluster of climates. At $P_o \geqslant 150$ mbar, all ΔT, and low-to-moderate f_{snow}, melting occurs at high elevation. Some melt also occurs at mid-southern latitudes. Neglect of the adiabatic lapse rate will lead to growing inaccuracy at high P_o, but will not alter the conclusion that warm-season snow will be driven to high ground at high P_o, far from the places where sedimentary rocks are observed (Fig. 16b).

Amber cluster of climates. ISEE-Mars predicts a broad swath of low latitude melting for a wide range of P_o, all ΔT, and moderate-to-high f_{snow}. Fig. 16c is effectively a map of maximum snowpack temperature – as f_{snow} becomes large, warm-season snow is no longer restricted by elevation. Melting is most intense at low elevation because there is more CO_2 overhead, but the overall pattern is diffuse in both elevation and latitude. This contrasts with the strongly-focused observed sedimentary rock distribution (Fig. 2).

Cyan cluster of climates. For $P_o < 150$ mbar and at least one of low ΔT or low f_{snow}, the model predicts focused, equatorial melting, in excellent agreement with observations (Fig. 16d). The agreement is especially notable given the simplicity of the model physics (Section 4) and the fact that we are considering one of three objectively-defined *classes* of paleoclimates rather than the optimum **C**.

We highlight seven points of data/model agreement:

(1) The thickest sedimentary rock exposures on Mars are in Valles Marineris (up to 8 km), Gale (5 km), and Terby Crater (3 km). The Medusae Fossae Formation is a sedimentary accumulation up to 3 km thick (Bradley et al., 2002) which may be aqueously cemented sedimentary rock at least in its lower part (Burr et al., 2010). Sedimentary layered deposits in the chaos regions are up to ~1 km thick (at Aram). Except for Terby, these are also the global snowmelt maxima predicted by the cyan cluster of climates. The Northern Valles Marineris canyons contain thicker sedimentary-rock mounds than the southern Valles Marineris canyons, and are correspondingly more favored for snowmelt in the model. This can be understood if unconsolidated material was not in short supply, but water for cementation was in short supply.

(2) Gale is a hemispheric maximum in ancient-terrain sedimentary rock thickness, and is a hemispheric maximum in ancient-terrain snowmelt in the model.

(3) Predicted deposit thickness dies away quickly from the predicted maxima, such that snowmelt is strongly focused in Valles Marineris, the chaos source regions, and Gale.

(4) Meridiani Planum is correctly predicted to be a local maximum within a wedge-shaped Sinus Meridiani outcrop narrowing and thinning to the East (Edgett, 2005; Hynek and Phillips, 2008; Andrews-Hanna et al., 2010; Zabrusky et al., 2012). Zooming in (not shown) confirms that the concentration of sedimentary rock in Western Arabia mound-filled craters (e.g. Crommelin, Firsoff, Danielson, Trouvelot, and Becquerel) is reproduced by the model. Alignment of Meridiani Planum with snowmelt maximum implies net True Polar Wander <10° since sediment deposition (Kite et al., 2009; Matsuyama and Manga, 2010).
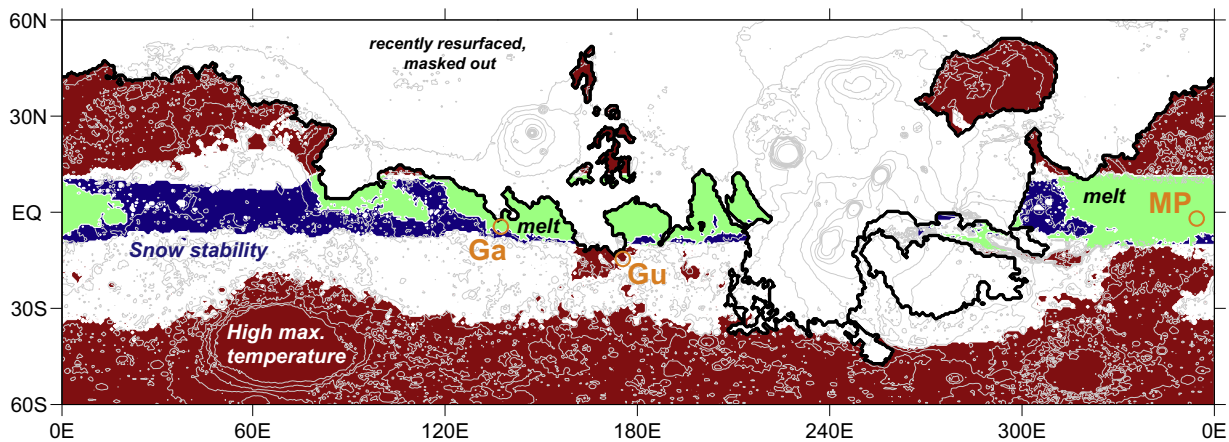
Fig. 13. Snapshot of snowmelt distribution for a single example of orbital forcing, showing role of snow stability and melting potential. $\phi = 50°$, $e = 0.145$, $L_p = 0°$, $P_o = 49$ mbar, $\Delta T = 5$ K. Blue-shaded areas correspond to $f_{snow} < 15\%$ – likely snowpack locations. Red-shaded areas receive enough sunlight for melting at some point during the year, if snow were present. Where the blue "snow stability" zone intersects the red "high maximum temperatures" zone, some melting will occur (solid green shading). Thick black line corresponds to the boundary of terrain resurfaced since sedimentary rocks formed, which ismasked out. Landing sites of long-range rovers are shown by green circles: – Ga = Gale; Gu = Gusev; MP = Meridiani Planum. Background contours are topography at intervals of 1.5 km from −5 km up to +10km. (For interpretation of the references to color in this figure legend, the reader is referred to the web version of this article.)
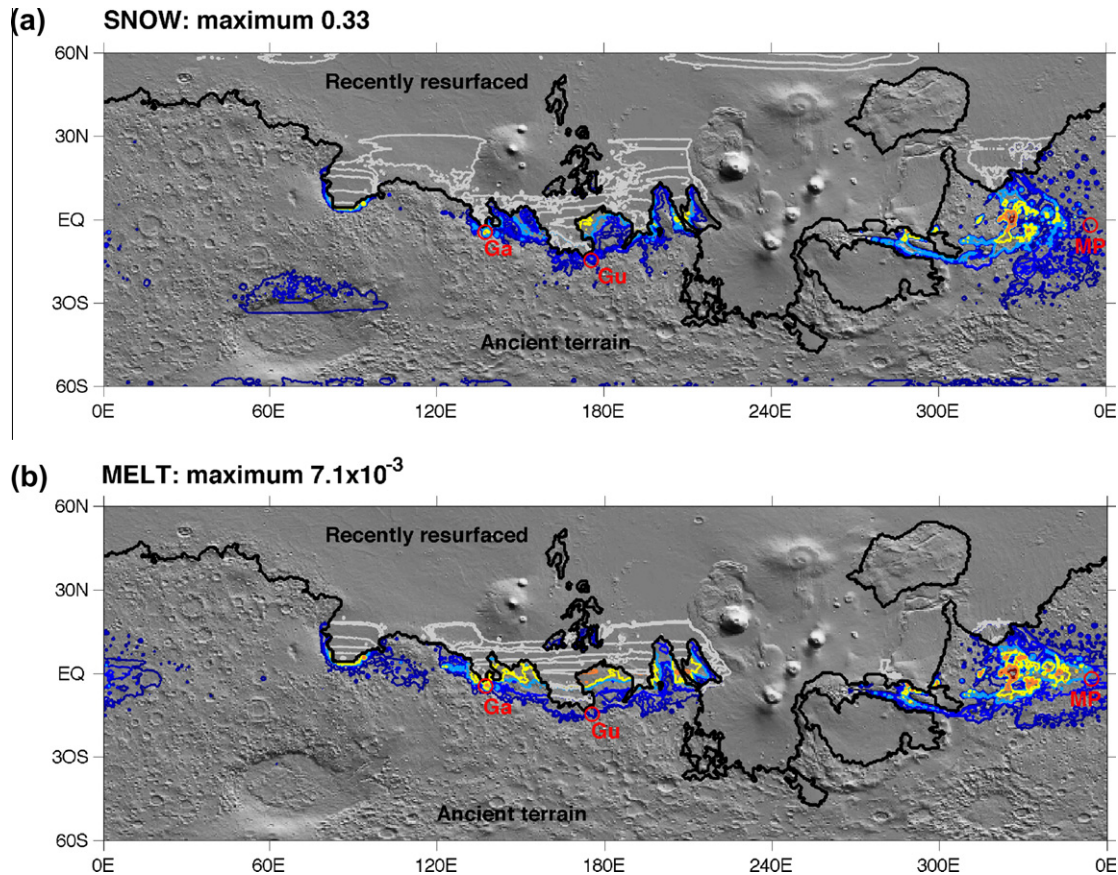
Fig. 14. Probabilities of warm-season snow (upper panel) and melting (lower panel) for P = 49 mbar, ΔT = 5 K, and f_{snow} = 2%. Background is shaded relief MOLA topography, illuminated from top right. Maximum probability on the warm-season snow map is 0.33, maximum of the melt map is 7.1 $\times$ 10^{-3} – the location is Hydaspis Chaos for both maxima. Contours are at 1%, 5%, 10%, 25%, 50%, 75% and 90% of the maximum value. The lowest colored contour in the snow map is greater than the highest colored contour in the melt map, because melting requires infrequent orbital conditions whereas warm-season low-latitude snow only requires high obliquity. Thick black line corresponds to the border of recently-resurfaced terrain, within which contours are grayed out. Landing sites of long-range rovers are shown by red circles: Ga = Gale; Gu = Gusev; MP = Meridiani Planum. (For interpretation of the references to color in this figure legend, the reader is referred to the web version of this article.)

(5) The southern rim of the Isidis basin is identified as a regional maximum for post-Noachian surface liquid water, consistent with geological mapping (Jaumann et al., 2010; Erkeling et al., 2010, 2012).

(6) Large, old equatorial craters in the Northern Plains are commonly modified by sedimentary infill (e.g., Nicholson, Reuyl). This correlation is reproduced by the model.

(7) Melting is strongly enhanced in Northern Hellas relative to other locations in the same latitude band (similarly to Fig. 15). However, $\Delta T \geqslant 10$ K is needed for non-negligible melting away from the equator, so this longitudinal enhancement is diluted in the class-average map and is not visible. A secondary enhancement within this southern latitude belt is the Uzboi–Ladon–Margaritifer corridor. These longitudinal enhancements match data on the distribution of sedimentary rocks and alluvial fans (Kraal et al., 2008). However, the model underpredicts the thickness of Terby's fill relative to the equatorial belt of sedimentary rocks.

The model predicts more snowmelt in the circum-Chryse canyons than in the Valles Marineris, but the greatest thickness of sedimentary rocks is in the Valles Marineris, not the circum-Chryse canyons. However, chaos and outflow channels formed around Chryse as late as the Early Amazonian (Warner et al., 2009), and would have destroyed sedimentary rocks deposited earlier. If the chasms were once brimful of ice, and supraglacial snowmelt crevassed to the base of the ice masses and inflated subglacial lakes

(Das et al., 2008), then seasonal melting could have contributed to chasm flooding and overflow. Alternatively, if the input rate of unconsolidated material limited sedimentary-rock accumulation in the circum-Chryse canyons, our model predicts more persistent water–sediment interaction here than at other sites. Sedimentary rocks overly chaos in Aram and Iani (Glotch and Christensen, 2005; Warner et al., 2011). The model does not predict snowmelt at Mawrth, consistent with Mawrth's interpretation as a Noachian deposit formed under a earlier climate (McKeown et al., 2009; Loizeau et al., 2012), nor does it predict snowmelt in Terra Sirenum, consistent with the nominally Late Noachian age of the inferred paleolake deposits there (Wray et al., 2011).

Red, amber, cyan and dark blue in Fig. 16 correspond to a hot-to-cold sequence in early Mars climate parameter space. The high elevation (red) and broad-swath (amber) classes have melt likelihoods as high as 0.17. The focused equatorial (cyan) class shows much lower melting probabilities ($\leqslant 0.054$) and is wrapped around the perpetual-global-desert climates (dark blue) in climate-forcing parameter space (Fig. 15a). At least one of P_o, ΔT or f_{snow} must be small to obtain a snowmelt map that matches sedimentary rock data. This assumes that sedimentary rocks accumulate in proportion to the number of years with snowmelt. Sedimentary rock formation involves nonlinear and rectifying processes such as runoff production and refreezing of downward-percolating melt. This means that years with little melt might leave no record, which could sharpen the geographically-broad swath of melting predicted by the amber cluster of climates and produce a sedimentary
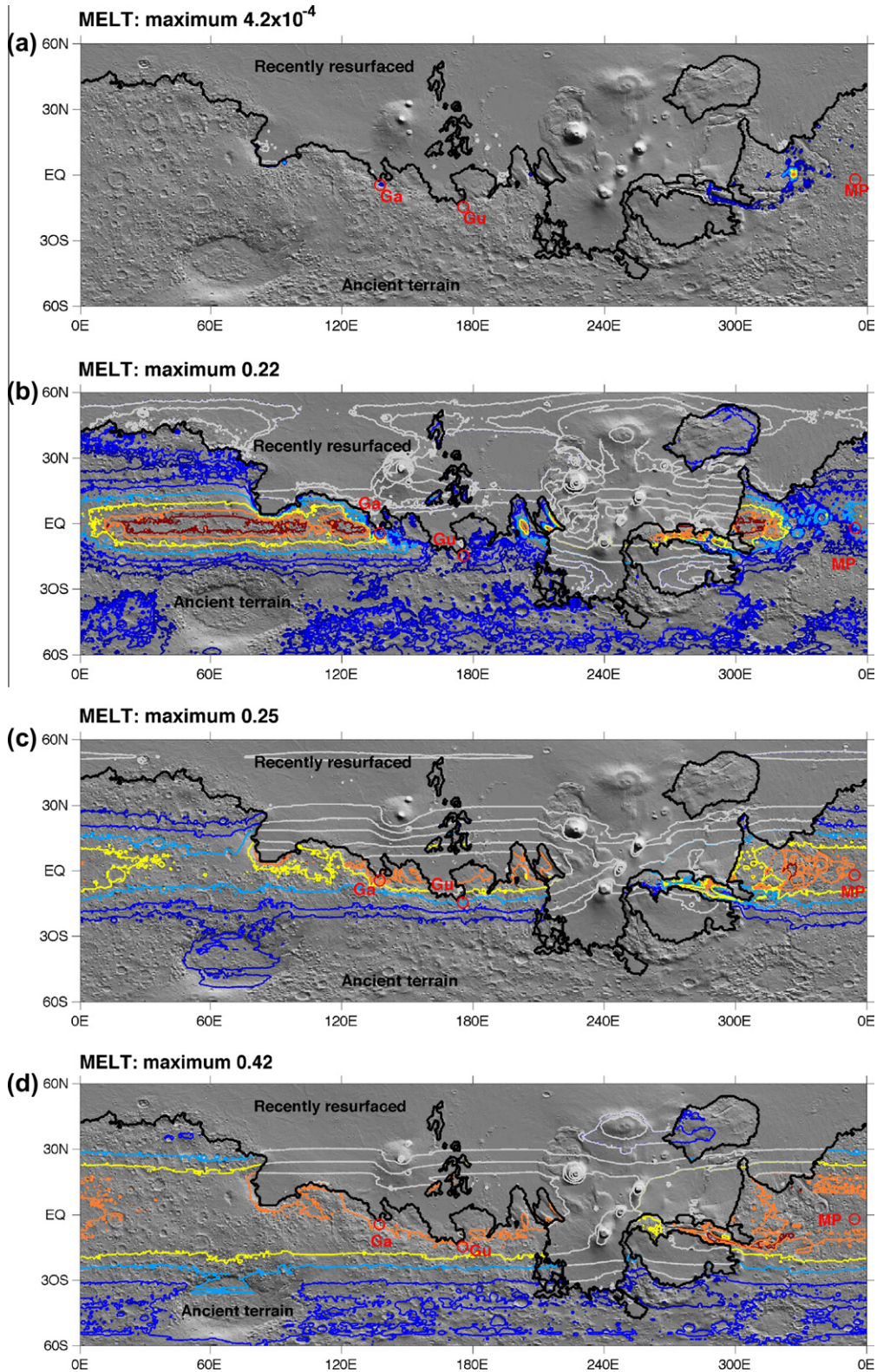
Fig. 15. Sensitivity of snowmelt maps to extreme variations in model parameters. Background is shaded relief MOLA topography, illuminated from top right. Colored contours correspond to snowmelt probabilities on ancient terrain. Contours are at 1%, 5%, 10%, 25%, 50%, 75% and 90% of the maximum melt likelihood, which is given at the top left of each panel and is different for each case. Thick black line corresponds to the border of recently-resurfaced terrain, within which contours are grayed out. Landing sites of long-range rovers are shown by red circles: Ga = Gale; Gu = Gusev; MP = Meridiani Planum. (a) Parameters that only marginally allow melting even under optimal orbital conditions: $P = 24$ mbar, $\Delta T = 5$ K, $f_{snow} = 0.1\%$. (b) High P drives snow (and melt) to high ground: $P = 293$ mbar, $\Delta T = 7.5$ K, $f_{snow} = 10\%$. This is inconsistent with the observed concentration of sedimentary rock at low elevations, but may be relevant to the distribution of older valley networks. (c) Parameters that produce snowmelt in Hellas: $P = 24$ mbar, $\Delta T = 15$ K, $f_{snow} = 20\%$. For legibility, the 1% contour is not shown for this subfigure. (d) Very high f_{snow} and ΔT predict a latitudinally broader distribution of sedimentary rocks than observed: $P = 49$ mbar, $\Delta T = 15$ K, $f_{snow} = 40\%$. (For interpretation of the references to color in this figure legend, the reader is referred to the web version of this article.)

(a)

(b)

(c)

(d)
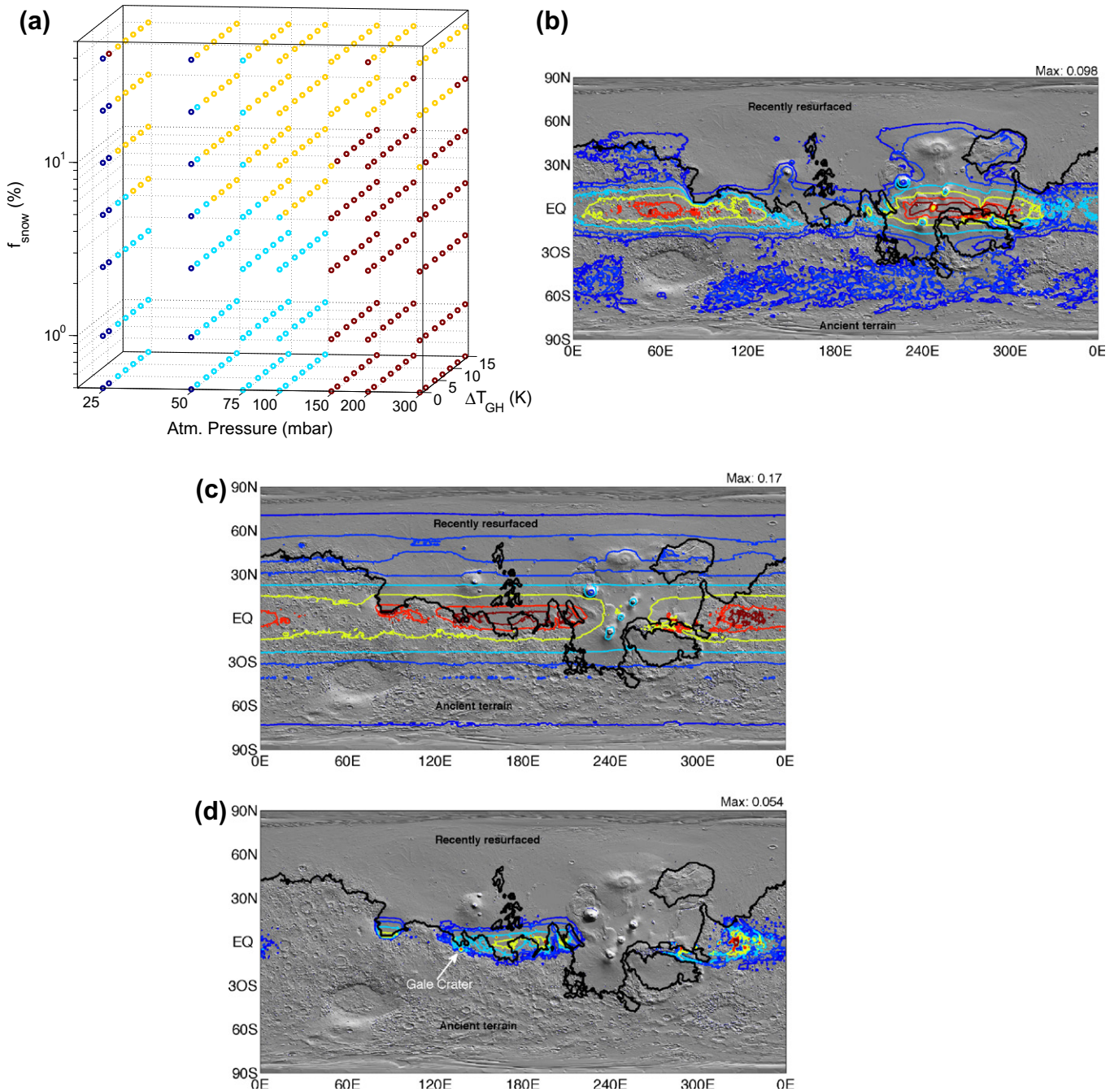
Fig. 16. Effect of climate on early Mars surface liquid water availability, assuming a snowmelt water source. Top panel shows clustering of climates into three melt-producing classes, plus perpetual-global-desert climates. (Our conclusions are not sensitive to the number of clusters used.) Remaining panels show maps of the mean of each of the melt-producing climate classes. The color of the border of each panel corresponds to the dots in the climate parameter space which contribute to that map. "Max:" to the top right of each map refers to the spatial maximum in melt likelihood, which is the probability that a given location sees some melting during the year. The colored contours correspond to melt likelihoods of 5%, 10%, 25%, 50%, 75%, and 90% of the spatial maximum for that climate class. Black line shows the boundary between ancient terrain and recently-resurfaced terrain. Compare to Fig. 2c. (For interpretation of the references to color in this figure legend, the reader is referred to the web version of this article.)

rock distribution consistent with observations. Aeolian erosion would preferentially efface thin deposits, and this could also focus a broad initial sedimentary-rock distribution. Therefore, we cannot rule out the broad-swath-of-melting (amber, high f_{snow}) climate class. Data-model comparison supports the focused-equatorial-melting climate class (cyan), and rules out the high-elevation melting paleoclimates (red class) and the perpetual global desert (dark blue).

In summary, if the seasonal-melting hypothesis is correct, Mars paleoclimate has left a fingerprint in the sedimentary rock distri-

bution. Sedimentary rocks are distributed as if Mars only marginally permitted snowmelt, even under near-optimal orbital conditions. If the wettest location on Mars was dry for $\gtrsim$ 90% of the time – which is true for the climates identified by our model as giving the best fit to the data – then Mars during the sedimentary-rock era would have been life-threateningly dry. If our model is correct, then the possibility for life is reduced but not removed, because microbial ecosystems exist in similarly hyperarid environments on Earth (Amundson et al., 2012; Wierzchos et al., 2012). The possibility for biosignature preservation is greatly reduced,

because we are not aware of any hyperarid environment with a fossil record (Summons et al., 2011).

6.2. Possible implications for valley networks, chlorides, and alluvial fans

Regionally-integrated valley networks are found over a wide range of latitudes, and record overland flow *prior* to the sedimentary rock era. The melt rates predicted by our model with nominal parameters are ≲mm/h, insufficient to form the classical valley networks. Therefore a warmer climate than the one considered in this paper is required, at least transiently. Three processes not modeled here could be explored in future work to determine if runoff from snowmelt in that warmer climate could form the classical highland valley networks: (1) a stronger greenhouse effect than considered here, with or without the orbital variability considered in this paper; (2) increasing e to ~0.22, as can occur transiently during the restructuring of Solar System orbital architecture predicted by the Nice model (Agnor and Lin, 2012); (3) transient darkenings from impact ejecta and ash, and transient heating from impact ejecta. Using the Hynek et al. (2010) database, we find that Mars valley-network elevation distribution is biased high by 600 m relative to ancient terrain, although this may reflect the generally higher elevation of mid-Noachian (as opposed to Early Hesperian) outcrop. High elevation is the fingerprint of high P_o (Figs. 15b and 16b). This suggests a geologic record of progressive atmospheric loss: P_o is >100 mbar at valley-network time (to drive snow to high ground as suggested by valley network elevations), falls to ~100 mbar by sedimentary-rock time (high enough to suppress evaporative cooling, low enough to allow sedimentary rock formation at low elevation), and falls further to the current state (6 mbar: L_{fr} prevents runoff on horizontal surfaces). This progression was independently suggested by Wordsworth et al. (2012a).

Chloride deposits ($n = 634$) are extremely soluble, generally older than the sedimentary rocks, and regionally anticorrelated with sedimentary rock (Osterloo et al., 2010). Equatorial chlorides are rare, which could be because chlorides were dissolved in the equatorial band during the melt events that lithified the sedimentary rocks. This would imply that melt rarely occurred far from the equator. Another possibility is that dust obscures chlorides at low latitudes. Either way, the large numbers of chlorides at 10–50°S excludes an erosional mechanism for the latitudinal distribution of sedimentary rocks.

Peak runoff production *during* the sedimentary-rock era is constrained to ~0.3 ± 0.2 mm/h (Irwin et al., 2005; Jaumann et al., 2010). Melt production at these rates does occur in our climate ensemble. However, peak runoff will be less than peak melting, because of refreezing, infiltration, and the damping effect of hydrograph lag time. Similar to the case of the classical highland valley networks, additional energy could be supplied by transient darkenings or greenhouse warming. An alternative way to maximize runoff at low P_o is a phase lag between the position of cold traps, which is set by orbital forcing (e.g. Montmessin et al., 2007), and the position of ice deposits. For example, an ice deposit built up at 20°S at high ϕ while $L_p \sim 90°$ may melt if it is not removed by sublimation before L_p swings back to 270°. In this paper, snow is always in equilibrium with orbital forcing (phase lag = 0°). Phase lags and ice deposits could be considered in future work.

7. Snowmelt in time: predictions for *Curiosity* at Mount Sharp

7.1. Testing snowmelt at Gale Crater's mound

The base of the Gale mound is a good place to test the snowmelt hypothesis: snowmelt is predicted at Gale for most of the paleoclimates that permit surface liquid water somewhere on Mars.[3] We think that it is not a coincidence that Gale is a good place to test the snowmelt hypothesis. *Curiosity* was sent to Gale because it hosts one of the thickest sedimentary rock packages on Mars, with mineralogic and stratigraphic hints of climate change (Wray, 2012). The snowmelt model predicts relatively abundant snowmelt at Gale (Fig. 16d), even in a changing early martian climate. Therefore, if snowmelt is the limiting factor in sedimentary-rock production, then Gale would naturally be a place that would sustain sedimentary-rock formation for a wide range of climate conditions. Gale's peak-to-moat elevation range is >5 km. When run with modern topography, the model predicts more snowmelt at the lowest elevations within Gale (the moat, and the lowest part of the mound) than at higher elevations (the rim and the top part of the mound). Before Mount Sharp accumulated, the entire Gale interior would have been at low elevation, so we predict a drying-upward sequence with most aqueous minerals deposited early (at low elevations) and few aqueous minerals deposited late (at high elevations). This is consistent with orbital spectroscopy (Milliken et al., 2010) and a new model of mound topography (Kite et al., 2012a).

Hypothesis: We hypothesize that the Gale Crater mound is an accumulation of atmospherically-transported sediments pinned in place and subsequently reworked by seasonal-meltwater-limited processes (Cadieux, 2011; Niles and Michalski, 2012).

Tests: We list predictions of the snowmelt model for Gale's mound in order of their potential to give a decisive test:

- *Mound-scale geochemistry records a succession of closed systems, not a flow-through geochemical reactor.* If the fluids responsible for alteration were in contact with the atmosphere, as is true of all the ancient waters yet sampled by meteorites and rovers (e.g., Hurowitz et al., 2010; Halevy et al., 2011), then any early-Mars climate model with $\overline{T} < 273$ K implies restriction of diagenesis to perched aquifers close to the surface (greater depths are possible beneath lakes). This predicts that the 5 km-high Gale mound is a succession of tens-to-thousands of closed systems. Alternatively, if the layers near the top of the mountain were altered by groundwater that had flowed from the bottom of the mountain, then the mountain is a flow-through geochemical reactor. In the flow-through scenario, basal layers would be vulnerable to alteration by subsequent upwelling fluids. If smectite layers are sandwiched between Mg-sulfate layers, this would place a tight upper limit on flow-through aqueous chemistry (Vaniman, 2011).
- *Wet-dry cycles on orbital timescales,* with dry conditions most of the time (Metz et al., 2009). This predicts repeatable or quasi-periodic patterns in mound geochemistry and sedimentology, with aeolian processes dominant (Kite et al., 2012a).
- *Generally homogenous chemistry and mineralogy on ascending the mound.* Except for episodic inputs of ash and impact-ejecta, the protolith is atmospherically-transported sediment with a composition that averages over global scales (for dust) or regional-to-global scales (for sand) (McSween et al., 2010). Most alteration is local, although boxwork structures have been observed and indicate fluid transport at least at the 1–10 m scale (Siebach and Grotzinger, 2012). This leaves little scope for unmixing of major-element chemistry. Reworking by wind erosion and subsequent alteration would further homogenize compositions.

---

[3] Of the subset of climate states considered that predict snowmelt anywhere on the planet, 66% predict snowmelt at the base of the Gale mound. If we say that Gale has a "robustness" of 66%, then >99% of ancient surface area scores lower for robustness. In addition, for 55% of climates modeled, the base of the Gale mound is in the top 1% of the planet for melt likelihood. If we say that the base of the Gale mound has a "maximality" of 55%, then >99.9% of ancient surface area scores lower for maximality.

- *Clay/sulfate transitions correspond to a change in protolith composition, not a change in global environmental chemistry.* At Gale and many other sites on Mars, sedimentary rocks transition upsection from irregular to rhythmic bedding (Grotzinger and Milliken, 2012). This suggests a change over time in the relative importance of transient forcing from volcanism and impacts, versus orbital forcing. Early on, large explosive eruptions and large impacts were more frequent – so many melt events were assisted by regional-to-global albedo reduction or greenhouse forcing. As volcanism and impacts declined, darkening events became less frequent, so eccentricity change (Fig. 12) emerged as the key regulator of melt events. Therefore, we predict that the phyllosilicate layers in the base of the Gale mound were altered in situ, and are stratigraphically associated with (possibly reworked) volcanic ash layers or impact ejecta (Barnhart and Nimmo, 2011).
- *Isotopic gradients.* Within a hypothetical unit representing a single identifiable melt event, isotopic trends will depend on the water loss mechanism. If the water evaporated, earlier deposits will be isotopically lighter (in H and O isotopes) and later deposits heavier. This is due to the preferential evaporation of light water and will give an O isotope trend similar to that seen within ALH84001 (Halevy et al., 2011). If the water froze instead of evaporating, later deposits will be lighter or no time dependent trend in isotopic composition will be observed. By contrast, in a global-groundwater model, if the supply of groundwater is ∼constant during mineralization, then the isotopic composition of the evaporating fluid will be some steady-state function of the evaporation rate and the isotopic composition of the upwelling fluid. Lesser variability is expected within a single deposition event.
- *No organic carbon.* Slow, orbitally-paced sedimentation and oscillation between reducing and oxidizing conditions would disfavor preservation of organic carbon.
- *No Gale-spanning lakes (except immediately after the Gale-forming impact).* Local perennial lakes are possible, as in the Antarctic Dry Valleys (Doran et al., 1998).

A complication is that layers outcropping near the base of Mount Sharp may have been buried to depths below the base of the ancient cryosphere (especially if insulated by salt hydrates; Kargel et al., 2007). Deeply buried layers may have been altered by deeper-sourced fluids, but the prediction of a horizontally-stratified early hydrosphere (Head, 2012) still holds.

7.2. From snowmelt time series to the Mount Sharp stratigraphic logs

Seasonal cycles and runoff. Early in the melt season, melt will percolate vertically and refreeze (Marsh and Woo, 1984). Infiltrating snowmelt can indurate and cement aeolian sand and dust. Flow-fingering (Albert et al., 1999) will lengthen the lifetime of subsurface melt. Refreezing of early-season melt builds an impermeable ice table which favors horizontal flow and runoff. Channelized drainage and ponding in ice-covered lakes requires that water reaches channels before it refreezes. By analogy with the Antarctic Dry Valleys, ice cover should slow further freezing once water reaches channels. Because the daily average temperature is below freezing (this is not a general requirement for seasonal-melting models, but it is a feature of the model output considered here), drainage times through firn must be <1 sol, in turn requiring high drainage density. Channel deposits with high drainage density are sometimes seen within the sedimentary rocks of Mars, feeding into much larger (and much more frequently preserved) inverted channels (e.g., Malin et al., 2010).

Milankovitch cycles. Snowmelt predictions are mapped onto sedimentology and stratigraphy in Fig. 17 (compare Fig. 1). Wet–dry cycles with period ∼20 kyr are inevitable unless $\Delta T \gtrsim 15$ K. Early in the wet phase of a wet-dry cycle, infiltration can provide water for diagenesis of layers that were deposited under dry conditions (Fig. 17). Runoff will be increasingly favored as cementation impairs infiltration. The primary control on temperature cycles is precession, with secondary control by ∼100 Kyr eccentricity cycles. Fig. 17's "STEADY ACCUMULATION" column shows sedimentological predictions for the case where sediment deposited during dry episodes is lithified by infiltration of snowmelt. Fig. 17's "WET-PASS FILTER/DISCONFORMITIES" column shows sedimentological predictions for the case where rock formation only occurs during wet intervals. Episodic reworking and further aqueous alteration is possible in either case. Preferential preservation of aeolian sediment during wet periods has been proposed for Earth – only small quantities of salt or clay cement are needed to make aeolian sediment stick in place (Nickling, 1984; Kocurek, 1998; Stokes and Bray, 2005; Hesse, 2011). Quasi-periodic liquid water availability at Gale will not necessarily produce quasi-periodic sedimentology. On Earth, climate signals at orbital frequencies are recorded with high fidelity by abyssal sediments (Pälike et al., 2006), but they are shredded by fluvial processes and barely detectable in fluvio-deltaic sediments (Jerolmack and Paola, 2010).

Sequence stratigraphy on Earth divides stratigraphic sequences into unconformity-bound packages (e.g., Shanley and McCabe, 1994). ISEE-Mars output suggests that the equivalent of sequence stratigraphy for Mars will involve mound accumulation during rare wet periods, and either bypass or mound degradation (and apron accumulation?) during more common dry periods (Kocurek, 1998; (Kite et al., 2012a).

8. Discussion

8.1. Water, dirt and sulfur: which was the limiting factor for sedimentary rock production?

Without cementation, sand and dust may accumulate but will ultimately be blown away by wind. Induration is required for strata to survive 3 Ga. We assume that cementation is the bottleneck step for making martian sedimentary rocks. The bottleneck could be earlier (piling up) or later (present-day exposure of cemented material), at least in principle.

If sediment starvation throttled early Mars sedimentary rock production, then either sediment fluxes or sediment reservoirs must have been small – but neither seems likely. Gross deposition rates for atmospherically-transported sediment on today's Mars (10^{1-2} µm/yr; Arvidson et al., 1979; Geissler et al., 2010; Johnson et al., 2003; Kinch et al., 2007; Drube et al., 2010) are not much less than past accumulation rates of sedimentary rocks: ∼30 µm/yr at Becquerel Crater (Lewis et al., 2008), ⩽20–300 µm/yr at Aeolis Dorsa (Kite et al., 2012). Planet-wide sand motion occurs on Mars (Bridges et al., 2012). Both sand and dust transport increase sharply for small increases in P (Newman et al., 2005). Mars has lost CO_2 over time (Barabash et al., 2007), and gross accumulation rates for atmospherically-transported sediment were probably $\gtrsim 10^{1-2}$ µm/yr at the $O(10^2)$ mbar level required for snowmelt. Present-day reservoirs of airfall sediment are large. For example, dust deposits at Tharsis and E Arabia Terra are $O(10)$ m thick (Bridges et al., 2010; Mangold et al., 2009). On early Mars, background dust supply would be supplemented by sediment produced during impacts and volcanic eruptions. We do not have good constraints on the current surface dust (and sand) budget and how important finite dust reservoirs are for the current dust cycle, let alone on early Mars. Therefore, applying current deposition rates to make the argument that sediment availability is not a limiting factor is fairly speculative. Nevertheless, if fluxes and
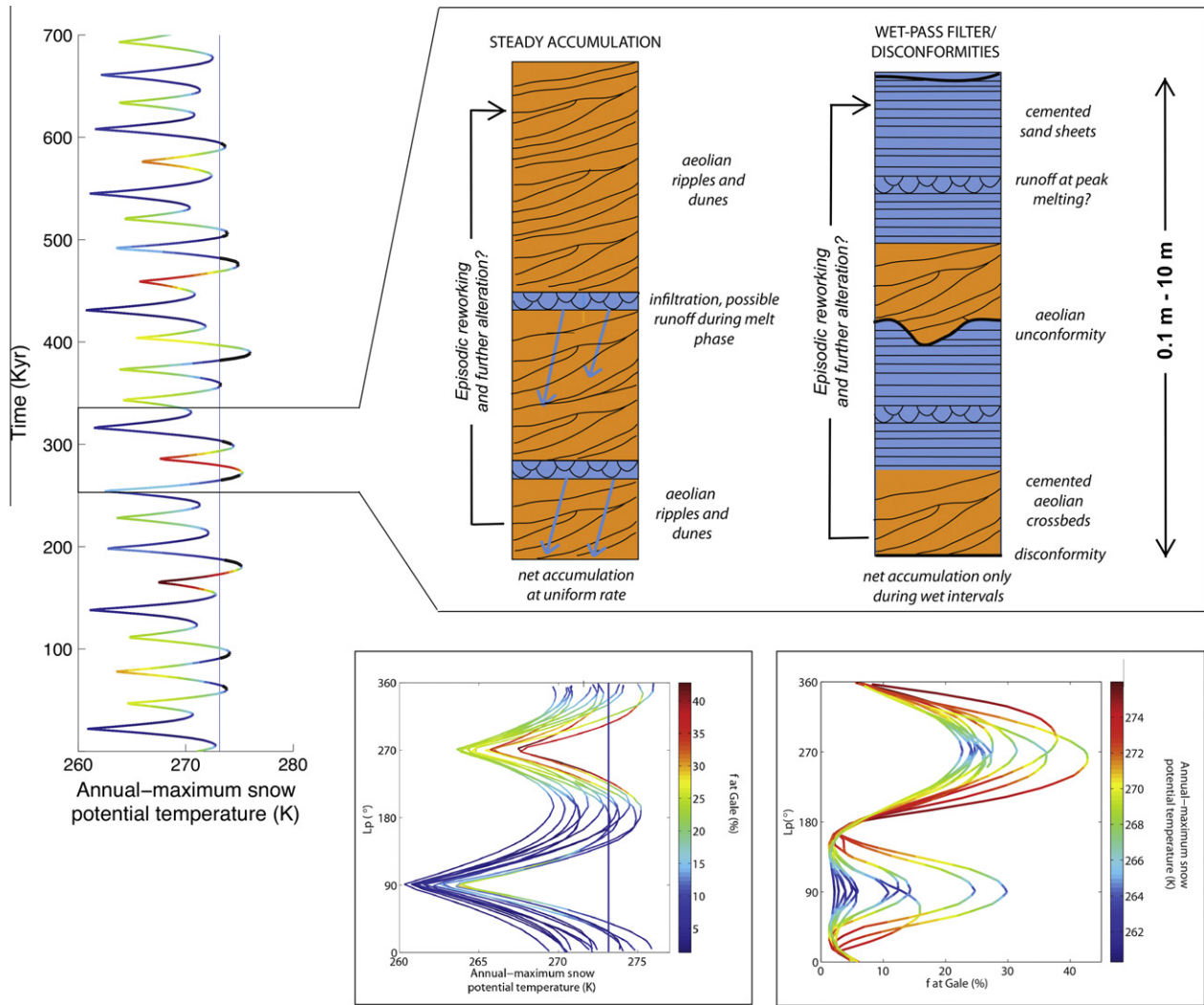
Fig. 17. Snowmelt model predictions for 700 Ka at Gale's mound (Mount Sharp, Aeolis Mons). *Left time series:* Potential temperature of snowpack at Gale ($\Delta T = 6$ K, $P_0 = 49$ mbar). The orbital forcing is realistic, but it is necessarily fictitious because the Solar System cannot be deterministically reverse integrated to 3.5 Gya. (We use Laskar solution 3O1OO3BIN_A.NOO6 for 73.05–73.75 Mya, but with 0.02 added to the eccentricity.) The color scale corresponds to *f* at Gale. Red is unfavorable for warm-season snow at Gale, and blue is most favorable for warm-season snow at Gale. The vertical blue line corresponds to the melting threshold. Black highlights intervals of melting at Gale for $f_{snow} = 10\%$. *Stratigraphic logs:* Two end-member stratigraphic responses to orbitally-paced wet–dry cycles over ~50 Kyr. Orange corresponds to sediment accumulated during dry intervals, and blue corresponds to sediment accumulated during wet intervals. In the left column, Gale's mound accumulates steadily with time, and layers are cemented by infiltration during wet intervals. In the right column, both accumulation and diagenesis are restricted to wet intervals, so Mount Sharp acts as a "wet-pass filter". *Lower panels:* Precession cycles of temperature and *f*. Imperfect cyclicity (quasi-periodicity) results from varying eccentricity. Perihelion during northern-hemisphere summer is especially favorable for snow accumulation at Gale. Gale is dry when perihelion occurs during southern-hemisphere summer: snow accumulation is unlikely, and any snow that does accumulate fails to reach the melting point. (For interpretation of the references to color in this figure legend, the reader is referred to the web version of this article.)

reservoirs were as large in the past as today, sedimentary rock formation would not have been limited by the availability of atmospherically-transported sediment. The difficulty then is to pin the sediment in place for >3 Gyr, and cementation by snowmelt is one mechanism that can resolve this difficulty.

Malin and Edgett (2000) and Edgett and Malin (2002) have suggested sedimentary rocks were once much more widespread, and that blanketing or erosion since sedimentary-rock time explains today's restricted exposure. In this view, what makes Gale special is deep moat erosion, not deep sedimentation (Edgett, 2011). At least in some craters, stratal orientations support the alternative hypothesis that mounds grew from a central core (Conway et al., 2012; Kite et al., 2012a).

Sulfate cementation requires water and S. It is possible that very early in Mars history (during relatively intense highland erosion), water was not limiting and so S was. Relatively late, it is unlikely

that S was limiting largely because of geochemical evidence for low water/rock ratios. Mars sedimentary rocks are enriched in S relative to the global soil (McLennan et al., 2010), and are estimated to contain a large proportion of the total S degassed by Mars volcanoes (Michalski and Niles, 2012). Therefore, it is necessary to explain how S became concentrated in sedimentary rocks. Acidic conditions like those observed at Meridiani Planum are likely only a part of a range of conditions that existed on the martian surface throughout its history. Charge balance of meltwater in equilibrium with the CO_2 in the atmosphere (and containing no additional ions other than sulfate) shows that only ~0.5 mM sulfate are required to reach pH ~3, if the sulfur arrived as sulfuric acid. This is also true if the sulfur comes from preexisting sulfate minerals, providing that the cations released by sulfate mineral dissolution in meltwater are precipitated as carbonates due to interaction of the solutions with the CO_2 in the atmosphere. An intense snowmelt

episode might generate $O(10^{13})$ kg of meltwater per year ($O(10^2)$ kg/m²/yr over 0.1% of the planet), and would therefore require approximately 7.5×10^{10} moles of sulfur per year for acidification. This is equivalent to approximately 10% of Earth's present volcanic outgassing rate (Halevy et al., 2007). Given the higher estimated sulfur content of martian magmas (Righter et al., 2009), this would represent a still smaller fraction of the average volcanic outgassing rate. Melting does not occur continuously, so sulfuric acid deposited onto the dry surface could partly avoid neutralization by silicate weathering and accumulate to acidify meltwater once melting occurred. Sulfur could also be contributed by preexisting and remobilized sulfates. Melting occurs episodically, with 10^{4-8}-years between episodes of melting. Volcanic outgassing of sulfur or aeolian remobilization of preexisting sediments during these dry periods "charges" the unconsolidated, mobile soil with sulfur (Catling et al., 2006), although not to the concentrations seen in the sedimentary rocks. The snowmelt model does not require initial S contents to be as high as in the sedimentary rocks we observe: once snowmelt forms, it dissolves and remobilizes the S to concentrate it in the last place that the water reached before evaporating or freezing. The sulfate may thus cement previously unconsolidated sediments in a process analogous to gypcrete formation, or accumulate in basins where water collected and evaporated. *Spirit* observations of the Peace-class rocks and the Troy deposit provide strong evidence that this S-concentrating mechanism has operated on Mars (Squyres et al., 2006; Arvidson et al., 2010).

8.2. Comparison with ice-weathering and global-groundwater models

Mechanisms for sedimentary rock formation on Mars must define sources of water, sediment, sulfur, and heat. In the ice-weathering model of Niles and Michalski (2009), the water source is an ice sheet. Sediment and sulfur is sourced from dust and gas trapped within the ice sheet. The heat source for weathering is the solid-state greenhouse effect at shallow depths, and geothermal heating as the ice is buried. In the global-groundwater model (Andrews-Hanna et al., 2010), strong greenhouse forcing warms the low latitudes to >273 K (long term average). The water source is a deep, regional-to-global groundwater reservoir, which is recharged by precipitation or basal melting. The sulfur source can be sulfide minerals, or the atmosphere. The seasonal melting model implies conditions that are warmer and wetter than the ice-weathering model, but much colder and drier than the global-groundwater model. Snowmelt under a moderately thicker atmosphere is the water source, and insolation under infrequent but expected orbital conditions supplies heat. Sediment is atmospherically transported – ice nuclei, dust-storm deposits, saltating sand, ash, and fine-grained impact ejecta – and it is trapped in the snowmelt area by aqueous cementation. The sulfur source is the atmosphere.

The main strength of the ice-weathering model is that it is (near-)uniformitarian – there is no requirement for temperatures on early Mars to have been much greater than temperature on today's Mars. Ice-sheet sulfate weathering is ongoing on Earth, and there is evidence for recent sulfate formation on Mars (Mangold et al., 2010; Massé et al., 2012). Current gaps in the ice-weathering model include the difficulty of explaining interbedded runoff features (Grotzinger et al., 2006), except as post-sulfate reworking, and a lack of a physical model for the proposed weathering mechanism.

Global groundwater models can explain the location of sedimentary rocks and the diagenetic stratigraphy at Meridiani (Andrews-Hanna et al., 2007; Andrews-Hanna and Lewis, 2011). The global groundwater model is internally self-consistent and complete. Upwelling rates are consistent with inferred sediment accumulation rates. The discovery of gypsum veins in material

eroded from the Shoemaker Formation ejecta in Endeavour Crater has been interpreted as evidence for bottom-up groundwater flow (Squyres et al., 2012), but this is inconclusive because gypsum veins are common in settings with a top-down water supply. Chaos terrain strongly suggests Mars had cooled enough to form a cryosphere that could modulate groundwater release. Therefore, even in the global-groundwater model, post-chaos interior layered deposits must have formed via a mechanism consistent with $\overline{T} < 273K$, such as spring flow (Pollard et al., 1999).

The advantages of the snowmelt model over previous models for the sedimentary-rock water source are as follows. The snowmelt model arises from a self-consistent climate solution (Sections 4 and 5). Liquid water production can "start and stop" rapidly relative to Milankovitch cycles. The equatorial concentration of sedimentary rocks arises directly from insolation (Sections 5 and 6). In the global-groundwater model, the low-latitude concentration of sedimentary rocks flows from a prescribed low-latitude distribution of recharge (Andrews-Hanna et al., 2010). Ice-weathering can take place even under modern Mars polar conditions (Niles and Michalski, 2009). In the snowmelt model, the sedimentary rocks form more or less in their current locations, with their current layer orientations, and in their current shapes. Most sedimentary rocks are now in moat-bounded mounds, filling craters and canyons. Groundwater models imply removal of $\gg 10^6$ km³ of siliciclastic rock to an unknown sink (Andrews-Hanna, 2012; Zabrusky et al., 2012). This removal is mediated by a major phase of aeolian erosion which produces the moats. Structural deformation is also required to tilt the near-horizontal primary dips expected for playa-like deposition to the observed present-day draping dips. There is no need to appeal to large-scale postdepositional modification in either the snowmelt model or the ice-weathering model (e.g. Kite et al., 2012, in preparation). Notwithstanding these advantages, the snowmelt model assumes that precipitation is uniform, but in reality it must have been spatially variable. ISEE-Mars also does not include a physical model for any of the steps linking melt generation to bedrock formation, and so it does not currently make detailed geochemical or mineral-stability predictions.

8.3. Validity of model assumptions

We neglect the lapse rate in surface temperature. Radiative fluxes set surface temperature on current Mars, so this is a good approximation for 6 mbar CO_2 atmospheres (Zalucha et al., 2010). What happens as P is increased? Results from the LMD GCM (Wordsworth et al., 2012b) show that the adiabatic lapse rate is not large at 250 mbar but is important for $P_o \sim 500$ mbar. We ran the NASA Ames Mars GCM at 80 mbar for modern orbital conditions, topography, and luminosity, as a double-check. Only a weak change in $\partial T/\partial z$ was found relative to the 6 mbar case. Both models show weak coupling of the adiabatic lapse rate to surface temperature for $P_o \sim 100$ mbar.

Atmospheric collapse to form perennial CO_2 ice caps is more likely for Faint Young Sun insolation and for ~ 100 mbar initial P (Kahre et al., 2011; Soto, 2012). However, snowmelt requires high ϕ, which is less favorable for atmospheric collapse. Will a CO_2 atmosphere that has collapsed at low ϕ reinflate on return to high ϕ? The rapid response of Mars atmospheric pressure to surface-energy-balance changes suggests that atmospheres need not stay collapsed. Dividing a 100 mbar atmosphere by the current seasonal CO_2 exchange rate of ~ 3 mbar/yr gives a reinflation time of 30 yr, much shorter than orbital change timescales of 10^4 yr. Therefore the atmosphere is relatively unlikely to be collapsed for orbital conditions that optimize snowmelt.

3D effects arising from the general circulation of the atmosphere are not included in ISEE-Mars. The most recent equatorial glaciers formed at intermediate elevations on Tharsis and Terra

Sabaea (Forget et al., 2006; Shean, 2010), associated with 3D effects such as orographic precipitation. Models disagree about where ice should precipitate under different orbital conditions (Mischna et al., 2003; Forget et al., 2006); results are sensitive to the rate of precipitation (Mischna and Richardson, 2006) and the treatment of thermal inertia (Madeleine et al., 2009). This motivates follow-up GCM work.

We assume that the freezing-point depression for melting is not very large. This is appropriate for sulfates (e.g., $\Delta T \lesssim 4$ K for the magnesium sulfate – H_2O eutectic brine), which are the most commonly reported secondary minerals in martian sedimentary rocks. Chloride brines allow liquid at much lower temperatures (Fairén et al., 2009).

We assume **C** changes more slowly than **O**, because post-Noachian rates of volcanic degassing, weathering, and loss to space are small compared to the atmospheric reservoir of CO_2. This assumption does not consider volcanic- or impact-driven transients in ΔT, nor reversible sequestration of CO_2 in ice deposits (Kreslavsky and Head, 2011; Phillips et al., 2011).

Finally, we assume no correlation between instantaneous values of e, ϕ, and L_p. Individual reverse integrations of the Solar System (obtained from http://www.imcce.fr/Equipes/ASD/insola/mars/DATA/index.html) show statistically significant correlation between e and ϕ, but the correlation coefficients are small ($|R| < 0.08$) and, more importantly, the sign of correlation varies between integrations. The weakness of these correlations justifies treating each orbital parameter independently. Mean probabilities exceed median probabilities for high e, but the exceedance probability for $e = 0.15$ is $\sim$0.8 over 4 Gya (Laskar, 2008).

8.4. Atmospheric evolution and the decline of sedimentary rock formation

Few sedimentary rocks form on Mars now, and there is minimal surface liquid water. The only evidence for liquid water at Meridiani since the current deflation surface was established is thin veneers and rinds slightly enriched in Na and Cl (Knoll et al., 2008). CO_2 escape to space is the simplest explanation for these changes, because it is known to occur today (Barabash et al., 2007). The 2013 MAVEN orbiter will constrain the present-day rate of escape to space (Jakosky, 2011). Supposing a 50–150 mbar atmosphere at sedimentary-rock time (Fig. 16, marginally consistent with Manga et al., 2012), a modern CO_2 reservoir of 12 mbar (Phillips et al., 2011), and that soil carbonate formation has been unimportant, a loss to space of $\sim$40–140 mbar over 3.5 Gya is predicted. Total loss of $\sim$40–140 mbar is higher than previous estimates of 0.8–43 mbar over 3.5 Gya from extrapolation of ASPERA-3 measurements (Barabash et al., 2007), and 2.6–21.5 mbar from fits to MHD models by Manning et al. (2011).

An alternative loss mechanism for CO_2 is uptake by carbonate weathering (Kahn, 1985; Manning et al., 2006; Kite et al., 2011a). The modern Mars atmosphere is ^{13}C-poor relative to $\sim$3.9–4.0 Ga carbonates in ALH84001 (Niles et al., 2010). If the ALH84001 carbonates faithfully record paleoatmospheric $\delta^{13}C$, this favors carbonate weathering as an atmospheric-loss process over escape to space by fractionating mechanisms, which would enrich Mars' atmosphere in ^{13}C over time (Niles et al., 2010). Carbonate exists in martian rocks, soils, and meteorites (Bandfield et al., 2003; Ehlmann et al., 2008; Boynton et al., 2009; Morris et al., 2010), but it is unclear how much of this carbonate formed *before* the sedimentary rocks. Carbonate in young soils could be reworked from older materials (McGlynn et al., 2012). A problem for carbonate-formation *during* the sedimentary rock era is that many sedimentary rocks contain sulfates, and small amounts of SO_2 make carbonate precipitation more difficult (Bullock and Moore, 2007; Halevy and Schrag, 2009).

An intriguing possibility is that a positive feedback between carbonate formation and increasing maximum temperatures led to a runaway decline in Mars' atmospheric pressure (Kite et al., 2011a). In this feedback, decreasing pressure allows the amplitude of the diurnal temperature cycle to grow, which favors melting (as pointed out by Richardson and Mischna (2005)). Liquid water availability promotes carbonate formation, so pressure decreases more steeply (Kite et al., 2011a). This positive feedback does not occur when the ground is covered with snow – strong evaporitic cooling ensures that peak temperatures decline as pressure falls (Fig. 9). However, for thin-film or dispersed-frost melting where the thermal environment is controlled by soil, evaporitic cooling is less important. Decreasing pressure may favor thin-film or dispersed-frost melting.

Theory predicts that Mars' mean obliquity has jumped between high and low values many times in the past 3.5 Ga (Laskar et al., 2004), so orbital change is not a theoretically attractive explanation for Mars' long-term drying trend.

8.5. What could allow streams to flow on early Mars?

This paper has emphasized infrequent, but expected, orbital conditions as a driver of melting (Figs. 12 and 18). Other drivers are possible. Deposition of ash or fine-grained ejecta can drive transient runoff events by lowering albedo (Fig. 6, Eq. (4)). Dark unweathered silicates provide the trigger for their own alteration by darkening the snow. In addition to Mount Sharp (Section 7.1), albedo reduction may have supplied meltwater for phyllosilicate formation at Mawrth: a regionally extensive, layered deposit possibly formed by top-down weathering of ash (e.g., Michalski and Noe Dobrea, 2007; McKeown et al., 2009; Noe Dobrea et al., 2010). Layered clays generally predate the sulfate rocks. The decline of volcanism and impacts in the Early Hesperian is consistent with the hypothesis that albedo reduction is needed to make clays. Albedo effects are the primary regulator of spatial and temporal melt production in the Antarctic Dry Valleys (e.g., Hall et al., 2010). Sharp increases in melt rate followed experimental dusting
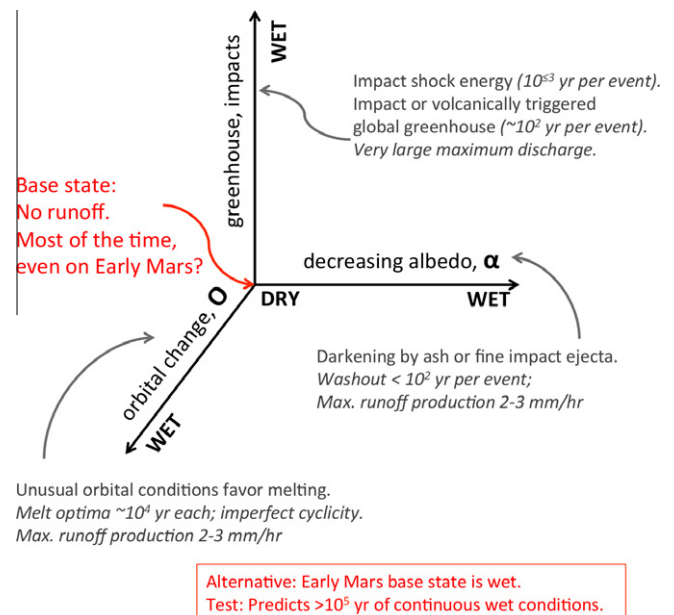
Fig. 18. Three routes to runoff on early Mars. Assuming runoff did not occur during most years on early Mars, runoff can be produced by perturbing orbital conditions, reducing albedo, heating from greenhouse forcing or impact shock energy, or some combination (black axes). All mechanisms can produce runoff $\sim$1 mm/h, but are distinguishable (gray arrows) by their limiting runoff and by their timescale.

of an Antarctic Dry Valleys glacier surface with 13–100 g/m^2 fine sand (Lewis, 2001). Dry Valleys snowpack melts faster when it is buried beneath sand, provided the sand cover is mm–dm thick (Heldmann, 2012).

Heating from longwave forcing or conduction (ΔT or impact ejecta heating) could also drive melting. Increased $LW\downarrow$ could result from clouds (but see Colaprete and Toon, 2003 and Wordsworth et al., 2012a) or short-lived pulses of volcanogenic gases (Halevy et al., 2007; Johnson et al., 2008; Tian et al., 2010; Halevy and Head, 2012).

A bright young Sun would provide more energy for melting on early Mars. This paper uses a standard solar model (Bahcall et al., 2001) that is consistent with solar neutrinos and helioseismology, but not elemental abundances in the photosphere (Asplund et al., 2005). Enhanced mass loss from the young Sun would help resolve this discrepancy, and would make the young Sun more luminous (Sackmann and Boothroyd, 2003; Guzik and Mussack, 2010; Turck-Chièze et al., 2011). To change the conclusion that the Sun was faint at the time the sedimentary rocks formed, the subsequent solar mass loss rate must have been two orders of magnitude higher than inferred from nearby solar-analog stars (Wood et al., 2005; Minton and Malhotra, 2007).

Future work could determine which mechanism is responsible using geologic observations and paleohydrology to constrain discharge and timescale. Albedo reduction events are short-lived, with runoff production that cannot exceed 2–3 mm/h, and should be most common downwind of the large volcanoes (Kerber et al., 2012). Optimal orbital conditions are relatively long-lived, but again runoff production is limited by sunlight energy and cannot exceed 2–3 mm/h (Fig. 6). Volcanic- or impact-driven events are short-lived, but with potentially very large discharge (e.g., Mangold et al., 2012).

The climates considered in this paper are extremely cold. Melt production is comparable to the coast of Antarctica (Liston and Winther, 2005). These climates can produce enough water for aqueous alteration, but struggle to match peak-runoff constraints. In a contribution that became available while this paper was in review, Wordsworth et al. (2012a) reaffirm the conclusion of Haberle (1998) that warming early Mars to $\overline{T} \sim 273$ K with a CO_2/H_2O greenhouse is hopeless, using a detailed model that tracks warming from CO_2 and H_2O clouds. Like us, they obtain small amounts of melting with dusty, low-thermal-inertia snow, and find that that additional forcing (ΔT) is needed to generate large amounts of runoff. One possibility is that cementation of the sedimentary rocks is the result of optimal orbital conditions, but that river deposits interbedded with those highly erodible sediments (Williams, 2007) record additional transient (non-orbital) warming. Future work could explore warmer snowmelt-producing climates, comparable to the coast of Greenland.

9. Summary and conclusions

Our paper has two objectives. First, we have presented a seasonal melting framework for Mars, ISEE-Mars, that relates candidate paleoclimate parameters to the production of seasonal meltwater. This framework has potentially broad applications. Second, we have applied the model to a specific problem: the origin and distribution of sedimentary rocks on Mars. Our approach has several novel elements:

- Cold-trap tracking using the potential well approximation (Section 4.3).
- Integrating over all orbital conditions (Section 4.4).
- k-means clustering of climate model output for comparison to data (Section 6).

Seasonal melting on Mars is the product of tides of light and tides of ice, which move around the planet on Milankovitch timescales. The peaks of these tides infrequently intersect, and melting can occur when they do. This meltwater may contribute to sedimentary rock cementation.

The main conclusions from our study are as follows:

(1) Order-of-magnitude calculations indicate that snowmelt is a sufficient water source for sedimentary rock cementation on a cold early Mars.
(2) Sedimentary rocks on Mars are narrowly concentrated at equatorial latitudes and at low elevations.
(3) Spin–orbit conditions for snowmelt in cold traps on Mars are optimal when obliquity is high, eccentricity is high, and longitude of perihelion is aligned with equinox. Melting then occurs in the early afternoon, at the equator, during perihelion equinox season.
(4) A model of snowmelt on early Mars has been presented, which uses a potential-well approximation to track cold traps for all orbital conditions. Integrated over all orbital conditions on an idealized flat planet with a ~100 mbar pure CO_2 atmosphere, and assuming snowpack with the albedo of dust, ISEE-Mars predicts a narrow equatorial concentration of snowmelt. This assumes that warm-season snow is tightly confined to cold traps. ISEE-Mars predicts a broad low-latitude belt of snowmelt if warm-season snow is more broadly dispersed.
(5) When MOLA topography is used, atmospheric pressure $\gg$ 100 mbar drives snow to high ground. High f_{snow} allows snowmelt on low ground even at high P. Sedimentary rocks are not on high ground, so either f_{snow} was high, snowmelt was not the water source for the sedimentary rocks, or P was $\lesssim$100 mbar at the time of sedimentary rocks.
(6) With MOLA topography, a large swathe of parameter space produces a snowmelt distribution that is a good match to sedimentary rock locations. Enough water is produced to satisfy mass balance for aqueous alteration of sedimentary rock.
(7) Within our model framework, cold early Mars climate states give the best fit to the spatial distribution of sedimentary rocks on Mars. Much warmer climates would lead to extensive snowmelt over a large swath of the planet, inconsistent with observations.
(8) Climates that allow surface liquid water anywhere usually predict snowmelt at Gale. Therefore, if Curiosity finds that snowmelt did not make a major contribution to sedimentary rock formation at Mount Sharp, this would be a decisive failure for our model.
(9) Specific predictions for MSL at Gale's mound include generally homogenous aqueous chemical processing on ascending the mound, and wet/dry orbital cycles, with wet events only during optimal conditions. Evidence for vertical fluid flow over distances comparable to the height of Gale's mound would be a major failure of the model presented here.
(10) This is the first physical model to identify Gale as a hemispheric maximum for sedimentary rock formation on Mars. ISEE-Mars therefore has the potential to relate observations at Gale to global habitability. We have presented a minimalist model in which potentially habitable surface conditions are severely restricted in space and time.

Table B.1
Selected parameters and variables. NSSDC = National Space Science Data Center.

Symbol	Parameter	Value and units	Source/rationale
Fixed parameters			
A_{vonk}	von Karman's constant	0.4	
C_p	Specific heat, Mars air	770 J/kg/K	
C_s	Specific heat capacity of snow	1751 J/kg/K	Carr and Head (2003)
D_{air}	Mechanical diffusivity of air	14×10^{-4} m^2/s	Hecht (2002)
g	Mars surface gravity	3.7 m/s^2	
k_b	Boltzmann's constant	1.38×10^{-23} m^2 kg s^{-2}	
k_{snow}	Thermal conductivity of snowpack	0.125 W/m/K	Carr and Head (2003)
m_c	Molar mass of CO_2	0.044 kg	
m_w	Molar mass of H_2O	0.018 kg	
M_w	Molecular mass of H_2O	2.99×10^{-26} kg	
$P_{atm,0}$	Current atmospheric pressure	610 Pa	NSSDC
L_e	Latent heat of water ice sublimation	2.83×10^6 J/kg	Hecht (2002)
L_e	Latent heat of water ice melting	3.34×10^5 J/kg	Hecht (2002)
r_h	Relative humidity	0.25	
R_{gas}	Gas constant	8.3144 J/(mol K)	
$u_{s,ref}$	Reference near-surface wind speed	3.37 m/s	Millour et al. (2008) "MY24" average
z_o	Roughness length	0.1 mm	Polar snow Brock et al. (2006)
z_{anem}	Anemometer height	5.53 m	Millour et al. (2008)
α	Albedo	≈0.28	Albedo of dusty snow
ϵ	Emissivity of ice at thermal wavelengths	0.98	
v_{air}	Kinematic viscosity of air	6.93×10^{-4} m^2/s	Hecht (2002)
ρ	Density of snowpack	350 kg m^{-3}	Carr and Head (2003)
ρ_0	Density of atmosphere (now)	0.02 kg m^{-3}	NSSDC
σ	Stefan–Boltzman constant	5.67×10^{-8} W m^{-2} K^{-4}	
τ	Time of interest	3.5 Gyr ago	Murchie et al. (2009b)
	Mars semimajor axis	1.52366 AU	NSSDC
	Duration of 1 Mars sol	88,775 s	
	Dust concentration	~2% by volume	Appendix C
	Dust radius	4 μm	Appendix C
	Ice grain radius	1 mm	Appendix C
	Solar constant (now)	1.361×10^3 W/m^2	Kopp and Lean (2011)
Selected variables			
O	Spin–orbit properties		
O′	Milankovitch parameters		
C	Climate parameters		
ϕ	Obliquity	0–80°	
b_{DB}	"b" of Dundas and Byrne (2010)	$f(P)$ (Appendix B)	Extrapolation from GCM runs
e	Eccentricity	0.0–0.16	
L_p	(Solar) longitude of perihelion	0–360°	
L_s	Solar longitude	0–360°	
M	Mean anomaly	0–360°	
P	Atmospheric pressure	24–293 mbar	
P_o	Atmospheric pressure at zero elevation	24–293 mbar	
ΔT	Non-CO_2 greenhouse forcing	0–15 K	
f_{snow}	Fraction of planet surface area with warm-season snow	0–50%	
Q_k	Fraction of incident sunlight absorbed at level k	0–100%	
$LW\downarrow$	Greenhouse forcing		
$LW\uparrow$	Thermal emission by surface		
$SW\downarrow$	Insolation		
s_r	Rayleigh scattering correction factor		
L_{fo}	Latent heat losses by forced convection		
L_{fr}	Latent heat losses by free convection		
S_{fo}	Sensible heat lost by forced convection		
S_{fr}	Sensible heat lost by free convection		

Appendix A. Data analysis

The MOC NA sedimentary rock database is probably a good proxy for the true distribution of sedimentary rocks on Mars, even though MOC NA did not sample the planet uniformly. MOC NA

took 97,000 images of Mars and about 4% showed sedimentary rocks (Malin et al., 2010) (http://marsjournal.org/contents/2010/0001/files/figure16.txt). Although MOC NA imaged only 5.5% of Mars' surface (Malin et al., 2010), the Mars Reconnaissance Orbiter Context Camera (CTX) has surveyed >75% of the planet at comparable resolution to MOC NA (April 2012 Malin Space Science Systems press release, http://www.msss.com/news/index.php?id=43) and has not found large areas of sedimentary rock missed by MOC NA. MOC NA targets were selected on a 1-month rolling cycle, and sedimentary rocks were among the highest scientific priorities of the MOC NA investigation (Malin et al., 2010). In the same way that oil wells are drilled more frequently in productive basins, there is a high density of MOC NA images in areas of sedimentary rocks that were identified early in the mission. Regardless, there is little difference between maps of the relative abundance of sedimentary rocks defined using the fraction of MOC NA images showing sedimentary rocks within a given spatial bin versus maps defined using the absolute number of sedimentary rock observations in a given spatial bin. We assumed sedimentary rock locations are close to image-center coordinates. We exclude orbits early in the MOC NA mission, which can have large image footprints.

The Terra Sirenum drape deposit (Grant et al., 2010) and a large part of the Medusae Fossae Formation (Bradley et al., 2002) are sedimentary in origin, but are excluded by the definition of sedimentary rock used by the MOC NA team. These omissions from the database have little or no effect on our data-model comparison. The Terra Sirenum drape deposit has a phyllosilicate-rich mineralogy that is distinct from the sulfate-bearing sedimentary rocks that are the focus of this paper, while ISEE-Mars consistently predicts the entire Medusae Fossae Formation to be a global near-maximum in sedimentary rock accumulation.

Because the abundance of sulfate-bearing sedimentary rocks peaks in the Hesperian, Terminal Hesperian and Amazonian terrain may conceal underlying sedimentary rocks and should be excluded from the analysis. We traced the edge of these young materials using the USGS Mars Global GIS (ftp://pdsimage2.wr.usgs.gov/pub/pigpen/mars/Global_GIS_Mars/) as a basemap. The resulting young-terrain mask excludes 45% of the planet, but only 3.5% of the images of sedimentary rocks ($n = 105$). These 3.5% are mostly from the Medusae Fossae Formation and the plateaux surrounding Valles Marineris. These rocks appear to represent a late tail in sedimentary rock formation. We retain them in Fig. 2, but omitting them does not change our conclusions.

Appendix B. Details of thermal model

The 1D model draws on previous work by others (particularly Clow, 1987; Liston and Winther, 2005; Williams et al., 2009; and Dundas and Byrne, 2010) and by ourselves (Kite et al., 2011b,c).

B.1. Radiative terms

A line-by-line radiative transfer model of the atmosphere (Halevy et al., 2009) is used to populate two look-up tables: $LW\downarrow$ as a function of T_1 and P; and $SW\downarrow$ as a function of P and solar zenith angle. The radiative transfer model, which for simplicity assumes a clear-sky, pure CO_2 atmosphere with no clouds or dust, is not run to radiative-convective equilibrium. Instead, for each combination of surface P, T, α, and solar zenith angle, an atmospheric P–T structure is prescribed and the resulting radiative fluxes are calculated. Following the approach of Kasting (1991), the tropospheric lapse rate is dry adiabatic and the stratosphere is approximated as isothermal with a temperature of 167 K. A two-stream approximation to the equations of diffuse radiative transfer (which

accounts for multiple scattering) is solved over a wavelength grid with a spectral resolution of $1 \, cm^{-1}$ at frequencies lower than $10,000 \, cm^{-1}$ and a spectral resolution of $10 \, cm^{-1}$ at higher frequencies. The error induced by this spectral resolution relative to high resolution calculations is small compared to the uncertainties in the other model parameters (Halevy et al., 2009). The parameterisation of collision-induced absorption is the same as in Wordsworth et al. (2010), and is based on measurements by Baranov et al. (2004) and calculations by Gruszka and Borysow (1997, 1998).

The atmospheric temperature profile that sets $LW\downarrow$ (T_r in Fig. 4) is pinned to the diurnal average surface temperature T_1. Mars' bulk atmospheric radiative relaxation time, τ_{relax}, is ~2 days at 6 mbar surface pressure (Goody and Belton, 1967; Eckermann et al., 2011), and increases in proportion to atmospheric density. τ_{relax} is much larger than a day but much shorter than a year for the P relevant to melting (>50 mbar).

B.2. Free convective terms

Our turbulent-flux parameterizations closely follow Dundas and Byrne (2010). Sensible heat loss by free convection is:

$$S_{fr} = 0.14(T - T_a)k_a\left[\left(\frac{C_p v_a \rho_a}{k_a}\right)\left(\frac{g}{v_a^2}\right)\left(\frac{\Delta\rho}{\rho_a}\right)\right]^{1/3} \quad (B1)$$

where T_a is the atmospheric temperature, k_a is the atmospheric thermal conductivity, C_p is specific heat capacity of air, v_a is viscosity of air, ρ_a is density of air, g is Mars gravity, and $\Delta\rho/\rho_a$ is the difference in density between air in equilibrium with the ground and air overlying the surface layer. $\Delta\rho/\rho_a$ is given by

$$\frac{\Delta\rho}{\rho} = \frac{(m_c - m_w)e_{sat}(1 - r_h)}{m_c P} \quad (B2)$$

Here, m_c is the molar mass of CO_2, m_w is the molar mass of H_2O, r_h is the relative humidity of the overlying atmosphere, and e_{sat} is the saturation vapor pressure over water ice. The expression for $\Delta\rho$ assumes that water vapor is a minor atmospheric constituent.

T_a is parameterized as (Dundas and Byrne, 2010)

$$T_a = T_{min}^{b_{DB}} T^{1-b_{DB}} \quad (B3)$$

where T_{min} is the coldest (nighttime) surface temperature experienced by the model, and b_{DB} is the Dundas–Byrne 'b', a fitting parameter. This is an empirical model motivated by Viking 2 measurements (Dundas and Byrne, 2010). b_{DB} decreases as P increases, because atmosphere-surface turbulent coupling strengthens. $b_{DB}(P)$ is obtained by fitting to the output of GCM runs at 7, 50, and 80 mbar which employed a version of the NASA Ames Mars GCM described in Haberle et al. (1993) and Kahre et al. (2006). Specifically, $b_{DB}(P)$ is fit to the global and annual average of the temperature difference between the surface and the near-surface atmosphere for local times from 11:00 to 13:00.

We set (Dundas and Byrne, 2010)

$$L_{fr} = L_e 0.14\Delta\eta\rho_a D_a\left(\left(\frac{v_a}{D_a}\right)\left(\frac{g}{v_a^2}\right)\left(\frac{\Delta\rho}{\rho}\right)\right)^{1/3} \quad (B4)$$

where L_e is the latent heat of evaporation, $\Delta\eta$ is the difference between atmosphere and surface water mass fractions, and D_a is the diffusion coefficient of H_2O in CO_2.

B.3. Forced convective terms

Sensible heat lost by forced convection is given by:

$$S_{fo} = \rho_a C_p u_s A(T_a - T) \quad (B5)$$

where u_s is the near-surface wind speed. Near-surface winds are controlled by planetary boundary layer turbulence which serves to mix the atmosphere vertically, so $S_{fo} \neq 0$ is consistent with the assumption of no meridional heat transport. The drag coefficient A is given by

$$A = \left(\frac{A_{vonk}^2}{\ln(z_{anem}/z_o)^2} \right) \tag{B6}$$

where A_{vonk} is von Karman's constant, z_{anem} is anemometer height, and z_o is surface roughness. The anemometer height is virtual – it is the lowest model level in Mars Climate Database (5.53 m).

Near-surface wind speed u_s in the NASA Ames Mars GCM decreases with increasing P and decreasing solar luminosity. Near-surface wind speed is 3.37 m/s in the European Mars Climate Database ("MY24" simulation, global average) (Millour et al., 2008). This is extrapolated for $P \leqslant 293$ mbar using a logarithmic dependence of u_s on P fitted to the global and annual average of Ames Mars GCM model surface wind speed for initial pressures of 7, 50 and 80 mbar. u_s is lowered by a factor of 1.08 for the Faint Young Sun using the ratio of wind speeds for two 50 mbar Ames Mars GCM simulations that differ only in solar luminosity. Simulations suggest u_s increases with ϕ (Haberle et al., 2003), but this is ignored. Fig. 8 shows the sensitivity of results to $u_s = f(P)$ versus $u_s \neq f(P)$.

Latent heat losses by forced convection are given by:

$$L_{fo} = L_e \frac{M_w}{kT_{bl}} u_s(e_{sat}(1 - r_h)) \tag{B7}$$

where M_w is the molecular mass of water, and k is Boltzmann's constant. Latent heat fluxes for dirty snow are calculated assuming that the entire exposed surface area is water ice. Because dirt concentrations are at the percent level by volume, or less, for all results presented here, this is acceptable.

The free and forced fluxes are summed together, rather than considering only the dominant term. This matches the functional form of Mars-chamber data (Chittenden et al., 2008) and is the standard approach in Mars research (Toon et al., 1980; Williams et al., 2008; Dundas and Byrne, 2010). However, summing the terms is an idealization that may overestimate cooling.

B.4. Melt handling

Melt occurs when $T_K > (273.15 \text{ K} - \Delta T)$. ΔT is a freezing-point depression. It can also be interpreted as non-CO_2 warming (due to, for example, water vapor, ice clouds, or SO_2), stochastic fluctuations in material properties around those assumed in Table B.1, or higher solar luminosity. Additional greenhouse warming (freezing point at 273.15 K) implies greater turbulent and $LW\uparrow$ losses at the melting point than freezing-point depression (freezing point at 273.15 K – ΔT), but ΔT is small so this difference is ignored here. Raising ΔT from 0 K to 5 K raises peak melt rate from 0.44 kg/m^2/h to 1 kg/m^2/h. Melt fraction reaches 1 in the shallow subsurface. Melt is produced for 6 (instead of 4) Mars-hours per sol, and there is some melt in the subsurface for 7.5 (instead of 4) Mars-hours per sol.

Total melt present and total melt produced are tracked during the sol. Melt is not permitted to drain, and the melt fraction is not allowed to affect snowpack material properties except to buffer temperature during refreezing.

Ablation of the snowpack surface by sublimation is not directly tracked. The effect on sublimation on snowpack survival is treated indirectly, through the potential-well approximation (Section 4.3). However, ablation also affects snowpack temperature. Movement of the snow surface down into the cold snowpack corresponds to advection of cold snow upwards (relative to the surface). Implied

sublimation rates are ~0.5 mm/sol for conditions favorable to melting. Snowpack thermal diffusivity is ~2×10^{-7} m^2/s. Melting at depths greater than ~$\kappa/u_{subl} \sim 4$ cm may be suppressed by this advective effect.

B.5. Run conditions

Conductive cooling is found by matrix inversion. Vertical resolution is ≈ 2.5 mm for nominal parameters, which is $0.033\times$ the analytic diurnal skin depth. Time resolution is 12 s, and the lower boundary condition is insulating. Output is stored every 100 time-steps for analysis.

The initial condition on the surface is slightly cooler than radiative equilibrium, and decays at depth with an e-folding depth equal to the diurnal skin depth to the energy-weighted diurnal average temperature. The model is integrated forwards in time for several sols using constant seasonal forcing until the maximum T_1 on successive sols has converged (to <0.01 K) and the diurnal-maximum melt column (if any) has converged to <0.018 kg/m^2. For polar summers, convergence can take an extremely long time as the melt zone spreads to cover the entire snowpack, so the integration stops after ~8 sols even if the convergence criteria are not met.

ISEE-Mars has no meridional heat transport, seasonal thermal inertia, or CO_2 cycle. Temperatures are not allowed to fall below the CO_2 condensation point. For each spatial location, the model is run for many seasons (L_s). The converged output is then interpolated on a grid equally spaced in time to recover annual means.

Details about melt-likelihood map construction. Results in this paper are based on grids of runs at $\phi = \{0°, 10°, 20°, \ldots, 80°\}$, $e = \{0, 0.03, 0.06, 0.09, 0.115, 0.13, 0.145, 0.16\}$, $L_p = \{0°, 15°, 30°, \ldots, 90°\}$ (with mirroring to build up a full precession cycle), $L_s = \{0°, 22.5°, 45°, \ldots, 337.5°\}$, and latitude $\{-90°, -80°, -70°, \ldots, 90°\}$, giving 1.5×10^6 snowpack thermal model runs for each **C**. Quoted results at intermediate values result from interpolation. Statements about **C** are based on interpolation in a grid of runs at $P = \{4, 8, 16, 24, 48\} \times 610$ Pa $\equiv \{24, 49, 98, 146, 293\}$ mbar, with $\Delta T = 0$ K. For the ensemble shown in Fig. 15, ΔT and f_{snow} were varied in postprocessing.

To remove longitudinal stripes of high snow probability in the Northern Plains that are artifacts of finite model resolution in **O′** and latitude, the step function in $(f_{snow} - f)$ is replaced by a linear ramp in $(f_{snow} - f)$. This is a minor adjustment.

Appendix C. Snowpack radiative transfer

Crystalline water ice is opaque in the thermal infrared, but almost transparent to visible light. The resulting solid-state greenhouse effect enhances snowmelt (Clow, 1987; Brandt and Warren, 1993; Möhlmann, 2010). The purpose of the solid-state greenhouse parameterization in this paper is to self-consistently model the tradeoff between snowpack broadband albedo (α) and subsurface absorption of sunlight. This does not require precisely calculating α as a function of dust content, so the model uses simple linear approximations to the radiative transfer equations developed for widely-seperated atmospheric aerosols (e.g. Kieffer, 1990; Calvin et al., 2009). Although more sophisticated models can be employed to take account of aspherical particles, near-field effects, and heterogeneous compositions (e.g. Cull et al., 2010; Yang et al., 2002), the lack of consensus on their importance leads us to not include them in our algorithm.

The solid-state greenhouse parameterization uses the snow radiative transfer model of Brandt and Warren (1993). Ice refractive indices are from Warren and Brandt (2008), and are converted to Henyey-Greenstein parameters using a standard Mie code

following Bohren and Huffman (1983). Mars dust optical parameters are calculated using the refractive indices of Wolff et al. (2006, 2009). An illustration of these parameters for the canonical atmospheric dust sizes is shown in Fig. 1 of Madeleine et al. (2011), but we also employ larger sizes as well. The 2000 ASTM Standard Extraterrestrial Spectrum Reference E-490-00 is used to describe the wavelength dependence of the direct flux component; diffuse flux is neglected as a being a minor perturbation. The young Sun was ~100 K cooler in the standard solar model. Solar reddening increases α by <0.01, so the spectral shift is ignored here. The effect of small amounts of meltwater on α is minor (Warren, 1982) and is also ignored. The effects on wavelength-dependent direct-beam semi-infinite albedo (not shown) are broadly similar to the idealized "red dust" in Warren and Wiscombe (1980). Once optical properties are prescribed, the most important variables are dust content, effective dust grain radius, and effective ice grain radius. A given α can usually be obtained by several different combinations of these properties. The Brandt and Warren (1993) model is used to build a look-up table of fractional subsurface absorption as a function of these variables, plus direct-beam path length. This length is mapped to depth within soil by multiplying by the cosine of the zenith angle.

The radiative transfer model reproduces the trends found by Clow (1987). Recent measurements increase the martian dust single scattering albedo in the optical (Wolff and Clancy, 2003; Wolff et al., 2006, 2009), which reduces the amount of melting for a given dust concentration. Ice grain size growth is slow in Mars' present day polar caps (Kieffer, 1990) but much faster under the near-melting conditions that are important for the model presented here. We adopt an effective size of 1 mm, corresponding to observed ice-grain radii in hoar layers in Earth snowpacks. Not surprisingly, there are no direct measurements of dust content in snow on Mars. Dust content in ice has been reported as "a few percent (up to at most around 30%)" by volume in the Northern Plains subsurface deposit (Dundas and Byrne, 2010), and ~15% by mass in the South Polar Layered Deposits. (Zuber et al., 2007). We assume ~2% dust mass fraction by volume and a dust grain radius of 4 μm.

References

Agnor, C.B., Lin, D.N.C., 2012. On the migration of Jupiter and Saturn: Constraints from linear models of secular resonant coupling with the terrestrial planets. Astrophys. J. 745, 143.

Albert, M., Koh, G., Perron, F., 1999. Radar investigations of melt pathways in a natural snowpack. Hydrol. Process. 13, 2991–3000.

Amundson, R. et al., 2008. On the in situ aqueous alteration of soils on Mars. Geochem. Cosmochim. Acta 72, 3845–3864.

Amundson, R. et al., 2012. Geomorphologic evidence for the late Pliocene onset of hyperaridity in the Atacama Desert. Geol. Soc. Am. Bull. 124, 1048–1070.

Andersen, D.T. et al., 2002. Cold springs in permafrost on Earth and Mars. J. Geophys. Res. 107, 5015.

Andrews-Hanna, J.C., 2012. The formation of Valles Marineris: 3. Trough formation through super-isostasy, stress, sedimentation, and subsidence. J. Geophys. Res. 117, E06002.

Andrews-Hanna, J.C., Lewis, K.W., 2011. Early Mars hydrology: 2. Hydrological evolution in the Noachian and Hesperian epochs. J. Geophys. Res. 116, E02007.

Andrews-Hanna, J.C., Phillips, R.J., Zuber, M.T., 2007. Meridiani Planum and the global hydrology of Mars. Nature 446, 163–166.

Andrews-Hanna, J.C. et al., 2010. Early Mars hydrology: Meridiani playa deposits and the sedimentary record of Arabia Terra. J. Geophys. Res. 115, E06002.

Arcone, S.A., Prentice, M.L., Delaney, A.J., 2002. Stratigraphic profiling with ground-penetrating radar in permafrost: A review of possible analogs for Mars. J. Geophys. Res. 107, 5108.

Arvidson, R.E., Guinness, E., Lee, S., 1979. Differential aeolian redistribution rates on Mars. Nature 278, 533–535.

Arvidson, R.E. et al., 2004. Localization and physical properties experiments conducted by Spirit at Gusev Crater. Science 305, 821–824.

Arvidson, R.E. et al., 2010. Spirit Mars Rover Mission: Overview and selected results from the northern Home Plate Winter Haven to the side of Scamander crater. J. Geophys. Res. 115, E00F03.

Asplund, M., Grevesse, N., Sauval, A.J., 2005. The solar chemical composition. In: Barnes, T.G. III, Bash, F.N. (Eds.), Cosmic Abundances as Records of Stellar Evolution and Nucleosynthesis. Astron. Soc. Pac. Conf. Series., vol. 336, p. 25.

Bahcall, J.N., Pinsonneault, M.H., Basu, S., 2001. Solar models: Current epoch and time dependences, neutrinos, and helioseismological properties. Astrophys. J. 555, 990–1012.

Bandfield, J.L., Glotch, T.D., Christensen, P.R., 2003. Spectroscopic identification of carbonate minerals in the martian dust. Science 301, 1084–1087.

Bandfield, J.L., Deanne Rogers, A., Edwards, C.S., 2011. The role of aqueous alteration in the formation of martian soils. Icarus 211, 157–171.

Barabash, S. et al., 2007. Martian atmospheric erosion rates. Science 315, 501–503.

Baranov, Y.I., Lafferty, W.J., Fraser, G.T., 2004. Infrared spectrum of the continuum and dimer absorption in the vicinity of the O_2 vibrational fundamental in O_2/CO_2 mixtures. J. Mol. Spectrosc. 228, 432–440.

Barnhart, C.J., Nimmo, F., 2011. Role of impact excavation in distributing clays over Noachian surfaces. J. Geophys. Res. 116, E01009.

Bengtsson, L., 1982. Percolation of meltwater through a snowpack. Cold Regions Sci. Technol. 6, 73–81.

Berger, G. et al., 2009. Evidence in favor of small amounts of ephemeral and transient water during alteration at Meridiani Planum, Mars. Am. Mineral. 94, 1279–1282.

Bibring, J. et al., 2006. Global mineralogical and aqueous Mars history derived from OMEGA/Mars Express Data. Science 312, 400–404.

Bibring, J.-P. et al., 2007. Coupled ferric oxides and sulfates on the martian surface. Science 317, 1206–1210.

Bohren, C.F., Huffman, D.R., 1983. Absorption and scattering of light by small particles.

Boynton, W.V. et al., 2002. Distribution of hydrogen in the near surface of Mars: Evidence for subsurface ice deposits. Science 297, 81–85.

Boynton, W.V. et al., 2009. Evidence for calcium carbonate at the Mars Phoenix Landing Site. Science 325, 61–64.

Bradley, B.A. et al., 2002. Medusae Fossae Formation: New perspectives from Mars Global Surveyor. J. Geophys. Res. 107, 5058.

Brandt, R.E., Warren, S.G., 1993. Solar-heating rates and temperature profiles in Antarctic snow and ice. J. Glaciol. 39, 99–110.

Bridges, N.T. et al., 2010. Aeolian bedforms, yardangs, and indurated surfaces in the Tharsis Montes as seen by the HiRISE Camera: Evidence for dust aggregates. Icarus 205, 165–182.

Bridges, N. et al., 2012. Planet-wide sand motion on Mars. Geology 40 (1), 31–34.

Brock, B.W., Willis, I.C., Sharp, M.J., 2006. Measurement and parameterization of aerodynamic roughness length variations at Haut Glacier d'Arolla, Switzerland. J. Glaciol. 52, 281–297.

Bullock, M.A., Moore, J.M., 2007. Atmospheric conditions on early Mars and the missing layered carbonates. Geophys. Res. Lett. 34, 19201.

Burr, D.M. et al., 2009. Pervasive aqueous paleoflow features in the Aeolis/Zephyria Plana region, Mars. Icarus 200, 52–76.

Burr, D.M. et al., 2010. Inverted fluvial features in the Aeolis/Zephyria Plana region, Mars: Formation mechanism and initial paleodischarge estimates. J. Geophys. Res. 115, E07011.

Cadieux, S.B., 2011. Constraining Martian Sedimentation via Analysis of Stratal Packaging, Intracrater Layered Deposits, Arabia Terra, Mars. Master's Thesis, University of Tennessee at Knoxville. <http://trace.tennessee.edu/utk_gradthes/860>.

Calvin, W.M. et al., 2009. Compact Reconnaissance Imaging Spectrometer for Mars observations of northern martian latitudes in summer. J. Geophys. Res. 114, E00D11.

Carr, M.H., Head, J.W., 2003. Basal melting of snow on early Mars: A possible origin of some valley networks. Geophys. Res. Lett. 30, 2245.

Carr, M.H., Head, J.W., 2010. Geologic history of Mars. Earth Planet. Sci. Lett. 294, 185–203.

Catling, D.C. et al., 2006. Light-toned layered deposits in Juventae Chasma, Mars. Icarus 181, 26–51.

Chittenden, J.D. et al., 2008. Experimental study of the effect of wind on the stability of water ice on Mars. Icarus 196, 477–487.

Clow, G.D., 1987. Generation of liquid water on Mars through the melting of a dusty snowpack. Icarus 72, 95–127.

Colaprete, A., Toon, O.B., 2003. Carbon dioxide clouds in an early dense martian atmosphere. J. Geophys. Res. 108, 5025.

Colaprete, A. et al., 2005. Albedo of the south pole on Mars determined by topographic forcing of atmosphere dynamics. Nature 435, 184–188.

Conway, S.J. et al., 2012. Climate-driven deposition of water ice and the formation of mounds in craters in Mars' North Polar Region. Icarus 220, 174–193.

Costard, F. et al., 2002. Formation of recent martian debris flows by melting of near-surface ground ice at high obliquity. Science 295, 110–113.

Cull, S. et al., 2010. Seasonal H_2O and CO_2 ice cycles at the Mars Phoenix Landing Site: 1. Prelanding CRISM and HiRISE observations. J. Geophys. Res. 115, E00D16.

Das, S.B. et al., 2008. Fracture propagation to the base of the Greenland ice sheet during Supraglacial Lake Drainage, Science, http://dx.doi.org/10.1126/science.1153360.

Doran, P.T. et al., 1998. Antarctic paleolake sediments and the search for extinct life on Mars. J. Geophys. Res. 103, 28481–28494.

Doran, P., Lyons, W., McKnight, D., 2010. Life in Antarctic Deserts and other Cold Dry Environments: Astrobiological Analogs. Cambridge University Press.

Drube, L. et al., 2010. Magnetic and optical properties of airborne dust and settling rates of dust at the Phoenix Landing Site. J. Geophys. Res. 115, E00E23.

Dundas, C.M., Byrne, S., 2010. Modeling sublimation of ice exposed by new impacts in the martian mid-latitudes. Icarus 206, 716–728.

Eckermann, S.D., Ma, J., Zhu, X., 2011. Scale-dependent infrared radiative damping rates on Mars and their role in the deposition of gravity-wave momentum flux. Icarus 211, 429–442.

Edgett, K.S., 2005. The sedimentary rocks of Sinus Meridiani: Five key observations from data acquired by the Mars Global Surveyor and Mars Odyssey orbiters. Mars J. 1, 5–58.

Edgett, K., 2010. Curiosity's candidate field site in Gale Crater, Mars. 4th MSL Landing Site Selection Workshop. <http://marsoweb.nas.nasa.gov/landingsites/msl/workshops/4th_workshop/talks/5_Edgett_Gale_opt.pdf>.

Edgett, K., 2011. Gale Crater in context. 5th MSL Landing Site Selection Workshop. <http://marsoweb.nas.nasa.gov/landingsites/msl/workshops/5th_workshop/talks/Tuesday_AM/Edgett_Gale_May2011xy.pdf>.

Edgett, K.S., Malin, M.C., 2002. Martian sedimentary rock stratigraphy: Outcrops and interbedded craters of northwest Sinus Meridiani and southwest Arabia Terra. Geophys. Res. Lett. 29 (24), 2179.

Ehlmann, B.L. et al., 2008. Orbital identification of carbonate-bearing rocks on Mars. Science 322, 1828–1832.

Ehlmann, B.L. et al., 2011. Subsurface water and clay mineral formation during the early history of Mars. Nature 479, 53–60.

Elwood Madden, M., Madden, A., Rimstidt, J., 2009. How long was Meridiani Planum wet? Applying a jarosite stopwatch to constrain the duration of diagenesis. Geology 37, 635.

Erkeling, G. et al., 2010. Morphologic, stratigraphic and morphometric investigations of valley networks in eastern Libya Montes, Mars: Implications for the Noachian/Hesperian climate change. Earth Planet. Sci. Lett. 294, 291–305.

Erkeling, G. et al., 2012. Valleys, paleolakes and possible shorelines at the Libya Montes/Isidis boundary: Implications for the hydrologic evolution of Mars. Icarus 219, 393–413.

Fairén, A.G. et al., 2009. Stability against freezing of aqueous solutions on early Mars. Nature 459, 401–404.

Fairén, A.G., Haqq-Misra, J.D., McKay, C.P., 2012. Reduced albedo on early Mars does not solve the climate paradox under a faint young Sun. Astron. Astrophys. 540, A13.

Fassett, C.I., Head, J.W., 2008. The timing of martian valley network activity: Constraints from buffered crater counting. Icarus 195, 61–89.

Fassett, C.I., Head, J.W., 2011. Sequence and timing of conditions on early Mars. Icarus 211, 1204–1214.

Fastook, J.L. et al., 2008. Tropical mountain glaciers on Mars: Altitude-dependence of ice accumulation, accumulation conditions, formation times, glacier dynamics, and implications for planetary spin-axis/orbital history. Icarus 198, 305–317.

Fastook, J.L. et al., 2012. Early Mars climate near the Noachian–Hesperian boundary: Independent evidence for cold conditions from basal melting of the south polar ice sheet (Dorsa Argentea Formation) and implications for valley network formation. Icarus 219, 25–40.

Fenton, L.K., Hayward, R.K., 2010. Southern high latitude dune fields on Mars: Morphology, aeolian inactivity, and climate change. Geomorphology 121, 98–121.

Forget, F. et al., 2006. Formation of glaciers on Mars by atmospheric precipitation at high obliquity. Science 311, 368–371.

Forget, F. et al., 2012. 3D modeling of the early martian climate under a dense CO_2 atmosphere: Temperatures and CO_2 ice clouds. Icarus. http://dx.doi.org/10.1016/j.icarus.2012.10.019.

Forsberg-Taylor, N.K., Howard, A.D., Craddock, R.A., 2004. Crater degradation in the martian highlands: Morphometric analysis of the Sinus Sabaeus region and simulation modeling suggest fluvial processes. J. Geophys. Res. 109, E05002.

Geissler, P.E., 2005. Three decades of martian surface changes. J. Geophys. Res. 110, E02001.

Geissler, P.E. et al., 2010. Gone with the wind: Eolian erasure of the Mars Rover tracks. J. Geophys. Res. 115, E00F11.

Glotch, T.D., Christensen, P.R., 2005. Geologic and mineralogic mapping of Aram Chaos: Evidence for a water-rich history. J. Geophys. Res. 110, 9006.

Golombek, M.P. et al., 2006. Erosion rates at the Mars Exploration Rover landing sites and long-term climate change on Mars. J. Geophys. Res. 111, E12S10.

Golombek, M. et al., 2010. Constraints on ripple migration at Meridiani Planum from opportunity and HiRISE observations of fresh craters. J. Geophys. Res. 115, E00F08.

Golombek, M. et al., 2012. Selection of the Mars Science Laboratory Landing Site. Space Sci. Rev., 1–97. http://dx.doi.org/10.1007/s11214-012-9916-y.

Goody, R., Belton, M.J.S., 1967. Radiative relaxation times for Mars. A discussion of martian atmospheric dynamics. Planet. Space Sci. 15, 247.

Grant, J.A., Parker, T.J., 2002. Drainage evolution in the Margaritifer Sinus region, Mars. J. Geophys. Res. 107, 5066.

Grant, J.A. et al., 2010. HiRISE views enigmatic deposits in the Sirenum Fossae region of Mars. Icarus 205, 53–63.

Grotzinger, J.P., Milliken, R.E., 2012. The sedimentary rock record of Mars: Distribution, origins, and global stratigraphy. In: Grotzinger, J.P. (Ed.), Sedimentary Geology of Mars, Special Publications, vol. 102. SEPM (Society for Sedimentary Geology), pp. 1–48.

Grotzinger, J. et al., 2006. Sedimentary textures formed by aqueous processes, Erebus Crater, Meridiani Planum, Mars. Geology 34, 1085.

Grotzinger, J. et al., 2012. Mars Science Laboratory mission and science investigation. Space Sci. Rev., 1–52. http://dx.doi.org/10.1007/s11214-012-9892-2.

Gruszka, M., Borysow, A., 1997. Roto-translational collision-induced absorption of CO_2 for the atmosphere of Venus at frequencies from 0 to 250 cm^{-1}, at temperatures from 200 to 800 K. Icarus 129, 172–177.

Gruszka, M., Borysow, A., 1998. Computer simulation of the far infrared collision induced absorption spectra of gaseous CO_2. Mol. Phys. 93, 1007–1016.

Guzik, J.A., Mussack, K., 2010. Exploring mass loss, low-Z accretion, and convective overshoot in solar models to mitigate the solar abundance problem. Astrophys. J. 713, 1108–1119.

Haberle, R.M., 1998. Early Mars climate models. J. Geophys. Res. 1032, 28467–28480.

Haberle, R.M. et al., 1993. Mars atmospheric dynamics as simulated by the NASA Ames General Circulation Model. I – The zonal-mean circulation. J. Geophys. Res. 98, 3093–3123.

Haberle, R.M., Murphy, J.R., Schaeffer, J., 2003. Orbital change experiments with a Mars general circulation model. Icarus 161, 66–89.

Halevy, I., Head, J.W., 2012. Punctuated volcanism, transient warming and global change in the Late Noachian–Early Hesperian. Lunar Planet. Sci. 43, 1908.

Halevy, I., Schrag, D.P., 2009. Sulfur dioxide inhibits calcium carbonate precipitation: Implications for early Mars and Earth. Geophys. Res. Lett. 36, 23201.

Halevy, I., Zuber, M.T., Schrag, D.P., 2007. A sulfur dioxide climate feedback on Early Mars. Science 318, 1903.

Halevy, I., Pierrehumbert, R.T., Schrag, D.P., 2009. Radiative transfer in CO_2-rich paleoatmospheres. J. Geophys. Res. 114, D18112.

Halevy, I., Fischer, W.W., Eiler, J.M., 2011. Carbonates in the martian meteorite Allan Hills 84001 formed at 18 ± 4 °C in a near-surface aqueous environment. Proc. Natl. Acad. Sci. 108, 16895–16899.

Hall, B.L. et al., 2010. Antarctic lakes suggest millennial reorganizations of Southern Hemisphere atmospheric and oceanic circulation. Proc. Natl. Acad. Sci. 107, 21355–21359.

Hausrath, E.M. et al., 2008. Basalt weathering rates on Earth and the duration of liquid water on the plains of Gusev Crater, Mars. Geology 36, 67–70.

Head, J.W., 2011. Geologic evidence for latitude-dependent water-related deposits on Mars: Implications for climate history and the hydrological cycle on Mars. In: Forget, F., Millour, E. (Eds.), 4th Intl. Workshop on the Mars Atmosphere, pp. 427–430.

Head, J.W., 2012. Early Mars global hydrology: Was the martian hydrologic cycle and system globally vertically integrated during the late Noachian? In: Third Intl. Conference on Early Mars, p. 7056.

Head, J.W. et al., 2003. Recent ice ages on Mars. Nature 426, 797–802.

Hecht, M.H., 2002. Metastability of liquid water on Mars. Icarus 156, 373–386.

Heldmann, J.L., 2012. Formation and evolution of buried snowpack deposits in Pearse Valley, Antarctica, and implications for Mars. Antarct. Sci. 24, 299–316.

Hendy, C., 2000. Late Quaternary lakes in the McMurdo Sound region of Antarctica. Geografiska Annaler Series A 82A (2–3), 411–432.

Herkenhoff, K.E. et al., 2008. In situ observations of the physical properties of the martian surface. In: Bell, J. III (Ed.), The Martian Surface – Composition, Mineralogy, and Physical Properties, Cambridge University Press, Cambridge, England, pp. 451–467.

Hesse, P., 2011. Sticky dunes in a wet desert: Formation, stabilisation and modification of the Australian desert dunefields. Geomorphology 134, 309–325.

Hudson, T.L., Aharonson, O., 2008. Diffusion barriers at Mars surface conditions: Salt crusts, particle size mixtures, and dust. J. Geophys. Res. 113, E09008.

Hurowitz, J.A., McLennan, S.M., 2007. A ~3.5 Ga record of water-limited, acidic weathering conditions on Mars. Earth Planet. Sci. Lett. 260, 432–443.

Hurowitz, J.A. et al., 2010. Origin of acidic surface waters and the evolution of atmospheric chemistry on early Mars. Nat. Geosci. 3, 323–326.

Hynek, B.M., Phillips, R.J., 2008. The stratigraphy of Meridiani Planum, Mars, and implications for the layered deposits' origin. Earth Planet. Sci. Lett. 274, 214–220.

Hynek, B.M., Phillips, R.J., Arvidson, R.E., 2003. Explosive volcanism in the Tharsis region: Global evidence in the martian geologic record. J. Geophys. Res. 108, 5111.

Hynek, B.M., Beach, M., Hoke, M.R.T., 2010. Updated global map of martian valley networks and implications for climate and hydrologic processes. J. Geophys. Res. 115, E09008.

Illangasekare, T. et al., 1990. Modeling of meltwater infiltration in subfreezing snow. Water Resour. 26, 1001–1012.

Irwin III, R.P., Craddock, R.A., Howard, A.D., 2005. Interior channels in martian valley networks: Discharge and runoff production. Geology 33, 489.

Jakosky, B.M., 2011. The 2013 Mars Atmosphere and Volatile EvolutioN (MAVEN) Mission to Mars. In: Forget, F., Millour, E. (Eds.), 4th Intl. Workshop on the Mars Atmosphere, pp. 477–477.

Jakosky, B.M., Carr, M.H., 1985. Possible precipitation of ice at low latitudes of Mars during periods of high obliquity. Nature 315, 559–561.

Jaumann, R. et al., 2010. The Western Libya Montes Valley System on Mars: Evidence for episodic and multi-genetic erosion events during the martian history. Earth Planet. Sci. Lett. 294, 272–290.

Jerolmack, D.J., Paola, C., 2010. Shredding of environmental signals by sediment transport. Geophys. Res. Lett. 37, 19401.

Johnson, J.R., Grundy, W.M., Lemmon, M.T., 2003. Dust deposition at the Mars Pathfinder landing site: Observations and modeling of visible/near-infrared spectra. Icarus 163, 330–346.

Johnson, S.S. et al., 2008. Sulfur-induced greenhouse warming on early Mars. J. Geophys. Res. 113, E08005.

Kadish, S.J., Head, J.W., Barlow, N.G., 2010. Pedestal crater heights on Mars: A proxy for the thicknesses of past, ice-rich, Amazonian deposits. Icarus 210, 92–101.

Kahn, R., 1985. The evolution of CO_2 on Mars. Icarus 62, 175–190.

Kahre, M.A., Murphy, J.R., Haberle, R.M., 2006. Modeling the martian dust cycle and surface dust reservoirs with the NASA Ames general circulation model. J. Geophys. Res. 111, E06008.

Kahre, M.A. et al., 2011. Stabilizing the early martian climate: Effects of airborne dust, CO_2 ice cap albedo, and orbital obliquity on atmospheric collapse. AGU (Fall Meet.). Abstracts #P21A-1656.

Kargel, J.S. et al., 2007. Martian hydrogeology sustained by thermally insulating gas and salt hydrates. Geology 35, 975.

Kasting, J.F., 1991. CO_2 condensation and the climate of early Mars. Icarus 94, 1–13.

Kerber, L. et al., 2012. The dispersal of pyroclasts from ancient explosive volcanoes on Mars: Implications for the friable layered deposits. Icarus 219, 358–381.

Keresztur, A., Vincendon, M., Schmidt, F., 2011. Water ice in the dark dune spots of Richardson crater on Mars. Planet. Space Sci. 59, 26–42.

Kieffer, H.H., 1990. H_2O grain size and the amount of dust in Mars' residual north polar cap. J. Geophys. Res. 95, 1481–1493.

Kinch, K.M. et al., 2007. Dust deposition on the Mars Exploration Rover Panoramic Camera (Pancam) calibration targets. J. Geophys. Res. 112, 6.

Kite, E.S. et al., 2009. True Polar Wander driven by late-stage volcanism and the distribution of paleopolar deposits on Mars. Earth Planet. Sci. Lett. 280, 254–267.

Kite, E.S., Gaidos, E., Manga, M., 2011a. Climate instability on tidally locked exoplanets. Astrophys. J. 743, 41.

Kite, E.S. et al., 2011b. Localized precipitation and runoff on Mars. J. Geophys. Res. 116, 7002.

Kite, E.S. et al., 2011c. Chaos terrain, storms, and past climate on Mars. J. Geophys. Res. 116, 10002.

Kite, E.S., Lewis, K.W., Lamb, M.P., Newman, C.E., Richardson, M.I., 2012a. Growth and form of the mound Gale Crater, Mars: Slope-wind enhanced erosion and transport. ArXiv e-prints arXiv:1205.6840; Geology, in press.

Kite, E.S., Lucas, A., Fassett, C.I., 2012. Pacing Early Mars fluvial activity at Aeolis Dorsa: Implications for Mars Science Laboratory observations at Gale Crater and Aeolis Mons. arXiv:1207.6726.

Knoll, A.H. et al., 2008. Veneers, rinds, and fracture fills: Relatively late alteration of sedimentary rocks at Meridiani Planum, Mars. J. Geophys. Res. 113, E06S16.

Kocurek, G., 1998. Aeolian system response to external forcing factors – A sequence stratigraphic view of the Saharan region. In: Alsharhan, A.S., Glennie, K.W., Whittle, G.L., Kendall, C.G.St.C. (Eds.), Quaternary Deserts and Climatic Change. A.A. Balkema Publishers, pp. 327–337.

Koeppen, W.C., Hamilton, V.E., 2008. Global distribution, composition, and abundance of olivine on the surface of Mars from thermal infrared data. J. Geophys. Res. 113, 5001.

Kopp, G., Lean, J.L., 2011. A new, lower value of total solar irradiance: Evidence and climate significance. Geophys. Res. Lett. 38, 1706.

Kraal, E.R. et al., 2008. Martian stepped-delta formation by rapid water release. Nature 451, 973–976.

Kreslavsky, M.A., Head, J.W., 2011. Carbon dioxide glaciers on Mars: Products of recent low obliquity epochs(?). Icarus 216, 111–115.

Laskar, J., 2008. Chaotic diffusion in the Solar System. Icarus 196, 1–15.

Laskar, J., Robutel, P., 1993. The chaotic obliquity of the planets. Nature 361, 608–612.

Laskar, J. et al., 2004. Long term evolution and chaotic diffusion of the insolation quantities of Mars. Icarus 170, 343–364.

Lee, P., McKay, C.P., 2003. Mars: Always cold, sometimes wet? Lunar Planet. Sci. 34, 2127.

Lefort, A., Russell, P.S., Thomas, N., 2010. Scalloped terrains in the Peneus and Amphitrites Paterae region of Mars as observed by HiRISE. Icarus 205, 259–268.

Levrard, B. et al., 2004. Recent ice-rich deposits formed at high latitudes on Mars by sublimation of unstable equatorial ice during low obliquity. Nature 431, 1072–1075.

Lewis, K.J., 2001. Solar-Forced Roughening of Antarctic Glaciers and the Martian Icecaps: How Surficial Debris and Roughness Affect Glacial Melting in Taylor Valley, Antarctica and How this can be Applied to the Martian Icecaps. Ph.D. Thesis, University of Colorado at Boulder.

Lewis, K.W., 2009. The rock record of Mars: Structure, sedimentology and stratigraphy. Ph.D. Thesis, Caltech. <http://thesis.library.caltech.edu/2486/>.

Lewis, K.W. et al., 2008. Quasi-periodic bedding in the sedimentary rock record of Mars. Science 322, 1532–1535.

Lewis, K.W. et al., 2010. Global significance of cyclic sedimentary deposits on Mars. Lunar Planet. Sci. 41, 2648.

Liston, G.E., Winther, J.-G., 2005. Antarctic surface and subsurface snow and ice melt fluxes. J. Climate 18, 1469–1481.

Loizeau, D., Werner, S.C., Mangold, N., Bibring, J.-P., Vago, J.L., 2012. Chronology of deposition and alteration in the Mawrth Vallis region, Mars. Planet. Space Sci. 72 (1), 31–43.

Maarry, M.R.E. et al., 2012. Searching for evidence of hydrothermal activity at Apollinaris Mons, Mars. Icarus 217 (1), 297–314.

Madeleine, J.-B. et al., 2009. Amazonian northern mid-latitude glaciation on Mars: A proposed climate scenario. Icarus 203, 390–405.

Madeleine, J.-B. et al., 2011. Revisiting the radiative impact of dust on Mars using the LMD Global Climate Model. J. Geophys. Res. 116, E11010.

Malin, M.C., Edgett, K.S., 2000. Sedimentary rocks of early Mars. Science 290, 1927–1937.

Malin, M.C. et al., 2010. An overview of the 1985–2006 Mars Orbiter Camera science investigation. Mars J. 5, 1–60.

Manga, M. et al., 2012. Wet surface and dense atmosphere on early Mars suggested by the bomb sag at Home Plate, Mars. Geophys. Res. Lett. 39, 1202.

Mangold, N. et al., 2009. Estimate of aeolian dust thickness in Arabia Terra, Mars. Geomorphologie (1), 23–31.

Mangold, N. et al., 2010. A Late Amazonian alteration layer related to local volcanism on Mars. Icarus 207, 265–276.

Mangold, N. et al., 2012. The origin and timing of fluvial activity at Eberswalde Crater, Mars. Icarus 220, 530–551.

Manning, C.V., McKay, C.P., Zahnle, K.J., 2006. Thick and thin models of the evolution of carbon dioxide on Mars. Icarus 180, 38–59.

Manning, C.V. et al., 2011. Parametric analysis of modeled ion escape from Mars. Icarus 212, 131–137.

Marchant, D.R., Head, J.W., 2007. Antarctic dry valleys: Microclimate zonation, variable geomorphic processes, and implications for assessing climate change on Mars. Icarus 192, 187–222.

Marsh, P., Woo, M.-K., 1984. Wetting front advance and freezing of meltwater within a snow cover 1. Observations in the Canadian Arctic. Water Resour. Res. 20, 1853–1864.

Massé, M. et al., 2012. Wide distribution and glacial origin of polar gypsum on Mars. Earth Planet. Sci. Lett. 317, 44–55.

Matsuyama, I., Manga, M., 2010. Mars without the equilibrium rotational figure, Tharsis, and the remnant rotational figure. J. Geophys. Res. 115, E1020.

McGlynn, I.O., Fedo, C.M., McSween Jr., H.Y., 2012. Soil mineralogy at the Mars Exploration Rover landing sites: An assessment of the competing roles of physical sorting and chemical weathering. J. Geophys. Res. 117, 1006.

McKay, C.P., Davis, W.L., 1991. Duration of liquid water habitats on early Mars. Icarus 90, 214–221.

McKelvey, B., 1981. The lithologic logs of DVDP Cores 10 and 11, Eastern Taylor Valley. In: McGinnis, L.D. (Ed.), Dry Valley Drilling Project, Antarctic Research Series, vol. 33. American Geophysical Union, p. 63.

McKeown, N.K. et al., 2009. Characterization of phyllosilicates observed in the central Mawrth Vallis region, Mars, their potential formational processes, and implications for past climate. J. Geophys. Res. 114, E00D10.

McKnight, D., 2011. Onyx River at Vanda Gauge Measurements. National Science Foundation McMurdo Dry Valleys Long Term Ecological Research Signature Datasets. knb-lter-mcm.9022.4.

McLennan, S.M., Grotzinger, J.P., 2008. The sedimentary rock cycle of Mars. In: Bell, J., III (Ed.), The Martian Surface – Composition, Mineralogy, and Physical Properties. Cambridge University Press, pp. 541–577.

McLennan, S.M. et al., 2005. Provenance and diagenesis of the evaporite-bearing Burns formation, Meridiani Planum, Mars. Earth Planet. Sci. Lett. 240, 95–121.

McLennan, S.M. et al., 2010. Distribution of sulfur on the surface of Mars determined by the 2001 Mars Odyssey Gamma Ray Spectrometer. Lunar Planet. Sci. 41, 2174.

McSween, H.Y., McGlynn, I.O., Rogers, A.D., 2010. Determining the modal mineralogy of martian soils. J. Geophys. Res. 115, E00F12.

Mellon, M.T., Jakosky, B.M., 1995. The distribution and behavior of martian ground ice during past and present epochs. J. Geophys. Res. 1001, 11781–11799.

Mellon, M.T. et al., 2000. High-resolution thermal inertia mapping from the Mars Global Surveyor Thermal Emission Spectrometer. Icarus 148, 437–455.

Metz, J.M. et al., 2009. Sulfate-rich eolian and wet interdune deposits, Erebus Crater, Meridiani Planum, Mars. J. Sediment. Res. 79, 247–264.

Michalski, J., Niles, P., 2012. Atmospheric origin of martian interior layered deposits: Links to climate change and the global sulfur cycle. Geology 40, 419.

Michalski, J.R., Noe Dobrea, E.Z., 2007. Evidence for a sedimentary origin of clay minerals in the Mawrth Vallis region, Mars. Geology 35, 951.

Milliken, R.E., Bish, D.L., 2010. Sources and sinks of clay minerals on Mars. Philos. Mag. 90, 2293–2308.

Milliken, R.E., Grotzinger, J.P., Thomson, B.J., 2010. Paleoclimate of Mars as captured by the stratigraphic record in Gale Crater. Geophys. Res. Lett. 370, L04201.

Millour, E., Forget, F., Lewis, S.R., 2008. European Mars Climate Database v4.3 Detailed Design Document. Tech. Rep., Lab. de Météorol. Dyn., Paris. <http://www-mars.lmd.jussieu.fr/>.

Ming, D.W., Morris, R.V., Clark, B.C., 2008. Aqueous alteration on Mars. In: Bell, J., III (Ed.), The Martian Surface – Composition, Mineralogy, and Physical Properties. Cambridge University Press, pp. 519–540.

Minton, D.A., Malhotra, R., 2007. Assessing the massive young Sun hypothesis to solve the warm young Earth puzzle. Astrophys. J. 660, 1700–1706.

Mischna, M.A., Richardson, M.I., 2006. Climate simulation of recent climate changes on Mars. In: Forget, F. et al. (Eds.), Mars Atmosphere Modelling and Observations. Second workshop on Mars atmosphere modelling and observations. LMD, IAA, AOPP, CNES, ESA, Granada, Spain, pp. 312–315.

Mischna, M.A. et al., 2003. On the orbital forcing of martian water and CO_2 cycles: A general circulation model study with simplified volatile schemes. J. Geophys. Res. 108, 5062.

Mitchell, K.L., 2004. Asymmetric ramparts of secondary craters in Cerberus, Mars: Interpretation and implications for local stratigraphy. Lunar Planet. Sci. 35, 1547.

Möhlmann, D.T.F., 2010. Temporary liquid water in upper snow/ice sub-surfaces on Mars? Icarus 207, 140–148.

Montmessin, F. et al., 2007. On the origin of perennial water ice at the south pole of Mars: A precession-controlled mechanism? J. Geophys. Res. 112, E08S17.

Morgan, G.A. et al., 2010. Gully formation on Mars: Two recent phases of formation suggested by links between morphology, slope orientation and insolation history. Icarus 208, 658–666.

Morris, R.V. et al., 2006a. Mössbauer mineralogy of rock, soil, and dust at Gusev Crater, Mars: Spirit's journey through weakly altered olivine basalt on the plains and pervasively altered basalt in the Columbia Hills. J. Geophys. Res. 111, E02S13.

Morris, R.V. et al., 2006b. Mössbauer mineralogy of rock, soil, and dust at Meridiani Planum, Mars: Opportunity's journey across sulfate-rich outcrop, basaltic sand and dust, and hematite lag deposits. J. Geophys. Res. 111, E12S15.

Morris, R.V. et al., 2008. Iron mineralogy and aqueous alteration from Husband Hill through Home Plate at Gusev Crater, Mars: Results from the Mössbauer instrument on the Spirit Mars Exploration Rover. J. Geophys. Res. 113, E12S42.

Morris, R. et al., 2010. Identification of carbonate-rich outcrops on Mars by the Spirit Rover. Science 329 (5990), 421–424.

Murchie, S. et al., 2009a. Evidence for the origin of layered deposits in Candor Chasma, Mars, from mineral composition and hydrologic modeling. J. Geophys. Res. 114, E00D05.

Murchie, S.L. et al., 2009b. A synthesis of martian aqueous mineralogy after 1 Mars year of observations from the Mars Reconnaissance Orbiter. J. Geophys. Res. 114, E00D06.

Murray, C.D., Dermott, S.F., 2000. Solar System Dynamics. Cambridge University Press.

Newman, C.E., Lewis, S.R., Read, P.L., 2005. The atmospheric circulation and dust activity in different orbital epochs on Mars. Icarus 174, 135–160.

Nezat, C., Lyons, W., Welch, K., 2001. Chemical weathering in streams of a polar desert, Taylor Valley, Antarctica. Geol. Soc. Am. Bull. 113 (11), 1401–1408.

Nickling, W.G., 1984. The stabilizing role of bonding agents on the entrainment of sediment by wind. Sedimentology 31, 111–117.

Niles, P.B., Michalski, J., 2009. Meridiani Planum sediments on Mars formed through weathering in massive ice deposits. Nat. Geosci. 2, 215–220.

Niles, P.B., Michalski, J., 2012. Origin and evolution of sediments in Gale Crater through ice-hosted processes. Lunar Planet. Sci. 43, 2575.

Niles, P.B. et al., 2010. Stable isotope measurements of martian atmospheric CO_2 at the Phoenix Landing Site. Science 329, 1334–1337.

Noe Dobrea, E.Z. et al., 2010. Mineralogy and stratigraphy of phyllosilicate-bearing and dark mantling units in the greater Mawrth Vallis/west Arabia Terra area: Constraints on geological origin. J. Geophys. Res. 115, E00D19.

Okubo, C.H., 2007. Strength and deformability of light-toned layered deposits observed by MER Opportunity: Eagle to Erebus Craters, Mars. Geophys. Res. Lett. 34, 20205.

Olsen, A., Rimstidt, J., 2007. Using a mineral lifetime diagram to evaluate the persistence of olivine on Mars. Am. Mineral. 92 (4), 598–602.

Osterloo, M.M. et al., 2010. Geologic context of proposed chloride-bearing materials on Mars. J. Geophys. Res. 115, E10012.

Pälike, H. et al., 2006. The heartbeat of the Oligocene climate system. Science 314, 1894–1898.

Phillips, R.J. et al., 2001. Ancient geodynamics and global-scale hydrology on Mars. Science 291, 2587–2591.

Phillips, R.J. et al., 2011. Massive CO_2 ice deposits sequestered in the south polar layered deposits of Mars. Science 332, 838–841.

Pollard, W. et al., 1999. Perennial spring occurrence in the Expedition Fiord area of western Axel Heiberg Island, Canadian High Arctic. Can. J. Earth Sci. 36, 105–120.

Press, W. et al., 2007. Numerical Recipes, The Art of Scientific Computing, third ed. Cambridge University Press.

Putzig, N.E., Mellon, M.T., 2007. Apparent thermal inertia and the surface heterogeneity of Mars. Icarus 191, 68–94.

Putzig, N.E. et al., 2005. Global thermal inertia and surface properties of Mars from the MGS mapping mission. Icarus 173, 325–341.

Richardson, M.I., Mischna, M.A., 2005. Long-term evolution of transient liquid water on Mars. J. Geophys. Res. 110, E03003.

Richardson, M.I., Soto, A., 2008a. Controls on precipitation and aridity for ancient Mars. In: Proc. Second Workshop on Mars Valley Networks. Moab, Utah., Smithson. Inst.

Richardson, M.I., Soto, A., 2008b. Water at the surface of ancient Mars. In: Proc. Second Workshop on Mars Valley Networks. Moab, Utah., Smithson. Inst.

Righter, K., Pando, K., Danielson, L.R., 2009. Experimental evidence for sulfur-rich martian magmas: Implications for volcanism and surficial sulfur sources. Earth Planet. Sci. Lett. 288, 235–243.

Sackmann, I.-J., Boothroyd, A.I., 2003. Our Sun. V. A bright young Sun consistent with helioseismology and warm temperatures on ancient Earth and Mars. Astrophys. J. 583, 1024–1039.

Sagan, C., Mullen, G., 1972. Earth and Mars: Evolution of atmospheres and surface temperatures. Science 177, 52–56.

Salvatore, M.R. et al., 2010. Definitive evidence of Hesperian basalt in Acidalia and Chryse planitiae. J. Geophys. Res. 115, E07005.

Scheidegger, J.M., Bense, V.F., Grasby, S.E., 2012. Transient nature of Arctic spring systems driven by subglacial meltwater. Geophys. Res. Lett. 39, 12405.

Schon, S.C., Head, J.W., 2012. Decameter-scale pedestal craters in the tropics of Mars: Evidence for the recent presence of very young regional ice deposits in Tharsis. Earth Planet. Sci. Lett. 317, 68–75.

Schorghofer, N., Aharonson, O., 2005. Stability and exchange of subsurface ice on Mars. J. Geophys. Res. 110, 5003.

Schorghofer, N., Forget, F., 2012. History and anatomy of subsurface ice on Mars. Icarus 220, 1112–1120.

Selvans, M.M. et al., 2010. Internal structure of Planum Boreum, from Mars advanced radar for subsurface and ionospheric sounding data. J. Geophys. Res. 115, E09003.

Shanley, K., McCabe, P., 1994. Perspectives on the sequence stratigraphy of continental strata. AAPG Bull. 78 (4), 544–568.

Shaw, J., Healy, T., 1980. Morphology of the Onyx River system, McMurdo sound region, Antarctica. N. Z. J. Geol. Geophys. 23 (2), 223–238.

Shean, D.E., 2010. Candidate ice-rich material within equatorial craters on Mars. Geophys. Res. Lett. 372, L24202.

Siebach, K., Grotzinger, J., 2012. Boxwork structures and groundwater volume estimates on Mount Sharp, Mars. In: Geol. Soc. Am. Annual Meeting, vol. 37.

Skinner, J.A., Tanaka, K.L., Platz, T., 2012. Widespread loess-like deposit in the martian northern lowlands identifies middle amazonian climate change. Geology 40, 1127–1130.

Sloan, C.E., van Everdingen, R.O., 1998. Permafrost region. In: Back, W., Rosenshein, J.S., Seaber, P.R. (Eds.), Hydrogeology. Vol. O_2 of Decade of North American Geology. Geol. Soc. Am., p. 541.

Soto, A., 2012. Martian Climate Dynamics Through Thick and Thin, Chapter 2 in Dynamical Paleoclimatology of Mars. Ph.D. Thesis, Caltech.

Squyres, S.W., Kasting, J.F., 1994. Early Mars: How warm and how wet? Science 265, 744–749.

Squyres, S.W. et al., 2004. In situ evidence for an ancient aqueous environment at Meridiani Planum, Mars. Science 306, 1709–1714.

Squyres, S.W. et al., 2006. Rocks of the Columbia Hills. J. Geophys. Res. 111, E02S11.

Squyres, S.W. et al., 2012. Ancient impact and aqueous processes at Endeavour Crater, Mars. Science 336, 570–576.

Stokes, S., Bray, H., 2005. Late Pleistocene eolian history of the Liwa region, Arabian Peninsula. Geol. Soc. Am. Bull. 117 (11–12), 1466–1480.

Summons, R.E. et al., 2011. Preservation of martian organic and environmental records: Final report of the Mars Biosignature Working Group. Astrobiology 11, 157–181.

Taylor, G.J. et al., 2010. Mapping Mars geochemically. Geology 38 (2), 183–186.

Tian, F. et al., 2010. Photochemical and climate consequences of sulfur outgassing on early Mars. Earth Planet. Sci. Lett. 295, 412–418.

Titus, T.N., Kieffer, H.H., Christensen, P.R., 2003. Exposed water ice discovered near the south pole of Mars. Science 299, 1048–1051.

Toon, O. et al., 1980. The astronomical theory of climatic change on Mars. Icarus 44, 552–607.

Toon, O.B., Segura, T., Zahnle, K., 2010. The formation of martian river valleys by impacts. Ann. Rev. Earth Planet. Sci. 38, 303–322.

Tosca, N.J., Knoll, A.H., 2009. Juvenile chemical sediments and the long term persistence of water at the surface of Mars. Earth Planet. Sci. Lett. 286, 379–386.

Touma, J., Wisdom, J., 1993. The chaotic obliquity of Mars. Science 259, 1294–1297.

Turck-Chièze, S., Piau, L., Couvidat, S., 2011. The solar energetic balance revisited by young solar analogs, helioseismology, and neutrinos. Astrophys. J. 731, L29.

Vaniman, D.T., 2011. Deriving a history of deposition and alteration from phyllosilicate–sulfate associations at Gale Crater. AGU (Fall Meet.). Abstracts #P32A-04.

Vincendon, M., Forget, F., Mustard, J., 2010. Water ice at low to midlatitudes on Mars. J. Geophys. Res. 115, E10001.

Warner, N. et al., 2009. A refined chronology of catastrophic outflow events in Ares Vallis, Mars. Earth Planet. Sci. Lett. 288, 58–69.

Warner, N.H. et al., 2011. Constraints on the origin and evolution of Iani Chaos, Mars. J. Geophys. Res. 116, 6003.

Warren, S.G., 1982. Optical properties of snow. Rev. Geophys. Space Phys. 20, 67.

Warren, S.G., 1984. Review. Impurities in snow: Effects on albedo and snowmelt. Annal. Glaciol. 5, 177–179.

Warren, S.G., Brandt, R.E., 2008. Optical constants of ice from the ultraviolet to the microwave: A revised compilation. J. Geophys. Res. 113, 14220.

Warren, S.G., Wiscombe, W.J., 1980. A model for the spectral albedo of snow. II: Snow containing atmospheric aerosols. J. Atmos. Sci. 37, 2734–2745.

Whiteway, J., Komguem, L., Dickinson, C., 2011. Observations of Mars atmospheric dust and clouds with the lidar instrument on the Phoenix mission. In: Forget, F., Millour, E. (Eds.), 4th Intl. Workshop on the Mars Atmosphere, pp. 171–174.

Wierzchos, J. et al., 2012. Novel water source for endolithic life in the hyperarid core of the Atacama Desert. Biogeosciences 9, 2275–2286.

Williams, R.M.E., 2007. Global spatial distribution of raised curvilinear features on Mars. Lunar Planet. Sci. 38, 1821.

Williams, K.E. et al., 2008. Stability of mid-latitude snowpacks on Mars. Icarus 196, 565–577.

Williams, K.E. et al., 2009. Ancient melting of mid-latitude snowpacks on Mars as a water source for gullies. Icarus 200, 418–425.

Wilson, S.A. et al., 2007. Geomorphic and stratigraphic analysis of Crater Terby and layered deposits north of Hellas basin, Mars. J. Geophys. Res. 112, 8009.

Wilson, S.A. et al., 2010. Evidence for ancient lakes in the Hellas region. In: Cabrol, N.A., Grin, E.A. (Eds.), Lakes on Mars. Elsevier B.V., pp. 195–222.

Wilson, S.A., Grant, J.A., Howard, A.D., 2012. Distribution of intracrater alluvial fans and deltaic deposits in the southern highlands of Mars. Lunar Planet. Sci. 43, 2462.

Wolff, M.J., Clancy, R.T., 2003. Constraints on the size of martian aerosols from Thermal Emission Spectrometer observations. J. Geophys. Res. 108, 5097.

Wolff, M.J. et al., 2006. Constraints on dust aerosols from the Mars Exploration Rovers using MGS overflights and Mini-TES. J. Geophys. Res. 111, E12S17.

Wolff, M.J. et al., 2009. Wavelength dependence of dust aerosol single scattering albedo as observed by the Compact Reconnaissance Imaging Spectrometer. J. Geophys. Res. 114, E00D04.

Wood, B.E. et al., 2005. New mass-loss measurements from astrospheric Lyα absorption. Astrophys. J. 628, L143–L146.

Wordsworth, R., Forget, F., Eymet, V., 2010. Infrared collision-induced and far-line absorption in dense CO_2 atmospheres. Icarus 210, 992–997.

Wordsworth, R. et al., 2012a. Global modelling of the early martian climate under a denser CO_2 atmosphere: Water cycle and ice evolution. Icarus. http://dx.doi.org/10.1016/j.icarus.2012.09.0363.

Wordsworth, R. et al., 2012b. How important is CO_2 to planetary habitability? In: 2nd Exoclimes workshop, Aspen, CO. <http://www.astro.ex.ac.uk/exoclimes/2012/pdf/talks/Day02_Wordsworth.pdf>.

Wray, J.J., 2012. Gale Crater: The Mars Science Laboratory/Curiosity Landing Site. Int. J. Astrobiol.. http://dx.doi.org/10.1017/S1473550412000328.

Wray, J.J. et al., 2011. Columbus crater and other possible groundwater-fed paleolakes of Terra Sirenum, Mars. J. Geophys. Res. 116, E01001.

Yang, P. et al., 2002. Inherent and apparent scattering properties of coated or uncoated spheres embedded in an absorbing host medium. Appl. Opt. 41, 2740–2759.

Zabrusky, K., Andrews-Hanna, J.C., Wiseman, S.M., 2012. Reconstructing the distribution and depositional history of the sedimentary deposits of Arabia Terra, Mars. Icarus 220, 311–330.

Zalucha, A.M., Plumb, R.A., Wilson, R.J., 2010. An analysis of the effect of topography on the martian Hadley cells. J. Atmos. Sci. 67, 673–693.

Zanetti, M. et al., 2010. Distribution and evolution of scalloped terrain in the southern hemisphere, Mars. Icarus 206, 691–706.

Zuber, M.T. et al., 2007. Density of Mars' south polar layered deposits. Science 317, 1718.